

Thin-film-specific elastic effects in ferroelectric domain structures

THÈSE N° 6953 (2016)

PRÉSENTÉE LE 25 FÉVRIER 2016

À LA FACULTÉ DES SCIENCES ET TECHNIQUES DE L'INGÉNIEUR
LABORATOIRE DE CÉRAMIQUE
PROGRAMME DOCTORAL EN SCIENCE ET GÉNIE DES MATÉRIAUX

ÉCOLE POLYTECHNIQUE FÉDÉRALE DE LAUSANNE

POUR L'OBTENTION DU GRADE DE DOCTEUR ÈS SCIENCES

PAR

Konstantin SHAPOVALOV

acceptée sur proposition du jury:

Prof. A. Fontcuberta i Morral, présidente du jury
Prof. A. Tagantsev, Prof. N. Setter, directeurs de thèse
Prof. N. Pertsev, rapporteur
Dr A. Cano, rapporteur
Prof. N. Marzari, rapporteur



ÉCOLE POLYTECHNIQUE
FÉDÉRALE DE LAUSANNE

Suisse
2016

Acknowledgements

First of all, I would like to express my sincere and strong gratitude to Alexander Tagantsev, Nava Setter and Peter Yudin, who offered me a possibility to gain experience of conducting scientific research in multinational environment in one of the strongest universities in material science. Without them, the current thesis could not be possible. Scientific discussions with Alexander Tagantsev have been priceless, as were his advices on the effective management of my time needed for reaching the set goals. I am also grateful to Peter for helping me to set higher and higher goals each time, allowing me to develop my understanding of science and to learn to efficiently apply the gathered knowledge to real problems. His help during the first years of my work in the Ceramics Laboratory made my transition between the two states – of student in Novosibirsk and of scientist in Lausanne – relatively easy. I am grateful to Nava Setter for believing in my potential of development and accepting me to her laboratory despite me having neither Master education nor international experience in the research at the moment of application. I am also grateful to Nava for organizing annual workshops and other events which helped me to know better my coworkers as well as other material scientists in European universities.

I would like to thank the members of jury: Nicolay Pertsev, Andres Cano, Nicola Marzari, Anna Fontcuberta i Morral for fruitful discussion of my thesis during my oral exam, showing me the points where it could be possible to do differently and improve the general quality of the work, and allowing me to reformulate my general approach to conducting scientific research in future.

I am grateful to my coworkers: Arnaud, Tomas, Leo, Barbara, Nachi, Kaushik, Alex, Sarunas, Peter B, Zhen, Robin, Sina, and all others for providing me with this first incredible international experience.

Lausanne, 2016

K. Shapovalov

Abstract

An essential feature of ferroelectric thin films is the presence in them of domain structures. In order to efficiently implement ferroelectric films into potential new ferroelectrics-based devices, it is of high interest to understand the behaviour of domain structures. Some properties of ferroelectric domain structures, such as internal structure of domain walls, orientation of domain walls, which were investigated and formulated for bulk systems, are typically believed to be applicable to thin films as well.

In this work, importance of thin-film-specific effects on domain structure formation is discussed. It is shown that in thin films nonferroelastic domain walls may interact by elastic means on distances far exceeding the domain wall width, which is sometimes considered as the maximal range of their interaction. Theoretical study of films of practical interest shows that the force of elastic repulsion between the walls can be strong enough to be important during the polarization switching and for control of nonferroelastic domain structures.

Further, this work discusses mechanisms of ferroelastic domain wall orientation specific to thin films. Typically, when a ferroelastic wall orients violating the condition of mechanical compatibility of the domains, macroscopic elastic fields appear leading to increase of the energy of the system restraining the deviation of the wall from the compatible state. It is shown that in thin films this increase of the energy can be small enough to allow competition with other contributions to the energy, such as domain wall self-energy, leading to large deviations of the wall orientation from its compatible state.

Another investigated mechanism of ferroelastic domain wall orientation is interference of elastic fields generated by an incompatible wall with the film-substrate misfit stresses. A system is investigated where such interference, which leads to reduction of elastic energy of the structure, results in deviation of the wall from its compatible state, violating the domain wall electric neutrality as well. Using this result, the concept of elasticity-driven generation of charged conductive domain walls is developed; the concept is supported by reports of experimental observation of metallic-like domain wall conduction in $\text{Pb}(\text{Zr}, \text{Ti})\text{O}_3$ films.

A theoretical description is provided for ferroelastic structures with narrow domain inclusions into dominant domain state. It is obtained that in sparse structures the domain

Acknowledgements

periodicity follows linear dependence on the film thickness, not the classical Kittel-like square root dependence. Equilibrium parameters of the domain structure, such as periodicity of the structure, width of the narrow inclusions, are obtained; the results for $\text{Pb}(\text{Zr}, \text{Ti})\text{O}_3$ films are compared with experimental observations of the films.

Finally, antiphase boundary with local ferroelectricity in antiferroelectric is investigated. The mechanical response of such boundary on external electric field is modelled. It is shown that the electric field gradient can be used as the driving force for displacement of the boundary. Conditions for displacement of the boundary sufficient for Scanning Probe Microscopy observations are formulated.

Key words: ferroelectricity, thin films, domain walls, elastic domain structures control, domain wall conductivity, antiphase boundary.

Résumé

Une caractéristique essentielle des couches minces ferroélectriques est la présence en leur sein de différentes structures de domaines. Afin de pouvoir intégrer efficacement les couches minces ferroélectriques dans de possibles nouveaux appareils basés sur les matériaux ferroélectriques, il est très important de comprendre le comportement de ces structures de domaine. Certaines propriétés des structures de domaines ferroélectriques, telles que la structure interne des parois de domaine ou leur orientation, ont été étudiées et formulées pour les systèmes macroscopiques, et sont généralement considérées comme également applicables aux couches minces.

Dans ce travail, l'importance des effets spécifiques aux couches minces agissant sur la formation des structures de domaine est discutée. Nous montrons que, dans les couches minces, les parois de domaine non-ferroélastiques peuvent avoir des interactions élastiques sur des distances dépassant de loin la largeur d'une paroi de domaine, cette dernière étant parfois considérée comme la portée maximale de leur interaction. L'étude théorique des couches présentant un intérêt pratique montre que la force de répulsion élastique entre les parois peut être assez forte pour jouer un rôle lors de la commutation de polarisation et dans le contrôle des structures de domaines non-ferroélastiques.

De plus, ce travail discute les mécanismes d'orientation des parois de domaines ferroélastiques spécifiques aux couches minces. Typiquement, quand une paroi ferroélastique est orientée en violation de la condition de compatibilité mécanique entre deux domaines voisins, des champs élastiques macroscopiques apparaissent, conduisant à une augmentation de l'énergie du système, et restreignant ainsi les possibilités de déviation de la paroi de son état compatible. Nous montrons que, dans les couches minces, cette augmentation de l'énergie peut être assez petite pour permettre une compétition avec d'autres contributions à l'énergie totale du système, telles que l'énergie de surface de la paroi de domaine, conduisant à de grandes déviations de l'orientation de la paroi par rapport à l'état compatible.

Un autre mécanisme d'orientation des parois de domaines ferroélastiques que nous avons étudié, est l'interférence entre le champ élastique généré par une paroi incompatible et les contraintes d'incompatibilité entre la couche mince et le substrat. Nous avons étudié un

Acknowledgements

système où de telles interférences, qui conduisent à la réduction de l'énergie élastique totale de la structure, se traduisent par la déviation de l'orientation de la paroi par rapport à son état compatible, en violant de plus la neutralité électrique de la paroi de domaine. En se basant sur ce résultat, nous développons le concept de génération de parois de domaines chargées et conductrices par des moyens élastiques ; ce concept est soutenu par l'observation expérimentale d'une conduction de type métallique par des parois de domaines dans des couches minces de $\text{Pb}(\text{Zr}, \text{Ti})\text{O}_3$.

Nous présentons une description théorique pour les structures ferroélastiques consistant en des inclusions de domaines étroits au sein d'un domaine prédominant. Nous trouvons que dans les structures à faible fréquence spatiale d'inclusions, la périodicité des domaines dépend linéairement de l'épaisseur du film, et ne suit pas la dépendance classique de Kittel en la racine carrée de l'épaisseur. Nous calculons les paramètres à l'équilibre de la structure de domaines, tels que la périodicité de la structure et la largeur des inclusions étroites ; nous comparons les résultats pour les couches de $\text{Pb}(\text{Zr}, \text{Ti})\text{O}_3$ avec des observations expérimentales de ces films.

Enfin, la paroi antiphase séparant deux domaines antiferroélectriques, et qui présente des propriétés ferroélectriques locales, est étudiée. La réponse mécanique d'une telle paroi à un champ électrique externe est modélisée. Nous montrons que le gradient de champ électrique peut être utilisé en tant que force motrice pour le déplacement de la paroi. Nous formulons les conditions de déplacement de la paroi suffisantes pour des observations par microscopie à sonde locale.

Mots-clefs : ferroélectricité, couches minces, paroi de domaine, contrôle de la structure des domaines élastiques, conductivité des parois de domaines, paroi antiphase.

List of designations

Following designations were used in the work (in alphabetic order):

- a (c , a_f) – lattice constants of the film. Tetragonal film: $a \times a \times c$. Rhombohedral film: $a_f \times a_f \times a_f$.
- a_s (a_{s1} , a_{s2} , a_{s3}) – lattice constant of the substrate. Cubic substrate: $a_s \times a_s \times a_s$. Orthorhombic substrate: $a_{s1} \times a_{s2} \times a_{s3}$.
- \mathbf{b} – Burgers vector.
- c_{ijkl} – tensor of elastic stiffness.
- $D(y)$ – function of deviation of the domain wall: at level $y = y_0$, the x -deviation of the wall off its permissible orientation is $D(y_0)$.
- E – Young modulus.
- $\mathbf{E} = (E_1, E_2, E_3)$ – electric field.
- e_{ijk} – Levi-Civita permutation symbol.
- $f(x)$ – dimensionless function describing the profile of polarization in the bulk material: $P(x) = P_S f(x/2\xi)$, ξ – correlation length.
- G (Chapters 2,3) – Gibbs potential.
- G (Chapter 4) – shear modulus.
- g_{ijkl} ($g_{\alpha\beta}$) – correlation energy in tensor (in Voigt) notations.
- h – thickness of the film.
- h_0 – characteristic film thickness. For a/c -domain structures in tetragonal film with lattice constants $a \times a \times c$, $h_0 = 6.1\lambda(1 - \nu^2)a^2/(E(c - a)^2)$, λ – domain wall self-energy per wall unit area, E – Young modulus, ν – Poisson ratio.

Acknowledgements

- h_S – thickness of the substrate.
- L – size of sample in x -direction.
- l – period of domain structure.
- P – polarization.
- P_S (P_S^I, P_S^{II}) – spontaneous polarization (in domain I, II).
- p – force (per unit length, per unit area, depending on the context).
- Q_{ijkl} ($Q_{\alpha\beta}$) – electrostriction in tensor (in Voigt) notations.
- q_{ijkl} ($q_{\alpha\beta}$) – electrostriction in tensor (in Voigt) notations. $s_{ijmn}q_{mnlk} = Q_{ijkl}$.
- R – radius of AFM tip.
- r_1, r_2, r_3 (x, y, z) – Cartesian coordinates.
- s_{ijkl} ($s_{\alpha\beta}$) – elastic compliance in tensor (in Voigt) notations.
- U – energy of the system (per unit length, per unit area, per unit volume, depending on the context).
- w (Chapters 3, 4, 5, 6) – distance between domain walls, width of domain.
- w (Chapter 7) – width of antiphase boundary.
- y_i – initial y -coordinate of antiphase boundary.
- α, β, γ (Chapters 2, 3) – 2nd, 4th, 6th order dielectric stiffnesses.
- α_{ij} – tensor of density of dislocations.
- α_{rh} – angle between $\langle 100 \rangle$ directions of rhombohedral unit cell.
- β (Chapters 4, 5) – cubic-rhombohedral angular mismatch: $\beta = (\pi/2) - \alpha_{rh}$.
- $\beta_{S_{ij}}$ – unsymmetrized tensor of spontaneous deformations: $\beta_{S_{ij}} = \partial u_j / \partial r_i$.
- γ (Chapter 6) – coherency factor. $\gamma = (a_{s1} - a)/(c - a) + \nu(a_{s2} - a)/(c - a) = \Phi_1 + \nu\Phi_2$ (for tetragonal film with lattice constants $a \times a \times c$ on a cubic substrate $a_{s1} \times a_{s2} \times a_{s3}$).
- $\Delta P^2(x)$ – function describing the profile of polarization square inside the wall: $\Delta P^2(x) = P_S^2 - P^2(x)$.

- $\Delta\phi$ – angle of domain wall rotation off its permissible orientation in clockwise direction.
- $\epsilon_0 = 8.85 \times 10^{-12}$ F/m – vacuum permittivity.
- ϵ_a, ϵ_c – a -misfit and c -misfit strains. $\epsilon_a = (a - a_s)/a_s, \epsilon_c = (c - a_s)/a_s$ (for tetragonal film with lattice constants $a \times a \times c$ on a cubic substrate a_s).
- ϵ_M – film-substrate misfit strain.
- ϵ_T – tetragonality factor. $\epsilon_t = (c - a)/a$ (for tetragonal film with lattice constants $a \times a \times c$).
- ϵ_{ij} – tensor of elastic deformations.
- $\epsilon_{S_{ij}}$ ($\epsilon_{S_{ij}}^{(I)}, \epsilon_{S_{ij}}^{(II)}, \epsilon_{S_{ij}}^{(a)}, \epsilon_{S_{ij}}^{(c)}$) – tensor of spontaneous deformation (in domain I, II, a, c).
- κ – dielectric constant. Case of electrically isotropic medium: κ_b . Medium of tetragonal symmetry: κ_c (measured along the polar axis), κ_a (measured normally to the polar axis).
- λ – domain wall self-energy per unit area.
- $\mu = (1/\sqrt{2\pi\xi}) \int_{-\infty}^{\infty} ((P_S^2 - P^2(x))/P_S^2) = \sqrt{2/\pi} \int_{-\infty}^{\infty} [1 - f^2(x)] dx$ – constant depending on the polarization profile in the wall.
- ν – Poisson ratio.
- ξ (Chapter 3) – correlation length.
- ξ (Chapter 6) – domain width to film thickness ratio. $\xi = w/h$.
- $\xi(x, z)$ (Chapter 7) – displacement of antiphase boundary in y -direction.
- ρ_b – density of bound charge.
- σ_{ij} – tensor of elastic stresses.
- $\sigma_{ij}^{kl}(x, y; x_0, y_0)$ – elastic stress at (x, y) generated by a unit dislocation at (x_0, y_0) having dislocation line along r_k and Burgers vector along r_l .
- Φ (Φ_1, Φ_2) – relative coherency strain. $\Phi = (a_s - a)/(c - a)$ (for tetragonal film with lattice constants $a \times a \times c$ on a cubic substrate $a_s \times a_s \times a_s$). $\Phi_1 = (a_{s1} - a)/(c - a)$, $\Phi_2 = (a_{s2} - a)/(c - a)$ (for tetragonal film with lattice constants $a \times a \times c$ on a cubic substrate $a_{s1} \times a_{s2} \times a_{s3}$).
- ϕ (Chapter 3) – electrostatic potential.
- ϕ (Chapter 4) – angle of domain wall inclination.

Contents

| | |
|---|------------|
| Acknowledgements | i |
| Abstract | iii |
| Résumé | v |
| List of designations | vii |
| 1 Introduction | 1 |
| 1.1 Outline of the thesis | 2 |
| 2 Fundamentals of ferroelectric domain structures | 5 |
| 2.1 Domain structures in ferroelectric thin films | 5 |
| 2.2 Domain walls in ferroelectric materials | 12 |
| 3 Elastic coupling between nonferroelastic domain walls | 19 |
| 3.1 Analytical description of nonferroelastic domain walls in thin freestanding films | 22 |
| 3.2 Numerical description of nonferroelastic domain walls in thin films | 25 |
| 3.3 Interwall coupling | 26 |
| 3.4 Conclusions | 28 |
| Appendix A. Derivation of the strain and stress components near the domain wall in the middle of the thin free-standing film | 29 |
| Appendix B. Coupling between polarization and strain | 32 |
| Appendix C. Electrostatic interaction of domain walls | 34 |
| 4 Mechanically incompatible ferroelastic domain walls in thin films | 37 |
| 4.1 Isolated elastic domain walls in thin films | 39 |
| 4.2 Ferroelastic domain walls in non-sparse domain structures | 46 |
| 4.3 Conclusions | 49 |
| Appendix A. Energy of interaction between dislocations | 49 |

Contents

| | |
|---|-----------|
| Appendix B. Derivation of equation (4.17) describing domain wall shape | 50 |
| 5 Inclined ferroelectric domain walls as reconfigurable metallic-like channels | 53 |
| 5.1 Theoretical description of domain wall bending | 54 |
| 5.2 Comparison with numerical simulations | 60 |
| 5.3 Comparison with experiments | 61 |
| 5.4 Conclusions | 63 |
| Appendix A. Derivation of the elastic energy vs domain wall rotation angle dependence | 63 |
| 6 Narrow ferroelastic domains and their sparse patterns in tetragonal ferroelectric thin films | 69 |
| 6.1 Stress fields around narrow a-domain inclusions from fictitious dislocation method | 70 |
| 6.2 Energetics of narrow a-domain inclusions | 73 |
| 6.3 Equilibrium and minimal a-domain widths | 76 |
| 6.3.1 Equilibrium domain width | 76 |
| 6.3.2 Minimal domain width | 77 |
| 6.4 Interaction between a-domain inclusions, equilibrium 1D pattern | 78 |
| 6.5 New periodicity scaling law | 81 |
| 6.6 Comparison with experiment | 83 |
| 6.6.1 Lattice constants of free - standing film | 83 |
| 6.6.2 Domain widths for $\text{Pb}(\text{Zr,Ti})\text{O}_3$ on DyScO_3 substrate | 86 |
| 6.7 Conclusions | 87 |
| Appendix A. Expressions for the stress field around dislocations in a semi-infinite isotropic media | 88 |
| Appendix B. Energy of interaction between two dislocations | 88 |
| 7 Moving antiphase boundaries using an external electric field | 91 |
| 7.1 Equilibrium of forces at the antiphase boundary in an electric field | 92 |
| 7.2 Displacement of an antiphase boundary induced by the electric field from an AFM tip | 94 |
| 7.3 Retainment of the antiphase boundary displacement upon removal of the electric field | 98 |
| 7.4 Conclusions | 100 |
| Appendix A. Derivation of expressions of forces p_{pe} , p_{me} | 100 |

| | |
|------------------------------|------------|
| 8 Summary and Outlook | 103 |
| 8.1 Outlook | 105 |
| Bibliography | 112 |
| List of publications | 113 |

1 Introduction

The field of ferroelectrics has gained an appreciable attention during the last many decades. The main feature of ferroelectrics is the multistability of the order parameter, polarization, which usually results from a group-subgroup phase transition under the Curie temperature. Initially, the phenomenon of ferroelectricity was discovered in 1920 in Rochelle salt by J. Valasek [1], triggering development of new types of devices implementing the unique features of ferroelectric materials. Since then, ferroelectric materials have found applications in microactuators [2], acoustic sensors [3] and transducers [4], pyroelectric detectors [5], non-volatile memories [6], and many other types of devices, with new functionality of devices in constant development and implementation.

Ferroelectric materials are typically composed of multiple regions of different ferroelectric states, the domains, that coexist with each other within the material. Domain walls (DWs), being the boundaries between domains, are essential elements of such systems. Characterized by their structure being different from the structure of the domains themselves, domain walls often behave in a different manner compared to the domains and, in certain systems, bring unique properties to the ferroelectric materials and thus are the subjects of extensive experimental and theoretical investigation. For instance, of high interest are conductive domain walls in non-conductive ferroelectrics, controllable generation and manipulation of which may have potential applications in nanoelectronics with reconfigurable electric circuits [7, 8]. Besides that, domain wall motion is known to largely enhance the piezoelectric response in certain ferroelectric materials, making a large contribution to the piezoelectric coefficient as the domains [9]. During the polarization switching process, DW motion and the interaction between them comes into play, impacting the switching speed and other dynamic properties of the process. These and some other manifestations of DWs impacting the properties of

Chapter 1. Introduction

ferroelectric materials triggers necessity of investigation of domain walls and, in general, of ferroelectric domain structures, i.e., of the structures comprised of domains and domain walls, in order to improve existing functionalities of ferroelectrics based devices and, potentially, develop devices with new functionalities.

During the large part of the 20th century, domain structures in ferroelectrics were investigated and described only in bulk crystals, which fitted well with the general trend of the time when mostly bulk ferroelectric materials were used in ferroelectrics based devices. Recently, when techniques of ferroelectric thin film fabrication advanced far enough to allow controllable growth of the films down to atomic scales, the trends have been shifted to implementation of thin films to ferroelectrics based devices and to miniaturization of the electronic devices. For description of ferroelectric domain patterns in thin films, some features of behaviour of the domain structures obtained for bulk crystals are often directly applied to the thin films since it is believed that the influence of the effects specific to thin film geometry on the domain structure behaviour can be neglected. While in most cases the application of such a consideration is reasonable, some properties of domain structures that are unique features of thin film geometry risk to be overlooked in thin films. In order to effectively implement thin films for creation of new types of devices, it is of high interest to investigate properties specific to systems of finite thickness or to other peculiarities of thin film geometry – which is the topic of this thesis.

1.1 Outline of the thesis

The introduction is followed by chapter 2 of the thesis, state of the art, where the current understanding of domain structures formation in ferroelectric bulk crystals and thin films is discussed.

In chapter 3, long-ranged elastic interaction between nonferroelastic domain walls in thin films is discussed on the example of 180° domain walls in PbTiO_3 thin films. A model taking into account couplings between polarization, electric and elastic fields is developed. Within this model, a simplified analytical description of the elastic fields around a domain wall is formulated, allowing to unveil the origins of the elastic interaction and to investigate its main features upon variation of the film thickness. The results of the analytical description are compared with a more rigorous numerical simulations for one film thickness. For this film thickness, the force of interaction of the walls is estimated.

In chapter 4, orientation of ferroelastic domain walls in thin films is investigated. Basic

mechanisms leading to violation of the principle of mechanical compatibility of the wall in thin films are formulated. The mechanisms are implemented for the theoretical description of the inclination of 71° domain walls in BiFeO_3 thin films on a substrate. For consideration of single domain wall, the shape of the wall at differing film thicknesses is investigated. For a non-sparse domain structure, the average inclination of the domain wall is studied.

In chapter 5, a theory is developed showing the basics of elasticity-driven generation of charged ferroelastic domain walls with metallic-like conductivity. To do it, the mechanisms of orientation of ferroelastic domain walls in thin films, developed in chapter 4, are applied to walls of an ultrathin a -domain inclusion in a/c -domain structure in tetragonal films on a substrate. The conductivity of the domain walls found here confirms reports of experimental observations of conductivity in $\text{Pb}(\text{Zr}, \text{Ti})\text{O}_3$ thin films.

Chapter 6 gives description of narrow domain inclusions in tetragonal films on an anisotropic (orthorhombic) substrate. A theory is developed linking the parameters of the domain pattern, such as the width of the inclusion and the equilibrium domain period, with film thickness and film-substrate lattice misfits. The output of the theory is then supported by the experimental results for $\text{Pb}(\text{Zr}, \text{Ti})\text{O}_3$ films on DyScO_3 substrate.

Chapter 7 discusses movement of antiphase boundaries with localized ferroelectricity by an external electric field. Theoretical description of PbZrO_3 antiphase boundaries is developed, necessary conditions for the displacement of the boundary by applied electric field are formulated, dependence of this displacement on the experimental parameters is studied. Besides, estimations of the retention of the displacement of the boundary on removal of the electric field are given.

2 Fundamentals of ferroelectric domain structures

Several thousands of papers have been published on observations of domain patterns in ferroelectrics and other kinds of nonmagnetic ferroics, offering a large amount of interesting data for many materials. Available data on domain patterns can be, in first approximation, classified into three categories. First, we can observe domains in a sample when its history (sample preparation, thermal record, applied forces, etc.) is not known. Second, and perhaps given in most of the papers, is when the sample has been treated using a known and/or planned procedure. In the third category, the sample quality and the external conditions (e.g., thermal history) are well defined and carefully prepared so that the resulting domain structure most likely corresponds to the minimal energy of the system; this is often referred to as the "equilibrium domain pattern". In this chapter, overview of the current development in theoretical description of the latter case, of equilibrium domain patterns, is given. The description is split into two sections. In Section 2.1, the theoretical development of the domain structures formation is given. In Section 2.2, current understanding of the properties of domain walls is described.

2.1 Domain structures in ferroelectric thin films

In most theoretical descriptions covering equilibrium patterns, the domain structures are obtained using the requirement of the minimum energy of the system. In bulk ferroelectrics, thermodynamic description shows that, in the absence of macroscopic electric field, the minimum energy of the system is attained when the ferroelectric is in the uniform single-domain state. However, in many systems containing a ferroelectric plate, the minimum of the energy can only be reached through formation of domain patterns with coexisting domain states. In this section, the basic principles of domain formation are discussed.

Chapter 2. Fundamentals of ferroelectric domain structures

Among the first, the theoretical description was given to the classical situation of 180° domain structures: a sample of uniaxial ferroelectric or of a multiaxial ferroelectric with coexisting domains having antiparallel polarizations. In the case where no external means (like short-circuited electrodes) are used to screen electric fields, the bound charges of the spontaneous polarization on the surface of the sample generate a depolarizing electric field which increases the energy of the system. The energy of the depolarizing electric field can be reduced if the sample is split into domains. At the same time, the domain formation increases the energy of the system by the energy of the appearing domain walls. All in all, the balance between these two contributions to the energy will decide whether the material splits into domains or not and determines the parameters of the domain pattern if its formation is favourable. It is clear from electrostatic arguments that if the polarization is directed along the longest macroscopic dimension of a ferroelectric sample, then the energy of the depolarizing field can be rather small and a single-domain state may be readily favourable, whereas in a ferroelectric plate with polarization normal to the plate, the energy of the depolarizing field is larger and a multidomain state is expected.

The simplest domain pattern expected in the latter case is shown in Fig. 2.1. In real systems, this pattern usually possesses no net polarization, i.e., the fractions of the opposite domains are equal, and it is dense, i.e., its period l is much smaller than the plate thickness h . For this case, the energetic consideration of the free-standing ferroelectric plate by T. Mitsui and J. Furuichi results in the following relation for the energy of the system U per plate unit area [10]:

$$U = U_{\text{dep}} + U_{\text{W}}, \quad (2.1)$$

$$U_{\text{dep}} = \frac{0.13P_S^2 l}{\epsilon_0(1 + \sqrt{\kappa_a \kappa_c})}, \quad (2.2)$$

$$U_{\text{W}} = 2\lambda \frac{h}{l}, \quad (2.3)$$

where U_{dep} is the energy of depolarizing electric fields, U_{W} is the energy of domain walls, P_S is the value of spontaneous polarization of the ferroelectric, κ_c and κ_a are the dielectric constants measured along the polarization and perpendicular to it, respectively, ϵ_0 is the vacuum permittivity, and λ is the domain wall self-energy per unit area of the wall. In the considered case, a domain structure with a smaller domain period l has a lower energy of electric fields U_{dep} . On the other hand, a more dense domain pattern means a larger amount of domain walls in the system, increasing the energy of the walls U_{W} . Thus, the period of the structure is defined by the competition between these two energy contributions. Minimizing

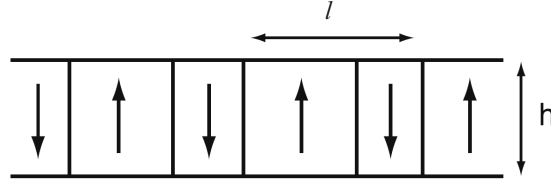


Figure 2.1: Schematics of a ferroelectric plate with lamella domain structure.

the total energy with respect to the domain period l gives the square root dependence of the equilibrium domain period $l_{\text{eq}}(h)$ on the film thickness:

$$l_{\text{eq}}(h) = \sqrt{15\epsilon_0(1 + \sqrt{\kappa_a\kappa_c})\lambda/P_S^2} \cdot \sqrt{h}. \quad (2.4)$$

A square root dependence similar to that in Eq. (2.4) is known as the Kittel law in magnetic systems; in ferroelectric systems it is commonly referred to as the Kittel – Mitsui – Furuichi law. Universally, the square root dependence of the domain period on the film thickness is often observed in other ferroelectric systems with dense patterns, governed by electrostatics or by other mechanisms (e.g., elasticity).

In real systems, notably in thin films on a substrate, the domain structure formation is mostly driven by elasticity. The key difference between a mechanically free bulk material and a thin film made of the same material deposited on a dissimilar substrate, is that the film is clamped, e.g., due to the difference in the lattice parameters of the film and of the substrate. The problem of domain formation driven by elastic effects in thin films of ferroics was pioneered by Roytburd [11] and later treated by many workers. These studies have made available a good qualitative and, in many cases, quantitative mathematical description of the phenomenon. The progress has been achieved using a number of approaches such as: (i) consideration of dense periodical domain structures (the domain period smaller than the film thickness) using the average mechanical energy of the systems as the basic approximation (e.g., [11]); (ii) calculations based on analytical results for elastic Green functions (e.g., [12]); (iii) calculations using fictitious dislocations for the description of the deformation fields (e.g., [13–16]); (iv) Landau theory of the dense domain pattern (e.g., [17]); and (v) phase-field calculations based on Ginzburg–Landau theory ([18, 19]). Here, the basic theoretical development implementing approaches (i) and (iii) is given on an example of a tetragonal film on a cubic substrate.

In general, domain formation driven by elastic effects can be described by the energy of

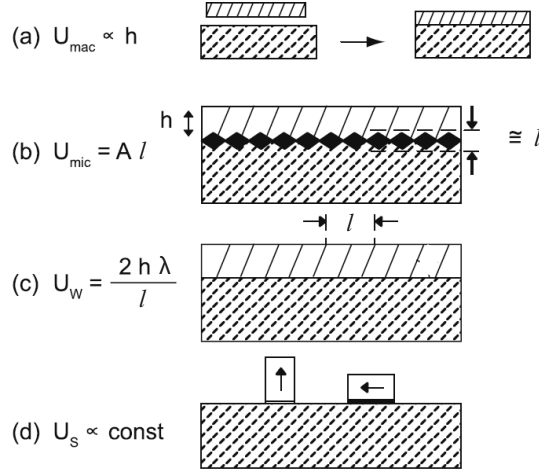


Figure 2.2: Schematic representation of the contributions to the electric energy of a dense periodic ferroelectric domain pattern. (a) Energy of the average (macroscopic) strain. (b) Energy of microstresses at the film-substrate interface. (c) Energy of the domain walls. (d) Contribution related to the difference in the energy of the film-substrate interface for the domain states involved in the pattern. Dashed line-hatched areas show substrate. Open areas show ferroelectric film. Systems of parallel lines show ferroelectric domain walls. Arrows in (d) show the orientation of a crystallographic direction of the material in the different ferroelectric domain states

the structure U that can be presented in the form [20]:

$$U = U_{\text{mac}} + U_{\text{mic}} + U_{\text{W}} + U_{\text{S}}, \quad (2.5)$$

where U_{mac} , U_{mic} , U_{W} , and U_{S} are the elastic energy corresponding to the average (macroscopic) strain in the system, the energy of microstresses at the film/substrate interface, the energy of the domain walls, and the contribution related to the difference in the energy of the film/substrate interface for the different domain states. These contributions are schematically illustrated in Fig. 2.2.

Basics of the elasticity-driven domain pattern formation can be elucidated by considering the macroscopic contribution U_{mac} to the elastic energy of the system [11]. For example, in a tetragonal (001) film (lattice constants along three directions a , a , and c) on a cubic substrate (lattice constant a_s), domain states are characterized by one of the three orientations of the c -direction of the unit cell of the film: along [100] (domain state a_1), [010] (domain state a_2), and [001] (domain state c) crystallographical directions. In a (001) film, each of the domain

states is described by its misfit strain ϵ_M :

$$\epsilon_M^{(a_1)} = \begin{pmatrix} \epsilon_c & 0 \\ 0 & \epsilon_a \end{pmatrix}, \quad \epsilon_M^{(a_2)} = \begin{pmatrix} \epsilon_a & 0 \\ 0 & \epsilon_c \end{pmatrix}, \quad \epsilon_M^{(c)} = \begin{pmatrix} \epsilon_a & 0 \\ 0 & \epsilon_a \end{pmatrix}, \quad (2.6)$$

where $\epsilon_a = (a - a_s)/a_s$, $\epsilon_c = (c - a_s)/a_s$.

In the description developed by Roytburd [11] for dense domain patterns, the elastic part of the energy of the structure is defined by the average strain of the film ϵ_M^{av} :

$$\epsilon_M^{\text{av}} = \alpha_1 \epsilon_M^{(a_1)} + \alpha_2 \epsilon_M^{(a_2)} + \alpha_3 \epsilon_M^{(c)}, \quad (2.7)$$

where α_1 , α_2 , and α_3 are the volume fractions of domains a_1 , a_2 , and c in the structure, respectively, $\alpha_1 + \alpha_2 + \alpha_3 = 1$.

Within the approach of the mean strain, the elastic energy U_{mac} of the elastically isotropic film clamped on the substrate can be found as follows [12]:

$$U_{\text{mac}} = \frac{1}{2} \frac{E}{1 - \nu^2} \left((\epsilon_{M_{11}}^{\text{av}})^2 + (\epsilon_{M_{22}}^{\text{av}})^2 + 2\nu \epsilon_{M_{11}}^{\text{av}} \epsilon_{M_{22}}^{\text{av}} \right), \quad (2.8)$$

where E is the Young modulus, ν is the Poisson ratio of the material. Minimization of the elastic energy of the structure gives the equilibrium relationship between volume fractions α_1 , α_2 , and α_3 , depending on the film-substrate misfit strains ϵ_a , ϵ_c . The results of this analysis are summarized in Fig. 2.3, where four cases of the misfit stress relaxation by the domain structure are considered [20]. Diagram #1 shows the case where only a and c domain monovariants are allowed in the structure: either $\alpha_1 = 1$ (a_1 monovariant), or $\alpha_2 = 1$ (a_2 monovariant), or $\alpha_3 = 1$ (c monovariant). Due to the symmetry of the problem, elastic energies of a_1 and a_2 monovariants are equal. Diagram #2 shows the possible appearance of the a/c domain structure leading to a more efficient release of the misfit strain: either $\alpha_1 \neq 0$ and $\alpha_3 = 1 - \alpha_1 \neq 0$, or $\alpha_2 \neq 0$ and $\alpha_3 = 1 - \alpha_2 \neq 0$. Diagram #3 takes into account strain release by the a_1/a_2 -variant: $\alpha_1 = 1/2$, $\alpha_2 = 1/2$, $\alpha_3 = 0$. Finally, diagram #4 allows the appearance of three-domain-state structures: $\alpha_1 = \alpha_2 \neq 0$, $\alpha_3 \neq 0$. It was shown that such gradual introduction of new types of domain structures, allowing to move from diagram #1 to diagram #4, leads, in general, to a gradually more efficient release of the misfit stresses in the film.

The investigation of the properties of dense domain structures at differing film thicknesses leads to the Kittel-like square root dependence of the domain period on the film thickness. This and some other results obtained within this consideration, such as the volume fraction of

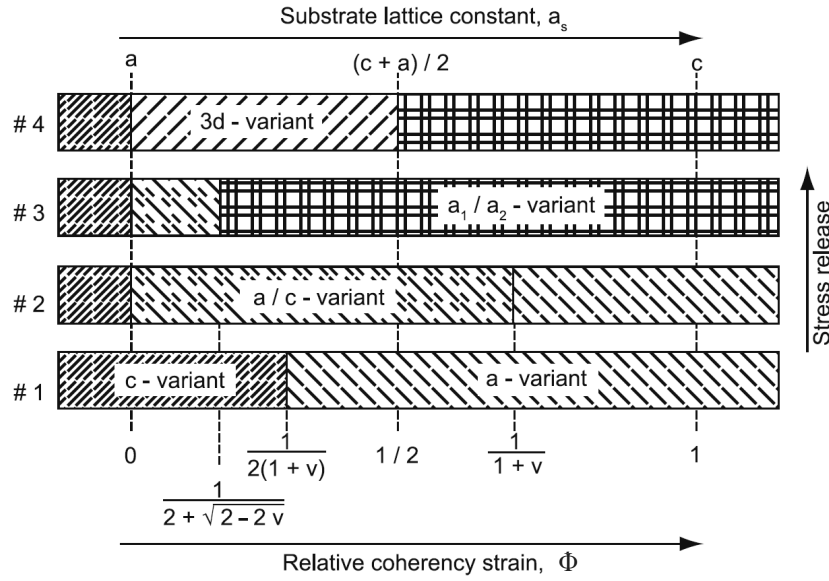


Figure 2.3: Diagram shows the domain states or domain patterns having the minimal average (macroscopical) elastic energy in a (001) tetragonal ferroelectric film as functions of the relative coherence strain, $\Phi = (a_s - a)/(c - a)$. The corresponding values of the substrate lattice constants are also shown. The "3d-variant" stands for the three-domain-state structure. ν is the Poisson ratio. See the text for the description of diagrams #1, #2, #3, #4.

domains in different domain structures, are shown in Fig. 2.4 by dashed lines.

Though the obtained results provide a good coverage of the typical experimental situations, they are still limited since the approach itself is applicable only if the domain structure of the film is dense, i.e., if the period of the structure is smaller than the film thickness. This condition is always violated when the film thickness is smaller than the critical thickness specific for the considered geometry, or when the fraction of one of the domain states tends to zero ($\alpha_1 \rightarrow 0$, $\alpha_2 \rightarrow 0$ or $\alpha_3 \rightarrow 0$). Description of the domains in these situations as well as the evaluation of the accuracy of the mean-strain approach calls for a more precise treatment of the problem.

New types of approaches to the problem, implementing advanced methods of the theory of elasticity, were offered by several authors. Three kinds of problems were addressed: (i) calculation of elastic energy of the a/c -variant [12, 14], (ii) calculation of elastic energy of the a_1/a_2 -variant [12, 14, 15], and (iii) calculation of elastic energy of an a -domain band inserted in a large c -domain [12]. All the problems were addressed in the approximation of elastic isotropy of both the ferroelectric film and the substrate, whose elastic constants were taken identical. The calculations performed in these problems involved usage of method of fictitious dislocations and disclinations by Pertsev et al [14, 16], by Romanov with coworkers

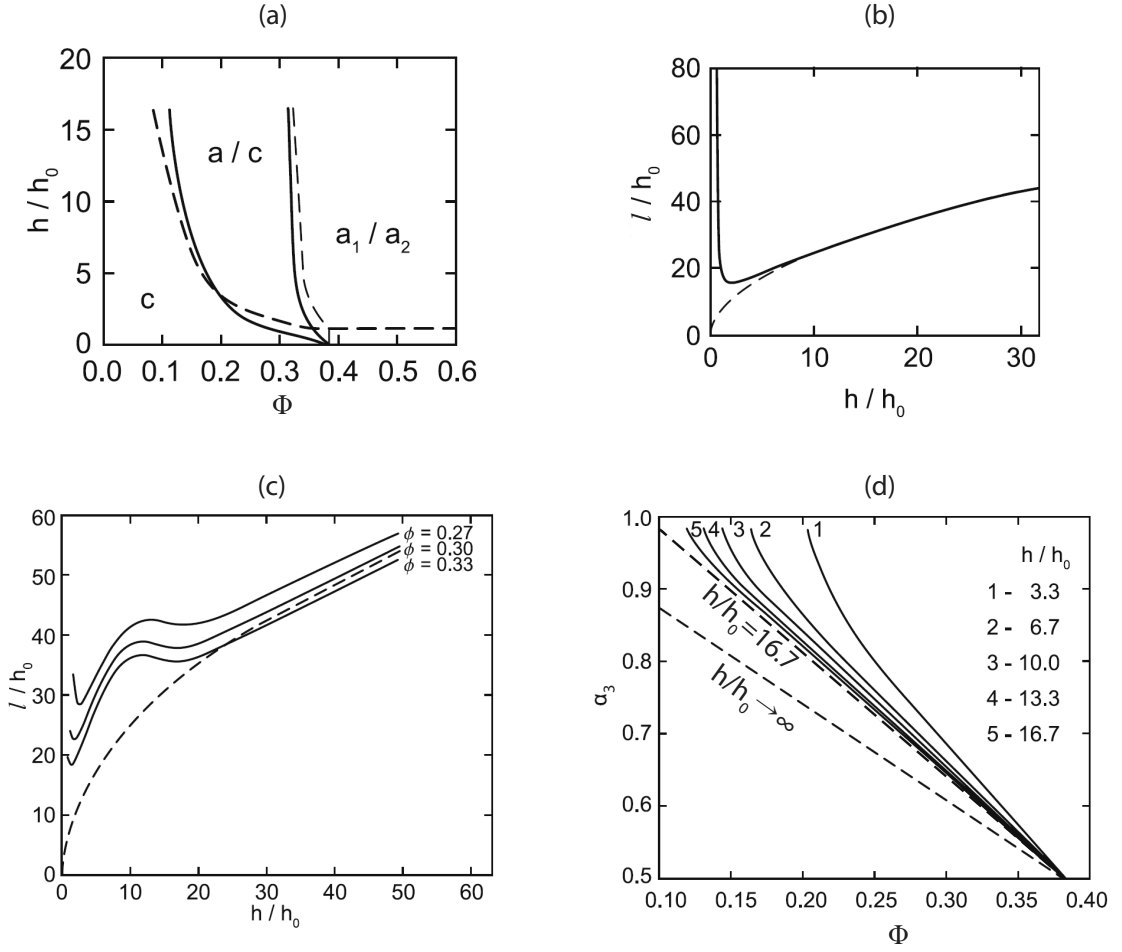


Figure 2.4: Results of the mean-strain approach for domain structures in (001) tetragonal ferroelectric film on a cubic substrate, compared with the results of numerical calculations [14] taking into account the exact stress distribution in the film. All lengths are normalized on the characteristic film thickness $h_0 = 6.1\lambda(1 - \nu^2)a^2 / (E(c - a)^2)$. (a) Energetically favourable type of the domain variant at different normalized film thicknesses h/h_0 and coherency strains $\Phi = (a_s - a)/(c - a)$. Dashed lines show the predictions of the mean-strain theory. Solid curves – the results of the numerical calculations [14]. Structures having maximum two domain states are considered. (b) Normalized period l/h_0 of the a_1/a_2 -domain pattern as a function of the normalized film thickness. Dashed line – the 'square root law', which, in the limit of large film thickness, is consistent with the results of the mean-strain approach. Solid curves – the results of the numerical calculations [14]. (c) Normalized period of the a/c-domain pattern at differing normalized film thicknesses. Dashed line – the 'square root law' which, in the limit of large film thickness, is consistent with the results of the mean-strain approach with relative coherence strain $\Phi = 0.3$. Solid curves – the results of the numerical calculations [14] for different values of the relative coherence strain Φ . (d) Effect of the film thickness on the dependence of the volume fraction of the c-domain state, α_3 , on the relative coherence strain, Φ . The a/c-domain pattern is considered. Dashed lines – the results of the mean-strain approach for $h/h_0 = 16.7$ and in the limit $h/h_0 \rightarrow \infty$. Curves 1–5 show the results of numerical calculations [14] for the normalized thicknesses $h/h_0 = 3.3, 6.7, 10, 13.3, 16.7$, respectively.

[15], and usage of elastic Green functions by Pompe et al [12]. For the case of a film of an arbitrary thickness the rigorous results can be derived only numerically. For the a_1/a_2 -pattern, Romanov and coworkers [15] offered an approximate analytical treatment of the problem. The technical aspects of the theory of dislocations will be presented in Chapters 4, 5, 6. The results of these investigations are summarized in Fig. 2.4 (solid lines), where they are given in comparison with the results obtained in the framework of dense-pattern theory.

2.2 Domain walls in ferroelectric materials

Domain walls are essential elements of domain structures. In equilibrium domain patterns, the properties of the walls (such as the wall orientation, internal structure, etc.) are defined by the condition of the minimal energy of the wall in the structure. In general, one can specify following factors controlling the orientation of the wall separating a domain pair: (i) electrostatic energy related to differently oriented vectors of polarization in the neighbouring domains (usually referred to as the electrical compatibility problem); (ii) elastic energy related to differing spontaneous strains in neighbouring domains (usually referred to as the mechanical compatibility problem); (iii) energy of the wall itself. In most practical situations, factors (i) and (ii) play the decisive role. Here the current theoretical development for description of these two factors is given.

An arbitrarily oriented domain wall between ferroelectric domains, in general, carries a bound charge whose density ρ_b , according to the Poisson equation, equals

$$\rho_b = -\text{div}\mathbf{P}. \quad (2.9)$$

The existence of this charge typically leads to the generation of electric fields associated with the bound charges and to increase of the energy of the system. In this case, orientation of the wall corresponding to the minimal energy of the system is defined by the condition of its electric neutrality ($\rho_b = 0$). For a wall with normal vector \mathbf{n} , separating two domains characterized by spontaneous polarization vectors \mathbf{P}_S^I and \mathbf{P}_S^{II} , the condition of the wall neutrality reads

$$(\mathbf{P}_S^I - \mathbf{P}_S^{II})\mathbf{n} = 0. \quad (2.10)$$

In principle, the bound charges on the wall can be compensated by free carriers. If this is not the case, then, for a bulk sample containing a charged domain wall, the electrostatic energy of the electric fields generated by the bound charges recalculated to the unit area of

the wall results in a large increase of the domain wall surface energy density. In this situation, the condition of electric neutrality should be strictly fulfilled. In principle, there can be other contributions to the energy of the system that can compensate the increase of the electric energy. However, the electric field created by a charged wall not only contributes to the energy of the system, but may also suppress ferroelectricity in the neighbouring domains [21], limiting the maximum value of surface charge density beyond which the wall cannot exist. Applied to the problem of the wall orientation, as was pointed out by Chervonobrodov and Roytburd [22], this defines the limit to a small possible deviation of the wall from the orientation of its electric neutrality.

For a ferroelastic domain pair, the requirement of mechanical compatibility also imposes restrictions on the orientation of the domain wall. For a generally oriented wall between domains having different spontaneous strain tensors, there is typically a lattice mismatch between domains which induces elastic strains increasing the elastic energy of the system. The condition of the minimal elastic energy of the system implies the absence of such elastic fields, and can be expressed mathematically as follows. Let the spontaneous strain in the domains be $\epsilon_S^{(I)}$ and $\epsilon_S^{(II)}$; then the transformation of any geometrical figure lying in the plane of the wall due to the deformations described by the tensors $\epsilon_S^{(I)}$ and $\epsilon_S^{(II)}$ should be identical up to a rigid body motion. Domain walls oriented so that this condition is met are sometimes called permissible or, alternatively, stress-free walls, since no additional macroscopic elastic strains are involved in their formation. Mathematically, the mentioned condition requires that for any vector $\boldsymbol{\tau}$ lying in the plane of the wall the following condition be fulfilled [23, 24]:

$$\Delta_{ij} \tau_i \tau_j = 0, \quad (2.11)$$

$$\Delta_{ij} = \epsilon_{S_{ij}}^{(I)} - \epsilon_{S_{ij}}^{(II)}, \quad (2.12)$$

where Δ_{ij} is the tensor describing the difference between the spontaneous deformations of the domains.

One can distinguish four different cases of the domain boundaries, depending on the relationships between the components of the tensor Δ_{ij} . Note that the matrix Δ_{ij} is symmetric, thus there exist a reference frame where it can be rewritten in diagonal form, with eigenvalues $\Delta^{(1)}$, $\Delta^{(2)}$, and $\Delta^{(3)}$. Since the volumes of the unit cells in the domains are the same, the trace of Δ_{ij} is zero, and $\Delta^{(1)} + \Delta^{(2)} + \Delta^{(3)} = 0$.

(i) If all principal components $\Delta^{(i)}$ are zero, which means $\epsilon_S^{(I)} = \epsilon_S^{(II)}$, then the domain wall separates a nonferroelastic domain pair, and at any orientation the wall is stress-free.

Chapter 2. Fundamentals of ferroelectric domain structures

(ii) If only one of the principal components of Δ_{ij} is zero (e.g., $\Delta^{(1)} = 0$), then $\Delta^{(2)} = -\Delta^{(3)}$ and, in the principal axes of the matrix Δ_{ij} , Eq. (2.11) reads

$$\tau_2^2 - \tau_3^2 = 0, \quad (2.13)$$

defining two permissible walls which are mutually perpendicular. Here, in addition, if the principal axes are directed along crystallographic directions of the material, then the wall has a crystallographically prominent orientation.

(iii) If, similarly to the case (ii), one of the principal components of Δ_{ij} is zero, but the matrix Δ_{ij} is not diagonal in the crystallographic reference frame, the orientation of the walls is not crystallographically prominent and is controlled by the relation between the components of the matrix. In this case, the permissible wall has a general orientation which in fact can change with the temperature due the temperature dependence of the spontaneous strains of the domains. Permissible walls of this kind have been denoted as "S walls" [23] – at the time of their prediction it was generally believed that any permissible wall must be crystallographically prominent, and the prefix S stood for "strange".

(iv) If none of $\Delta^{(i)}$ equals zero and therefore $\det \Delta_{ij} \neq 0$, then Eq. (2.11) has no non-trivial solutions and the two domains cannot be separated by a stress-free wall. These situations are usually referred to as *R cases*.

Even if the relationship between components of the tensor Δ_{ij} falls into the category (ii) or (iii), it is still possible that permissible walls are not allowed in the system due to the effects of electrostatics. If the orientation of the wall leads to a charged domain wall ($\rho_b \neq 0$ in Eq. (2.9)), such a wall is, in general, energetically unfavourable. Thus, the orientation of a ferroelastic walls is defined by both electrostatic and mechanical principles.

In bulk materials, the condition of mechanical compatibility of an electrically neutral ferroelastic domain wall given by Eq. (2.11) must be followed strictly, since a deviation of the wall off its permissible orientation leads to appearance of lattice mismatches on the wall and to generation of macroscopic stresses essential rising the elastic energy of the system. At the same time, strictly speaking, in thin films the increase of the elastic energy associated with the wall deviation is relatively small, and it is possible that other mechanisms can compensate this increase of the energy. Due to the lack of theoretical descriptions of such mechanisms, it is of interest to investigate the question of possible existence of mechanically incompatible domain walls in thin films.

2.2. Domain walls in ferroelectric materials

For nonferroelastic domain pairs, the matching of the domains lattices is assured for all orientations of the wall, and no macroscopic stresses are generated by the wall. Thus, in practice, it is usually assumed that the properties of nonferroelastic domain walls are not influenced by elastic effects. It is important to remember though that, following investigations of the internal structure of nonferroelastic walls, there is often a presence of internal stresses confined within the domain wall width that are originated by the effect of electrostriction [20].

The basics of the internal structure of a nonferroelastic domain wall can be shown on example of a 180° domain wall in tetragonal BaTiO₃-like structure with one domain wall, characterized by the second order cubic to tetragonal phase transition at the Curie temperature. For this system, theoretical development in the framework of thermodynamic approach gives the following expression for the Gibbs potential density G in Cartesian coordinate system (z (r_3) axis is directed along the polarization, x (r_1) axis is directed normally to the domain wall):

$$G = \frac{1}{2}\alpha P^2 + \frac{1}{4}\beta P^4 - \frac{1}{2}s_{11}(\sigma_{11}^2 + \sigma_{22}^2 + \sigma_{33}^2) - s_{12}(\sigma_{11}\sigma_{22} + \sigma_{22}\sigma_{33} + \sigma_{33}\sigma_{11}) - \frac{1}{2}s_{44}(\sigma_{12}^2 + \sigma_{23}^2 + \sigma_{13}^2) - Q_{11}\sigma_{33}P^2 - Q_{12}(\sigma_{11} + \sigma_{22})P^2 + g_{44}\left(\frac{\partial P}{\partial x}\right)^2, \quad (2.14)$$

where α and β are the second and the fourth order dielectric stiffnesses, respectively, s_{ij} is the compliance tensor in Voigt notations, Q_{ij} is the electrostriction tensor in Voigt notations, g_{ij} is the correlation energy tensor in Voigt notations, $P(x)$ and $\sigma_{ij}(x)$ are the polarization and the stress profiles inside the wall, respectively. Equations obtained by minimization of the Gibbs potential along with the constitutive equations for the problem form the following set of relationships describing polarization and elastic stresses inside the wall:

$$\frac{\partial G}{\partial P} = \frac{d}{dx} \left(\frac{\partial G}{\partial (dP/dx)} \right), \quad (2.15)$$

$$\frac{\partial G}{\partial \sigma_{ij}} = -\epsilon_{ij}, \quad (2.16)$$

$$e_{ikm}e_{jln} \frac{\partial^2 \epsilon_{ij}}{\partial r_k \partial r_l} = 0, \quad (2.17)$$

$$\frac{\partial \sigma_{ij}}{\partial r_j} = 0, \quad (2.18)$$

where $\epsilon_{ij}(x)$ is the strain profile inside the wall, e_{ijk} is the Levi-Civita permutation symbol.

Rewriting this set of equations for a ferroelectric of the infinite size (see, e.g., [20] for details) leads to the following relationships coupling polarization with elastic stresses (only

Chapter 2. Fundamentals of ferroelectric domain structures

non-zero stress components are shown):

$$\sigma_{22}(x) = \frac{s_{11}Q_{12} - s_{12}Q_{11}}{s_{11}^2 - s_{12}^2} (P_S^2 - P^2(x)), \quad (2.19)$$

$$\sigma_{33}(x) = \frac{s_{11}Q_{11} - s_{12}Q_{12}}{s_{11}^2 - s_{12}^2} (P_S^2 - P^2(x)), \quad (2.20)$$

$$-g_{44} \frac{\partial^2 P}{\partial x^2} + B(\alpha P + \beta P^3) = 0, \quad (2.21)$$

$$B = 1 + \frac{1}{\beta} \left(\frac{(Q_{11} + Q_{12})^2}{s_{11} + s_{12}} + \frac{(Q_{11} - Q_{12})^2}{s_{11} - s_{12}} \right), \quad (2.22)$$

where $P_S = \sqrt{-\alpha/\beta}$ is the value of spontaneous polarization inside the domains.

Thus, in the considered domain wall, the electrostrictive coupling between elastic field and polarization generates elastic stresses inside the wall, which reach their maximal values when $P = 0$. Solution to the equation for the polarization profile (2.21) is described by the classical hyperbolic tangent function:

$$P(x) = P_S \tanh\left(\frac{2x}{t_W}\right), \quad (2.23)$$

$$t_W = \sqrt{-\frac{8g_{44}}{B\alpha}}, \quad (2.24)$$

where t_W is the thickness of the wall.

It is important to note that, when describing the nonferroelastic domain walls internal structure, the influence of the stresses inside the wall on the structure of the wall is very often omitted for the sake of simplicity. In this case, when the effect of electrostriction is not taken into consideration, the governing equation on polarization inside the wall has the same form as Eq. (2.21) with constant $B = 1$, and the solution to this equation gives the same order of magnitude for the domain wall thickness t_W . Due to the nonferroelastic nature of the wall, it is universally considered that, except for renormalization of the width of the wall, there is no influence of elastic effects on the nonferroelastic domain walls.

At the same time, investigation of solution for stresses (2.19)–(2.20) obtained for an infinite crystal shows that it is not applicable to real non-infinite ferroelectric structures. When the finiteness of the sample is taken into consideration, it is clear that at the edges of the sample either $\sigma_{22} \neq 0$ or $\sigma_{33} \neq 0$ inevitably breaks the free surface mechanical boundary conditions, implying that in real systems the structure of a nonferroelastic domain wall cannot be described by the one-dimensional solution given by Eqs. (2.19), (2.20), and (2.23). In other words, elastic properties of the nonferroelastic domain wall may depend on the macroscopic

2.2. Domain walls in ferroelectric materials

dimensions of the sample, which is an interesting point for theoretical investigation.

A remark should be made, that all the properties of domain walls described in this Section were obtained considering a ferroelectric of infinite size containing a single domain wall. The question of the applicability of such results to real ferroelectric films of small thicknesses has not been studied by the scientific community. There are few works that investigate some features of domain walls in near-surface regions, e.g., variation of internal structure of the wall near the surface [25]. As a consequence, the properties of domain walls obtained for ferroelectric bulk materials described in this section are usually applied to thin film geometries as well. It is of interest to investigate features of domain walls specific to the thin film geometry. This thesis gives description to some of the features.

3 Elastic coupling between nonferroelastic domain walls

Domain walls are an essential attribute of ferroics. Their motion controls to a large extent switching and other properties of ferromagnets and ferroelectrics [20]. The internal structure and properties of the domain walls themselves, accessible at ease only in recent years, are of an increasing interest for both fundamental and applied research [26–31].

The well-known correlation between film thickness and domain wall spacing entails that interactions between adjacent domain walls become substantial upon reduction of the film thickness. Such interaction can be of particular importance for polarization switching where, inevitably, domain walls have to approach closely each other. The interwall interaction was actually taken into account by calculations in [14, 32], where the results can be interpreted as the consequence of coupling between ferroelastic (non 180°) domain walls, and possibly detected experimentally as well [33]. However, interactions between nonferroelastic (180°) domain walls have been overlooked. Possible interactions between ferroelectric-nonferroelastic domain walls are of high interest since the switching processes in ferroelectric thin films are mainly determined by the motion of nonferroelastic walls because ferroelastic walls typically show poor mobility [34]. Interaction between domain walls is also highly relevant for domain-wall-based agile electronics where it is crucial to precisely control the domain wall's position and movement [7].

This chapter addresses the internal structure of nonferroelastic 180° walls in ferroelectric thin films and its influence on the interaction between these walls. It is shown that 180° domain walls in ferroelectric films can exhibit an internal structure which is very different from that in the bulk counterparts. It is found that the elastic fields associated with the wall extend to a distance comparable with the film thickness, which, in typical situations, is much larger than domain wall thickness in the bulk material. Such elastic fields naturally bring about

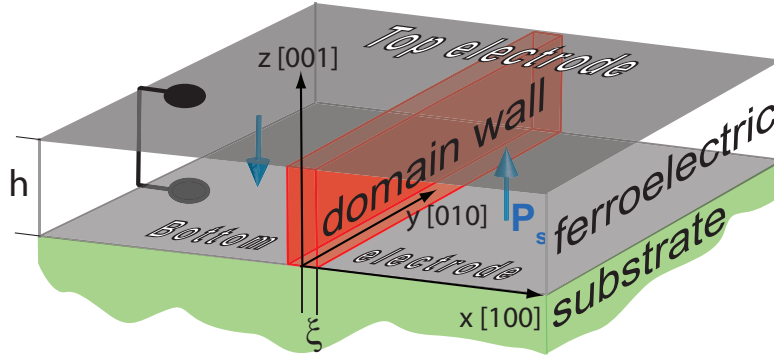


Figure 3.1: Schematic of the problem: thin film of thickness h with a domain wall in the region $x \in (-\xi, \xi)$ on a substrate of thickness h_s in the region $(-h_s < z < 0)$. Two cases considered: $h_s = 0$ (free standing film) and $h_s \gg h$ (film on a substrate).

an appreciable interaction between domain walls. An essential feature of the results is that they have been obtained for a 180° ferroelectric-nonferroelastic wall, while the elastic effects in thin films were commonly expected so far to be important only for ferroelectric-ferroelastic walls.

The predicted effects can be viewed as an impact of the film surface on the domain wall structure. Some surface effects were theoretically addressed in the past, reporting the distortion of the wall structure at distances from the surface comparable with the domain wall thickness [25, 35]. In this chapter, in contrast, a strong modification of the elastic structure of the wall throughout the whole film thickness is shown, implying an appreciable interwall coupling.

In the following, first a simple analytical model is considered for the elastic structure of a 180° wall for the case of a freestanding thin film. This simple treatment captures the principal features of the phenomenon both in freestanding thin films and in films on substrates and allows a simple qualitative explanation of the effect to be given. Then the results of a numerical simulation of the wall structures are presented in freestanding films and in films on substrates using an advanced model. Based on these results the interwall coupling is evaluated to show that the force applied to the wall due to this coupling can be comparable to that due to the applied electric field in the switching regime. The modelling addresses the short-circuited situation for the geometry with top and bottom electrodes, common for applications of ferroelectric thin films. In this situation, the electrostatic effects are strongly suppressed and are negligible with respect to the elastic effects in question.

Consider a perovskite ferroelectric film of thickness h in the tetragonal phase, either

freestanding or placed on a substrate of thickness $h_S \gg h$ (Fig. 3.1). Both top and bottom (001) surfaces are electroded and short circuited. This model corresponds to a typical ferroelectric-film-based device where the average depolarizing fields are screened. The film contains one 180° nonferroelastic domain wall oriented along the (100) crystallographic plane and normal to the surface. To describe the elastic effects around the domain wall, the thermodynamic Landau theory is used. The Cartesian reference frame is introduced with axes x, z (r_1, r_3) directed as shown in Fig. 3.1. The Gibbs potential density in a perovskite ($0 < z < h$) with cubic to tetragonal phase transition ($m\bar{3}m - 4mm$) can be written in the form [20]

$$G = \frac{1}{2}\alpha P_z^2 + \frac{1}{4}\beta P_z^4 + \frac{1}{6}\gamma P_z^6 - \frac{1}{2}s_{11}(\sigma_{11}^2 + \sigma_{22}^2 + \sigma_{33}^2) - s_{12}(\sigma_{11}\sigma_{22} + \sigma_{22}\sigma_{33} + \sigma_{33}\sigma_{11}) - \frac{1}{4}s_{44}\sigma_{13}^2 - Q_{12}(\sigma_{11} + \sigma_{22})P_z^2 - Q_{11}\sigma_{33}P_z^2 + \frac{1}{2}g_{44}\left(\frac{\partial P_z}{\partial x}\right)^2 + \frac{1}{2}g_{11}\left(\frac{\partial P_z}{\partial z}\right)^2, \quad (3.1)$$

where P_i is the ferroelectric contribution to the dielectric polarization, σ_{ij} is the stress tensor, α, β , and γ are the 2nd, 4th, and 6th order dielectric stiffnesses, correspondingly, g_{ij} is the correlation energy tensor, s_{ij} is the compliance tensor, and Q_{ij} is the electrostriction tensor. Here, Voigt notation is used for compliance, electrostriction, and correlation energy tensors. For the case of a film on a nonferroelectric substrate, the Gibbs potential in the substrate ($-h_S < z < 0$) can be written in the same form as in (3.1) with $P_z = 0$, leaving only elastic terms.

The set of equations to be solved can be obtained from the Gibbs potential using relationships (see, e.g., [20]):

$$\frac{\partial G}{\partial P_i} - \frac{\partial}{\partial r_j} \left(\frac{\partial G}{\partial P_{i,j}} \right) = -\frac{\partial \phi}{\partial r_i}, \quad (3.2)$$

$$\frac{\partial}{\partial r_i} (-\kappa_b \epsilon_0 \frac{\partial \phi}{\partial r_i} + P_i) = 0, \quad (3.3)$$

$$-\frac{\partial G}{\partial \sigma_{ij}} = \epsilon_{ij}, \quad e_{ikm} e_{jln} \frac{\partial^2 \epsilon_{ij}}{\partial r_k \partial r_l} = 0, \quad \frac{\partial \sigma_{ij}}{\partial r_j} = 0, \quad (3.4)$$

where ϕ is the electrostatic potential defined at $0 < z < h$, $\epsilon_{ij} = (u_{i,j} + u_{j,i})/2$ is the strain tensor, u_i is the deformation vector, κ_b is the background dielectric constant, ϵ_0 is the vacuum permittivity, and e_{ijk} is the Levi-Civita symbol. Hereafter $A_{i,j}$ denotes derivative of A_i with respect to r_j . The symmetry of the problem allows a 2D treatment with all values dependent on x, z only.

3.1 Analytical description of nonferroelastic domain walls in thin freestanding films

First, the case of a freestanding film is considered with electroded and short-circuited surfaces, with boundary conditions:

$$P_z(x \rightarrow \pm\infty) = \pm P_S, \quad (3.5)$$

$$\phi(z = 0) = 0, \quad \phi(z = h) = 0, \quad (3.6)$$

$$\sigma_{ij}(x \rightarrow \pm\infty) = 0, \quad (3.7)$$

$$\sigma_{13}(z = h) = 0, \quad \sigma_{33}(z = h) = 0, \quad (3.8)$$

$$\sigma_{13}(z = 0) = 0, \quad \sigma_{33}(z = 0) = 0, \quad (3.9)$$

where P_S is the spontaneous polarization value.

To capture the main features and obtain an analytical description for the effect, the polarization is presented in the form $P(x, z) = P_b(x) + P_1(x, z)$, where $P_b(x)$ is the solution to the polarization profile in a domain wall in the bulk system and $P_1(x, z)$ is the correction related to the finite film thickness. When calculating the elastic fields near the domain wall that arise due to the electromechanical coupling, the impact of $P_1(x, z)$ is neglected compared to that of $P_b(x)$. As it will be seen later, such approximation provides a qualitatively correct picture of the phenomenon. Besides, the problem is solved in the approximation of elastically isotropic media ($s_{44} = 2s_{11} - 2s_{12}$) which is also a reasonable approximation¹ for perovskite ferroelectrics (cf. [14]).

The solution for the bulk media may be formally obtained from Eqs. (3.2)–(3.5), and (3.7) as a limiting case $h \rightarrow \infty$, for which a 1D treatment is applicable (see, e.g., [25]). For a domain wall in the bulk, the polarization profile $P_b(x)$ can be presented as

$$P_b(x) = P_S f\left(\frac{x}{2\xi}\right), \quad (3.10)$$

where ξ is the correlation length (2ξ has the meaning of the half-width of the wall), and $f(x)$ is the function describing the polarization profile: $f(x \rightarrow \pm\infty) = \pm 1$. For example, for ferroelectrics having second order phase transition not very close to a tricritical point, $f(x) = \tanh(x)$.

¹The present analysis is restricted to the isotropic case for simplicity. Numerical simulations confirm that the results for the isotropic case differ only slightly from that for the parameters of PbTiO_3 with low elastic anisotropy.

3.1. Analytical description of nonferroelastic domain walls in thin freestanding films

To trace the elastic effects around the domain wall, the relative strain $\epsilon_{ij}^r = \epsilon_{ij} - \epsilon_{ij}^D$ is introduced, where ϵ_{ij}^D is the strain in the bulk of the domains. For bulk samples and freestanding films, ϵ_{ij}^D is equal to the spontaneous strain $\epsilon_{Sij} = Q_{ij33}P_S^2$. In the case of the bulk material, in view of clamping of all the other strain components by surrounding domains, the only nonzero relative strain component is ϵ_{11}^r :

$$\epsilon_{11}^{r,b}(x) = -\epsilon_{11}^0 \frac{\Delta P^2(x)}{P_S^2}, \quad (3.11)$$

$$\epsilon_{11}^0 = \frac{s_{11}^2 + s_{11}s_{12} - 2s_{12}^2}{s_{11} + s_{12}} q_{12} P_S^2. \quad (3.12)$$

Here the notation $\Delta P^2(x) = P_S^2 - P_b^2(x)$ is used, q_{ij} is the electrostrictive strain coefficient (tensor in Voigt notation) determined as $s_{ijmn}q_{mnl} = Q_{ijkl}$, and ϵ_{11}^0 is the strain in the middle of the wall. It is seen that for a domain wall in the bulk system, the spacial scales for the polarization profile [Eq. (3.10)] and for the deformation [Eq. (3.11)] are the same and determined by the correlation length ξ .

For thin film geometry, according to the aforementioned model, the bulk polarization profile $P_b(x)$ is used in Eq. (3.1), and thus the problem is reduced to the elastic subproblem (3.4) with boundary conditions (3.7)–(3.9). The solution can be found in the framework of the plane-stress approach using stress functions [36, 37]. For typical film thicknesses where $h \gg \xi$, one obtains the solution for the relative in-plane strain component in the middle of the film (see Appendix A):

$$\epsilon_{11}^r(x, h/2) = \epsilon_{11}^0 \left(-\frac{\Delta P^2(x)}{P_S^2} + \mu R \frac{\xi}{h} g_1\left(\frac{x}{h}\right) \right). \quad (3.13)$$

Here,

$$\mu = \frac{1}{\sqrt{2\pi}\xi} \int_{-\infty}^{\infty} \frac{\Delta P^2(x)}{P_S^2} dx = \sqrt{\frac{2}{\pi}} \int_{-\infty}^{\infty} (1 - f^2(x)) dx \quad (3.14)$$

is typically a constant of the order of unity, $R = (q_{11}/q_{12})((s_{11} + s_{12})/(s_{11} + 2s_{12})) + (s_{12}/(s_{11} + 2s_{12}))$, $g_1(\zeta)$ is the dimensionless function controlling the shape of the elastic effects in the middle of the film, which has been obtained analytically in its Fourier form (see Appendix A):

$$\widetilde{g}_1(\eta) = 2 \frac{(\eta/2) \cosh(\eta/2) - \left(1 + \frac{2s_{12}}{s_{11}}\right) \sinh(\eta/2)}{\eta + \sinh(\eta)}. \quad (3.15)$$

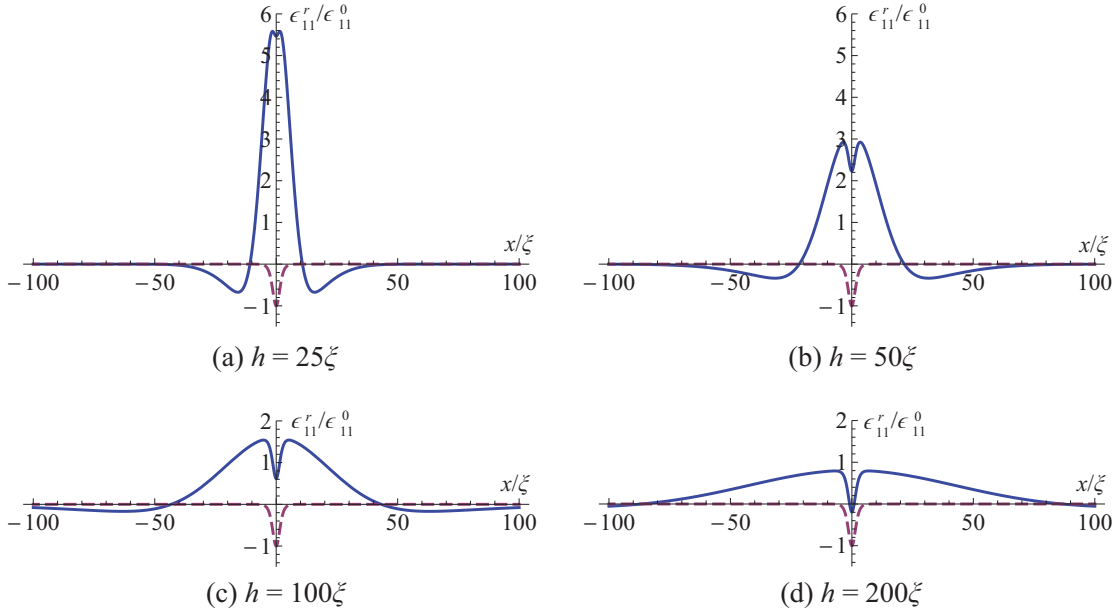


Figure 3.2: Normalized strain component $\epsilon_{11}^r(x, h/2)$ calculated according to Eq. (3.13) as a function of the distance from the wall center x for the middle cross section of a freestanding PbTiO_3 film for different film thicknesses h . Dashed lines represent the x dependence of the same component for a wall in the bulk crystal. ϵ_{11}^0 is the strain in the wall center in the bulk system [Eq. (3.12)]. ξ is the correlation length. (a) $h = 25\xi$, (b) $h = 50\xi$, (c) $h = 100\xi$, and (d) $h = 200\xi$.

Expression (3.13) for ϵ_{11}^r strain component consists of two terms: the first term, with the scale $x \sim 2\xi$, corresponds to the exact solution for a bulk sample (3.11); the second term, with the scale h , represents the surface-related contribution to the elastic profile.

Let us compare the two terms in Eq. (3.13). Since, typically, $h \gg \xi$, the second term is expected to be small by the factor ξ/h . However, in perovskites the factor R is large (e.g., 45 in PbTiO_3), which enhances the surface effect. As a result, for typical film thicknesses ($10\xi < h < 100\xi$), the two terms in Eq. (3.13) are comparable. Such a high strength of the surface effect is related to the high anisotropy of the electrostrictive tensor q_{ij} . The high value of R in perovskites is a consequence of the fact that typically $q_{11} \gg q_{12}$ in these materials (e.g., for PbTiO_3 $q_{11}/q_{12} = 24.8$)

The elastic profiles for the middle cross section of the film ($z = h/2$), as described by Eq. (3.13), for free-standing PbTiO_3 films with different thicknesses are shown and compared with those of the bulk system in Fig. 3.2². One can see an appreciable qualitative difference

²The values used for the ratios $2s_{12}/s_{11} = -0.625$, $q_{11}/q_{12} = 24.8$ correspond to those in PbTiO_3 . The polarization profile is described by the function $f(x) = \tanh x$.

3.2. Numerical description of nonferroelastic domain walls in thin films

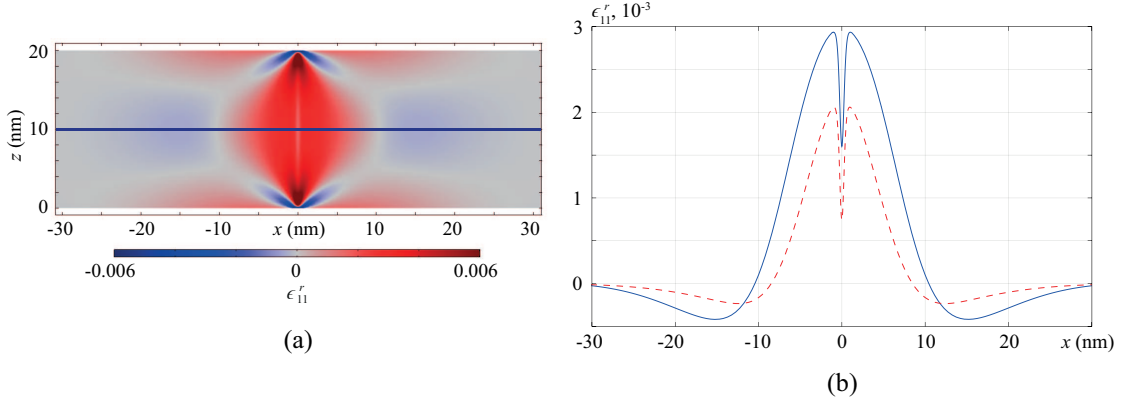


Figure 3.3: In-plane strain $\epsilon_{11}^r(x, z)$ for a 20 nm-thick freestanding PbTiO_3 film. (a) Strain distribution in xz cross section. (b) The strain at the middle cross sections of the film: numerical simulations shown by the solid line, Eq. (3.13) shown as a dashed line.

between the elastic profiles in the film and those in the bulk system. Such a difference holds for a broad range of film thicknesses. Therefore, we can speak here about the effect of "elastic widening" of domain walls in ferroelectric thin films in general.

The physics behind this effect can readily be elucidated drawing analogy with the Saint-Venant principle [36]. Essentially, the domain wall manifests itself as an inclusion of a material with different lattice constants. The mismatch gives rise to elastic fields which, in agreement with the Saint-Venant principle, penetrate inside the domains on distances of the order of the film thickness. The strain distribution has the well-known structure of elastic fields from a linear indentation [38] on a semi-infinite isotropic medium. These elastic fields are sign changing like those from a vertical point load [37]. In the context of the considered problem, an effective linear indentation takes place since the bulk solution does not satisfy stress-free conditions on the surfaces [20].

3.2 Numerical description of nonferroelastic domain walls in thin films

The above considerations capture the main features of the effect. As a support, numerical self-consistent calculations of Eqs. (3.2)–(3.9) were performed taking into account the feedback of the elastic fields on the polarization profile and electrostatic effects. The results of the calculations for 20 nm thick films using parameters for PbTiO_3 ³ are presented in Fig. 3.3(a)

³Parameters used for PbTiO_3 : $s_{11} = 8.0 \times 10^{-12} \text{ Pa}^{-1}$, $s_{12} = -2.5 \times 10^{-12} \text{ Pa}^{-1}$, $s_{44} = 18 \times 10^{-12} \text{ Pa}^{-1}$, $Q_{11} = 0.089 \text{ m}^4/\text{C}^2$, $Q_{12} = -0.026 \text{ m}^4/\text{C}^2$, $\alpha = -3.45 \times 10^8 \text{ Vm}/\text{C}$ (at $T = 300 \text{ K}$), $\beta = -2.9 \times 10^8 \text{ Vm}^5/\text{C}^3$, $\gamma = 1.6 \times 10^9 \text{ Vm}^9/\text{C}^5$, $g_{11} = 2 \times 10^{-10} \text{ Vm}^3/\text{C}$, $g_{44} = 10^{-10} \text{ Vm}^3/\text{C}$, $\kappa_b = 100$.

where the in-plane strain component $\epsilon_{11}^r(x)$ is shown. In agreement with the analytical predictions, the elastic fields around the wall extend to distances of the order of the film thickness. In Fig. 3.3(b) the analytical results are compared with the numerical ones for the middle cross section ($z = h/2$) of the film. One sees that while qualitatively the results obtained with these two methods are in agreement, quantitatively the numerical calculations yield larger values for both the maximal value and the width of the strain profiles, revealing some additional contribution. The source of this contribution is traced back to the feedback of the elastic fields on the polarization profile, which has not been taken into account in the analytical calculations (see Appendix B), while the electrostatic contribution to the same effect is shown to be small.

The obtained results for the freestanding film suggest that, in perovskites, the effect related to the finite film thickness has high enough value to be observable in the TEM measurements.

Numerical calculations were also run for the case of a thin film on a thick substrate. Equations (3.2)–(3.4) with boundary conditions (3.5)–(3.8) were solved self-consistently, with additional boundary conditions at the bottom surface of the substrate:

$$\epsilon_{11}^r(z = -h_S) = 0, \quad u_3(z = -h_S) = 0. \quad (3.16)$$

The elastic properties of the substrate were set identical to those of the film. Calculations were run for different compressive and tensile lattice mismatches between the substrate and the film. Lattice mismatch of magnitudes typical for ferroelectric films was shown to have negligible impact on the relative strain fields near the domain wall⁴.

The results of the simulations for a film of thickness 20 nm on a substrate of thickness 100 nm are presented in Fig. 3.4. One can see that the elastic widening effect manifests itself in the case of a film on a substrate as well, exhibiting strain values comparable to those obtained for the free-standing film, except for the intimate vicinity of the substrate.

3.3 Interwall coupling

The effect of elastic widening of 180° nonferroelastic walls presented above implies an additional mesoscale interaction between them. The force (per unit area) between two domain walls with distance w between them can be obtained from the energy $U(w)$ (per unit length

⁴Note that according to our definition of relative strain and due to mechanical coupling of the film on the substrate, $\epsilon_{11}^r \rightarrow 0$ at $x \rightarrow \pm\infty$ for any mismatch

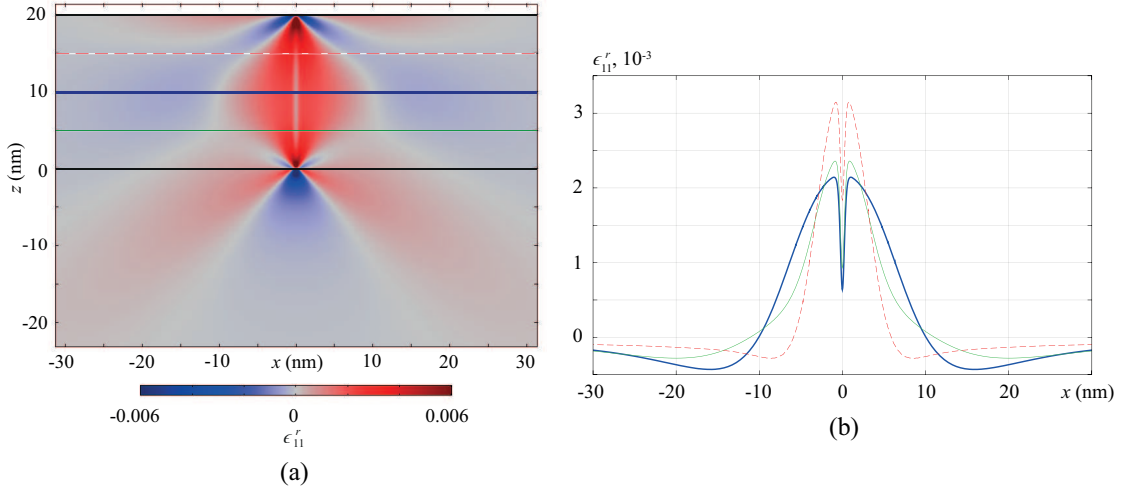


Figure 3.4: In-plane strain $\epsilon_{11}^r(x, z)$ in 20nm-thick PbTiO₃ film on a substrate. The thin film lays at $z \in (0, 20)$ nm. (a) Strain distribution in xz cross section. (b) Cross sections of $\epsilon_{11}^r(x, z)$ at different constant z : in the middle of the film at $z = 10$ nm (thick line), at $z = 5$ nm (thin line) and $z = 15$ nm (dashed line).

in the third dimension) of their elastic interaction:

$$p(w) = \frac{1}{h} dU/dw, \quad (3.17)$$

$$U(w) = \iint c_{ijkl} \epsilon_{ij}^r(x, z) \epsilon_{kl}^r(x-w, z) dx dz, \quad (3.18)$$

where c_{ijkl} is the stiffness tensor, $\epsilon_{ij}^r(x, z)$ is the field created by an individual domain wall located at $x = 0$. Equation (3.18) implies that the elastic field of the ensemble of two domain walls is taken as a sum of those created by individual domain walls. The integration is carried out over all the sample including both film and substrate. Based on the numerical results, this force is evaluated for a PbTiO₃ film of thickness 20 nm. Figure 3.5 shows a plot of the normalized force $E_e(w) = 0.5p(w)/P_S$ of interaction between domain walls obtained using Eqs. (3.17) and (3.18). The parameter E_e has the meaning of the electric field which creates the same force (per unit area) on the walls as that due to the elastic interaction between domain walls. One should mention that Fig. 3.5 does not fully describe interaction between domain walls, since it does not take into account the interaction between the polarization profiles of the domain walls. However, one expects that, for $w \gg \xi$, the force acting between the walls due to the elastic widening effect will be dominating. As seen from Fig. 3.5, this force, being equivalent to electric field of a few kV/cm, can be comparable to the coercive force acting on the wall. This suggests a potentially strong effect of the interwall interaction on polarization switching in thin films. Interestingly, the complicated structure of the elastic fields around

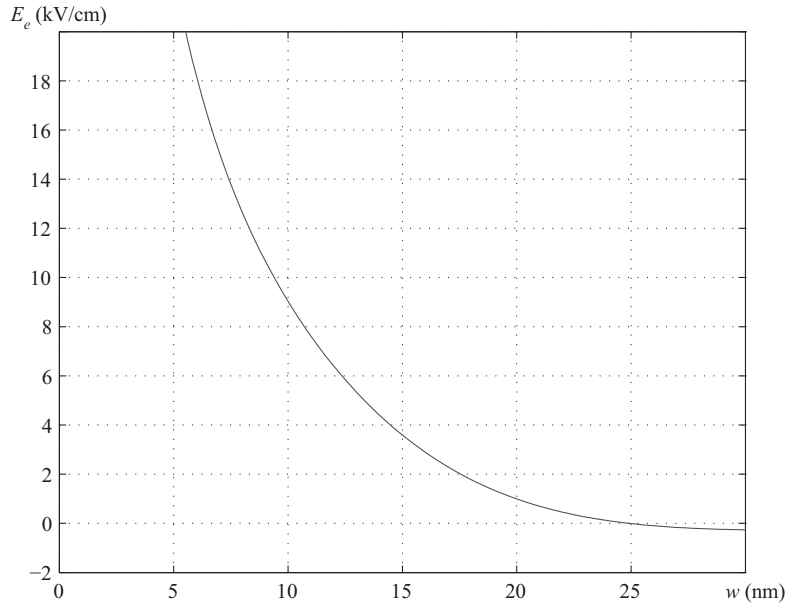


Figure 3.5: The normalized force acting between two 180° domain walls due to the elastic widening effects plotted vs the distance w between them. The units of equivalent out-of-plane electric field E_e which would exert the same pondermotor force on the walls are used (see the text). Calculations are done for a 20 nm PbTiO_3 film using Eqs. (3.17) and (3.18).

domain walls allows a weak attraction between the domain walls on distances between them of the order of the film thickness.

It is important to note that the obtained elastic interaction is dominant in thin films with electroded and short circuited surfaces since the screening of depolarizing fields leads to negligible electrostatic interaction between domain walls (see Appendix C).

3.4 Conclusions

To conclude, it has been demonstrated that in thin ferroelectric films the elastic fields associated with nonferroelastic domain walls extend inside the adjacent domains for a distance comparable to the film thickness. Such elastic widening effect results in appreciable elastic interaction between adjacent walls. It has been shown that the predicted interaction between the walls is appreciable for film thicknesses within the range of tens of nanometres.

This interaction could have substantial impact on polarization switching and domain pattern control in ferroelectric thin films. Particularly, the results are relevant for potential agile electronic devices based on domain walls. The fact that domain walls interact with each other opens new possibilities to control their positions and movement.

Appendix A. Derivation of the strain and stress components near the domain wall in the middle of the thin free-standing film

After the substitution of Eq. (3.10) into Eq. (3.1) one derives from (3.4) the simplified full set of equations for elastically isotropic material:

$$\epsilon_{11} = s_{11}\sigma_{11} + s_{12}\sigma_{22} + s_{12}\sigma_{33} + Q_{12}P_b^2 \quad (3.19)$$

$$\epsilon_{22} = s_{12}\sigma_{11} + s_{11}\sigma_{22} + s_{12}\sigma_{33} + Q_{12}P_b^2 = Q_{12}P_S^2 \quad (3.20)$$

$$\epsilon_{33} = s_{12}\sigma_{11} + s_{12}\sigma_{22} + s_{11}\sigma_{33} + Q_{11}P_b^2 \quad (3.21)$$

$$\epsilon_{13} = (s_{11} - s_{12})\sigma_{13} \quad (3.22)$$

$$\epsilon_{11,33} + \epsilon_{33,11} - 2\epsilon_{13,13} = 0 \quad (3.23)$$

$$\sigma_{11,1} + \sigma_{13,3} = 0, \quad \sigma_{13,1} + \sigma_{33,3} = 0 \quad (3.24)$$

The solution to the problem consisting of Eqs. (3.19–3.24) and boundary conditions (3.7–3.9) is sought in the framework of the plane-stress approach [36, 37]. As it is customarily done (see e.g. [25]), a stress function $\chi(x, z)$ is introduced allowing to represent stress components as:

$$\sigma_{11}(x, z) = \chi_{,33}, \quad \sigma_{13}(x, z) = -\chi_{,13}, \quad \sigma_{33}(x, z) = \chi_{,11} \quad (3.25)$$

As a result, all stress and strain components can be expressed through the stress function $\chi(x, z)$ using Eqs. (3.19–3.22, 3.25). In terms of the stress function, Eq. (3.24) is satisfied and Eq. (3.23) is rewritten in the form:

$$\chi_{,1111} + 2\chi_{,1133} + \chi_{,3333} = \frac{Q_{11}s_{11} - Q_{12}s_{12}}{s_{11}^2 - s_{12}^2} \Delta P^2_{,11} \quad (3.26)$$

Here the notation $\Delta P^2(x) = P_S^2 - P_b^2(x)$ is used.

In terms of Fourier components introduced as

$$\begin{aligned} \tilde{\chi}(k, z) &= \frac{1}{\sqrt{2\pi}} \int_{-\infty}^{\infty} \chi(x, z) \exp(-ikx) dx \\ \Delta \tilde{P}^2(k) &= \frac{1}{\sqrt{2\pi}} \int_{-\infty}^{\infty} \Delta P^2(x) \exp(-ikx) dx \end{aligned} \quad (3.27)$$

Chapter 3. Elastic coupling between nonferroelastic domain walls

Equation (3.26) takes the form:

$$\frac{\partial^4 \tilde{\chi}}{\partial z^4} - 2k^2 \frac{\partial^2 \tilde{\chi}}{\partial z^2} + k^4 \tilde{\chi} = - \frac{Q_{11}s_{11} - Q_{12}s_{12}}{s_{11}^2 - s_{12}^2} k^2 \Delta \tilde{P}^2(k) \quad (3.28)$$

The free surface boundary conditions (3.8–3.9) in terms of $\tilde{\chi}(k, z)$ read:

$$\tilde{\chi}(k, 0) = 0, \quad \tilde{\chi}(k, h) = 0, \quad \frac{\partial}{\partial z} \tilde{\chi}(k, 0) = 0, \quad \frac{\partial}{\partial z} \tilde{\chi}(k, h) = 0 \quad (3.29)$$

The solution to Eq. (3.28) with the boundary conditions (3.29) can be written in the form:

$$\tilde{\chi}(k, z) = - \frac{s_{11}Q_{11} - s_{12}Q_{12}}{s_{11}^2 - s_{12}^2} \frac{\Delta \tilde{P}^2(k)}{k^2} \left(1 + \frac{2 \sinh(\frac{kh}{2}) kz' \sinh(kz')}{kh + \sinh(kh)} - \frac{2(\sinh(\frac{kh}{2}) + \frac{kh}{2} \cosh(\frac{kh}{2})) \cosh(kz')}{kh + \sinh(kh)} \right) \quad (3.30)$$

where $z' = z - h/2$ is the distance from the middle of the film.

From Eq. (3.30), using Eqs. (3.19–3.22, 3.25) the expressions for the in-plane mechanical strain may be readily derived as:

$$\tilde{\epsilon}_{11}^r(k, h/2) = \epsilon_{11}^0 \cdot \left(- \frac{\Delta \tilde{P}^2(k)}{P_s^2} + R \frac{\Delta \tilde{P}^2(k)}{P_s^2} \tilde{g}_1(kh) \right) \quad (3.31)$$

$$\tilde{g}_1(\eta) = 2 \frac{- \left(1 + \frac{2s_{12}}{s_{11}} \right) \sinh(\eta/2) + (\eta/2) \cosh(\eta/2)}{\eta + \sinh(\eta)} \quad (3.32)$$

The case $h \gg \xi$, which is applicable for typical film thicknesses, is of interest. In this case the product $\Delta \tilde{P}^2(k) \tilde{g}_1(kh)$ can be approximated as $\Delta \tilde{P}^2(0) \tilde{g}_1(kh)$ since the characteristic width of $\Delta \tilde{P}^2(k)$ is much larger than that of $\tilde{g}_1(kh)$ as a function of k , i.e., $\frac{1}{\xi} \gg \frac{1}{h}$. Thus one readily makes the inverse fourier transform of (3.31) to get Eq. (3.13):

$$\epsilon_{11}^r(x, h/2) = \epsilon_{11}^0 \cdot \left(- \frac{\Delta P^2(x)}{P_s^2} + \mu R \frac{\xi}{h} g_1\left(\frac{x}{h}\right) \right) \quad (3.33)$$

$$g_1(\zeta) = \frac{1}{\sqrt{2\pi}} \int_{-\infty}^{\infty} \tilde{g}_1(\eta) \exp(i\eta\zeta) d\eta \quad (3.34)$$

Having applied similar logic, from Eq. (3.30) one can derive expressions for other non-zero

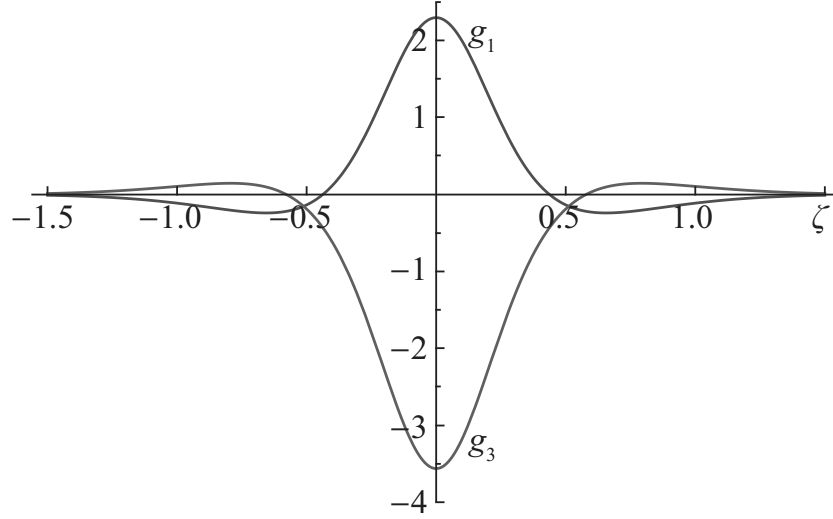


Figure 3.6: Numerical results for the functions $g_1(\zeta)$ and $g_3(\zeta)$ determining the profiles of strain components $\epsilon_{11}^r(x)$ and $\epsilon_{33}^r(x)$ near the domain wall.

strain and stress components:

$$\epsilon_{33}^r(x, h/2) = (s_{11} - s_{12})q_T P_S^2 \cdot \mu R \frac{\xi}{h} g_3\left(\frac{x}{h}\right) \quad (3.35)$$

$$\sigma_{11}(x, h/2) = q_T P_S^2 \cdot \mu R \frac{\xi}{h} f_1\left(\frac{x}{h}\right) \quad (3.36)$$

$$\sigma_{22}(x, h/2) = q_T P_S^2 \cdot \left(\frac{\Delta P^2(x)}{P_S^2} + \mu R \frac{\xi}{h} f_2\left(\frac{x}{h}\right) \right) \quad (3.37)$$

$$\sigma_{33}(x, h/2) = q_T P_S^2 \cdot \left(R \frac{\Delta P^2(x)}{P_S^2} + \mu R \frac{\xi}{h} f_3\left(\frac{x}{h}\right) \right) \quad (3.38)$$

where $q_T = -\frac{s_{11}Q_{12} - s_{12}Q_{11}}{s_{11}^2 - s_{12}^2}$. Functions $g_3(\zeta)$, $f_i(\zeta)$ are the inverse Fourier transforms of $\tilde{g}_3(\eta)$, $\tilde{f}_i(\eta)$ defined identically to Eq. (3.34). The analytical expressions for $\tilde{g}_3(\eta)$, $\tilde{f}_i(\eta)$ read:

$$\tilde{g}_3(\eta) = 2 \frac{-\left(1 + \frac{2s_{12}}{s_{11}}\right) \sinh(\eta/2) - (\eta/2) \cosh(\eta/2)}{\eta + \sinh(\eta)} \quad (3.39)$$

$$\tilde{f}_1(\eta) = 2 \frac{-\sinh(\eta/2) + \frac{\eta}{2} \cosh(\eta/2)}{\eta + \sinh(\eta)} \quad (3.40)$$

$$\tilde{f}_2(\eta) = 2 \frac{\frac{2s_{12}}{s_{11}} \sinh(\eta/2)}{\eta + \sinh(\eta)} \quad (3.41)$$

$$\tilde{f}_3(\eta) = 2 \frac{-\sinh(\eta/2) - \frac{\eta}{2} \cosh(\eta/2)}{\eta + \sinh(\eta)} \quad (3.42)$$

The profiles of $g_1(\zeta)$, $g_3(\zeta)$ obtained after taking the inverse Fourier transforms numerically are shown in Fig. 3.6 (the value of s_{12}/s_{11} has been set -0.3125 as for PbTiO_3).

Appendix B. Coupling between polarization and strain

The main source of surface-induced perturbation of polarization profile is electrostrictive coupling between polarization and elastic strain and stress tensors. For sake of simplicity, the back action of elastic variables on polarization is investigated for the case of the second order phase transition, with Gibbs potential written up to the 4th power of the order parameter – the same considerations can be applied to the first order phase transition with qualitatively the same results.

The following Gibbs potential is considered:

$$G = \frac{1}{2}\alpha P_z^2 + \frac{1}{4}\beta P_z^4 - \frac{1}{2}s_{11}(\sigma_{11}^2 + \sigma_{22}^2 + \sigma_{33}^2) - s_{12}(\sigma_{11}\sigma_{22} + \sigma_{22}\sigma_{33} + \sigma_{33}\sigma_{11}) - \frac{1}{4}s_{44}\sigma_{13}^2 - Q_{12}(\sigma_{11} + \sigma_{22})P_z^2 - Q_{11}\sigma_{33}P_z^2 + \frac{1}{2}g_{44}\left(\frac{\partial P_z}{\partial x}\right)^2 + \frac{1}{2}g_{11}\left(\frac{\partial P_z}{\partial z}\right)^2, \quad (3.43)$$

After the substitution of Eqs. (3.36-3.38) into Eq. (3.2) for this Gibbs potential, Eq. (3.2) rewrites in the following form in the center of the film (in order to demonstrate the general trend of the back action of elastic fields on polarization, dependence of the polarization on z -coordinate and effect of the depolarizing fields are neglected):

$$-\left(1 + 2\frac{\xi}{h}g\left(\frac{x}{h}\right)\right)P_S^2P_z(x) + P_z^3(x) = 2P_S^2\xi^2\frac{\partial^2 P_z}{\partial x^2}(x), \quad (3.44)$$

where

$$P_S = \sqrt{-\frac{\alpha}{\beta}}, \quad (3.45)$$

$$\xi = \sqrt{\frac{g_{44}}{2P_S^2(2q_T R Q_{11} + 2q_T Q_{12} + \beta)}}, \quad (3.46)$$

$$g(\zeta) = \frac{\mu R q_T}{2R q_T Q_{11} + 2q_T Q_{12} + \beta} (Q_{12}f_1(\zeta) + Q_{12}f_2(\zeta) + Q_{11}f_3(\zeta)). \quad (3.47)$$

For example, in PbTiO_3 $g(\zeta) \approx -0.3f_1(\zeta) - 0.3f_2(\zeta) + 1.2f_3(\zeta)$. One can see that if the back effect of elastic fields on polarization is not accounted for, i.e., if $g(x/h) = 0$, then the solution to Eq. (3.44) attains the polarization profile in the bulk $P_b(x)$ (for the considered case of second-order phase transition, the solution is classic hyperbolic tangent profile described by Eq. (2.23),

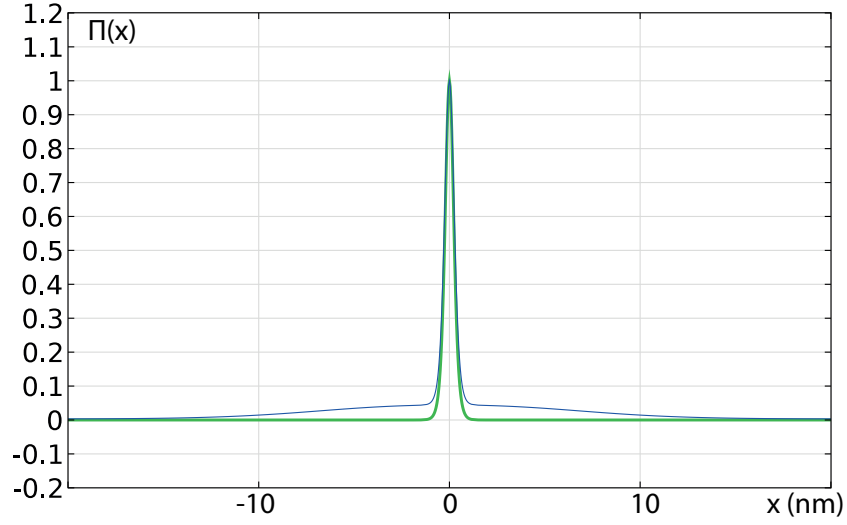


Figure 3.7: Function $\Pi(x) = 1 - P^2(x)/P_S^2$ for the bulk polarization profile (green, thick) and the corrected profile (blue, thin)

with $t_W = 4\xi$).

Equation (3.44) was solved in approximation $\xi \ll h$; the following polarization profile was obtained:

$$P_z(x) \approx P_S \left(1 + \frac{\xi}{h} g\left(\frac{x}{h}\right) \right) \tanh\left(\frac{x}{2\xi(1 - \frac{\xi}{h}g(0))} \right). \quad (3.48)$$

One can elucidate that this profile satisfies Eq. (3.44) by substituting it into (3.44) and making the following approximations at the two characteristic scales of the x -coordinate:

- when $x \sim \xi$, one can set $g(x/h) \approx g(0)$.
- when $x \sim h$, one can set $P(x) \approx P_S$, and keep only terms of the first order of smallness ($\propto (\xi/h)$) in Eq. (3.44).

Thus, the function $g(\zeta)$ describes the back effect of elastic stresses on the polarization. One can see that the correction to the polarization profile has smallness (ξ/h) , and the profile of polarization in the thin film is very close to the profile in the bulk – see Fig. 3.7 where function $\Pi(x) = 1 - P^2(x)/P_S^2$ is plotted for these two cases. However, despite this smallness of correction to the polarization profile, its back influence on the elastic effects is not negligible. The trends leading to this behaviour can be demonstrated as follows.

After the back influence on the polarization profile is obtained (Eq. (3.48)), one should

Chapter 3. Elastic coupling between nonferroelastic domain walls

recalculate expressions for the elastic variables (3.33), (3.35)–(3.38) that are generated when the new profile of polarization is taken into account. This task would be of increased difficulty: in this chapter, the developed analytical theory for elastic profiles only describes the case of polarization distribution for which the function $\Pi(x)$ has width $\xi \ll h$. As one can see in Fig. 3.7, the function $\Pi(x)$ for the polarization profile (3.48) has now the width of the order of the film thickness h , thus the developed theory cannot be applied directly.

Nevertheless, one can still make a conclusion that the recalculated elastic profiles will have a larger magnitude. Note that the magnitude of the elastic stresses (3.36)–(3.38) is proportional to the constant μ introduced in Eq. (3.14):

$$\mu = \frac{1}{\sqrt{2\pi\xi}} \int_{-\infty}^{\infty} \left(1 - \frac{P_b^2(x)}{P_S^2} \right) dx. \quad (3.49)$$

As a rather rough estimation, one can say that the recalculated elastic stresses will have the same form as given by Eqs. (3.36)–(3.38), with the coefficient of proportionality $\mu = \frac{1}{\sqrt{2\pi\xi}} \int_{-\infty}^{\infty} \Pi(x) dx$ renormalized with accordance to the new function $\Pi(x)$. In a way, the coefficient μ has a meaning of the surface area under the graph $\Pi(x)$ in Fig. 3.7. The new function $\Pi(x)$ has a larger surface area under the graph, therefore the value for constant μ is larger, and the magnitude of the elastic stresses (3.36)–(3.38) is stronger. The qualitative results of this reasoning are confirmed by numerical simulations of the system (see Section 3.2).

Appendix C. Electrostatic interaction of domain walls

The deviation of polarization profile in the film from the bulk polarization profile, described in the previous section and having a smallness of ξ/h , results in presence of electric fields and in electrostatic interaction between domain walls. One can expect that the smallness of the deviation translates into weakness of the electrostatic interaction. Here, this reasoning is illustrated.

The procedures are followed similar to those described in the main text (Eqs. (3.17) and (3.18)). If a separate domain wall located at $x = 0$ creates electric field $\mathbf{E}(x, z)$, then the electric field of the ensemble of the two domain walls located at $x = -w/2$ and at $x = w/2$ can be estimated as $\mathbf{E}_{\text{ens}}(x, z) = \mathbf{E}(x + w/2, z) + \mathbf{E}(x - w/2, z)$. Then, the expression for electrostatic energy density $\kappa_b \epsilon_0 \|\mathbf{E}_{\text{ens}}\|^2/2$ is used to calculate the force (per unit area) between two domain

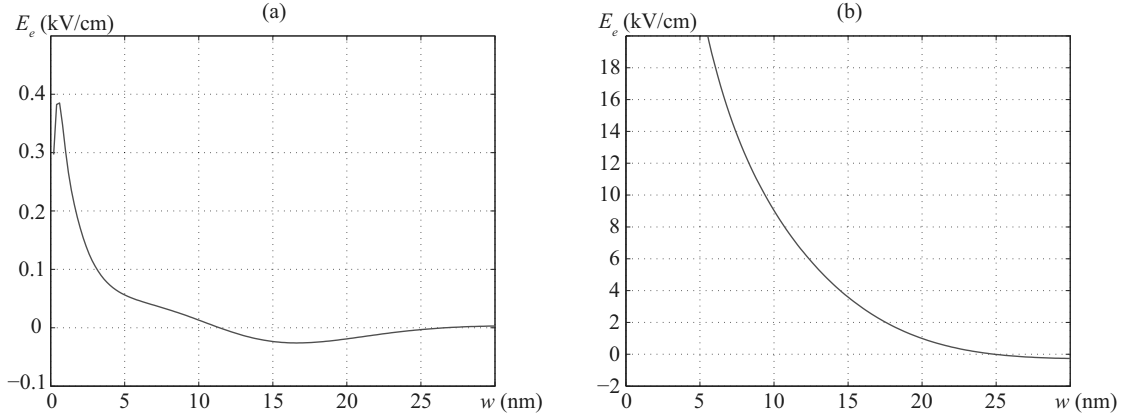


Figure 3.8: Normalized force of interaction between domain walls. (a) Conditioned by electrostatic effects only. (b) Conditioned by elastic effects. The value of the dielectric constant used is $\kappa_b = 100$, the film thickness $h = 20$ nm, the substrate thickness $h_s = 100$ nm

walls with distance w between them:

$$p(w) = \frac{1}{h} dU/dw \quad (3.50)$$

$$U(w) = \iint \kappa_b \epsilon_0 (\mathbf{E}(x + w/2, z) \mathbf{E}(x - w/2, z)) dx dz \quad (3.51)$$

Using Eqs. (3.50) and (3.51) the force of the electrostatic interaction is calculated and compared to the elastic one, described by Eqs. (3.17) and (3.18). In Fig. 3.8 the comparison is shown of electrostatic and elastic forces obtained solving numerically Eqs. (3.2)–(3.4) of the main text with boundary conditions (3.5)–(3.8), (3.16) for a film of thickness 20 nm on a substrate of thickness 100 nm – it is clear that the electrostatic interaction is few orders of magnitude weaker.

4 Mechanically incompatible ferroelastic domain walls in thin films

Ferroelectric domain walls (DWs) have been one of the priority subjects of investigations in the field of ferroelectricity due to their unique properties that may be used in ferroelectric devices. In most cases DWs form in accordance to the principles of their electric neutrality [20] and of the mechanical compatibility of the domains they separate [23]. There have been a growing attention to exceptional cases, where domain structures contain DWs oriented with violation to these requirements. For instance, controllable generation of structures with charged DWs, forcing a wall to form in spite of nonfulfillment of the 'electric' condition on its orientation, is seen as the principal mechanism for attaining the DW conductivity, implying a number of potential applications in nanoelectronics with reconfigurable electric circuits.

The violation of the condition of the mechanical compatibility of the domains separated by a wall is typically considered unlikely due to the large elastic energy penalties associated with it. Initially, this condition was formulated for individual walls in bulk crystals, where a small deviation of an individual DW off its permissible orientation would result in generation of uncompensated elastic stresses propagating on macroscopic volumes, resulting in infinite elastic energy penalties per deviated wall. This condition is widely used in thin films as well despite the fact that, strictly speaking, the considerations formulated for the bulk crystals do not apply to the thin films. Specifically, the elastic stresses generated by an individual mechanically incompatible DW propagate only on finite distances from the wall in thin films, as a consequence the elastic energy penalty associated with the wall deviation may be small enough to have a limited impact on the DW orientation, with possibility for other mechanisms to come to play to govern the DW orientation. For instance, numerical phase-field modelling of BiFeO₃-like thin films documented a small change of the ferroelastic DW orientation with variation of the DW self-energy per unit area [39]. Besides, in films strained on a substrate,

Chapter 4. Mechanically incompatible ferroelastic domain walls in thin films

generation of DW incompatibility stresses by a deviated DW does not automatically lead to increase of the elastic energy of the structure since the interaction of the DW incompatibility stresses with film-substrate mismatch strains decreasing energy of the structure is possible. In PbZrTiO_3 films, a small deviation of a wall pair of a thin domain was reported which was linked to relaxation of the film-substrate lattice mismatches by the DW mechanical incompatibility elastic fields generated as a result of the deviation [40].

A question arises whether deviations of an individual DW off the mechanically compatible state can be large in thin films. One should note that in many systems a deviation off the mechanically compatible state is closely tied with breaking of the electric neutrality of the wall. In order to investigate applicability of the 'elastic' condition solely on the DW orientation in thin films, it is reasonable to focus on those systems where a deviation of the wall preserves the DW electric neutrality. For the analysis, a system of high experimental interest is chosen, a BiFeO_3 -like rhombohedral (010)-oriented thin film on a cubic substrate with 71° ferroelastic domain structure. Based on the analysis of this system, two mechanisms of possible DW deviations in thin ferroelectric films are formulated. Firstly, a DW deviation towards minimizing the wall self-energy is expected in systems where the elastic energy penalty resulting from the deviation is small compared to the reduction of the wall self-energy. Besides, in films strained on a substrate, large DW deviations can be driven by relaxation of the film-substrate mismatch elastic stresses by the DW incompatibility elastic fields.

In the following, the applicability of the condition of mechanical compatibility of the DW to thin films is trialled by describing the variation of the energy of domain structures upon deviation of the 71° walls in rhombohedral BiFeO_3 -like thin film off their permissible orientation. A (010)-oriented film on a cubic substrate is considered with the domain structure comprised of domain states $(1\bar{1}1)$, hereafter domain I, and $(1\bar{1}\bar{1})$, hereafter domain II, alternating in [100]-direction. Following the requirements of the electrical neutrality of the wall and of the mechanical compatibility of the domains separated by the wall, the DWs in the structure have $(\bar{1}10)$ orientation, inclining at the angle of 45° to the film surface [41, 42]. Deviations that conserve the electric neutrality of the wall are restricted by the condition $\mathbf{P}_S^I \cdot \mathbf{n} = \mathbf{P}_S^{II} \cdot \mathbf{n}$, where \mathbf{n} is the normal to the wall, \mathbf{P}_S^I and \mathbf{P}_S^{II} are the spontaneous polarizations of domain states I and II, respectively. Following this restriction, all deviations that keep the DW normal \mathbf{n} in the xy -plane do not break the requirement of the DW electric neutrality, only violating the condition of the DW mechanical compatibility (Cartesian reference frame with axes Ox , Oy , and Oz directed along [100], [010], and [001] directions, respectively, is introduced). Other deviations, leading to charged DWs, are excluded from the following consideration.

In the framework of the analysis, the part of the energy of the structure with neutral DWs that affects the wall orientation is comprised of two contributions: the elastic energy associated with the generation of stresses by the mechanically incompatible wall, and the DW self-energy. The energy of the structure is calculated for an arbitrary shape of a single isolated domain wall, which is a reasonable approximation for systems where the distance between DWs largely exceeds the film thickness, i.e., for equilibrium sparse domain patterns and for non-equilibrium structures with an isolated wall. In such systems, since the elastic fields generated by incompatible DWs propagate away from the wall only on distances of the order of the film thickness (according to the principles of elasticity), the interference of the fields from the neighbouring DWs can be neglected. Besides, the description is given to DWs in equilibrium non-sparse domain patterns, considering planar walls of an arbitrary inclination. In all cases, for the calculation of the energy of the structure, the DW self-energy is taken isotropic, dependent only on the DW surface area and independent of the wall inclination. The equilibrium wall shape in sparse structures and the equilibrium wall inclination in non-sparse structures are obtained imposing the requirement of the minimal energy of the structure.

4.1 Isolated elastic domain walls in thin films

First, the shape of an individual domain wall in thin films is described. The geometry of the problem allows two-dimensional treatment with all variables depending on x and y only, the schematics of the problem is shown in Fig. 4.1. The DW shape is defined by an arbitrary function of deviation $D(y)$, which describes the deviation of the DW off the mechanically compatible state (restriction $D(0) = 0$ is imposed on the function). The shape of the wall is thus described by the set coordinates $(y + D(y), y)$, $0 \leq y \leq h$, where h is the thickness of the film (see Fig. 4.1). At all points where the local angle of the DW inclination differs from 45° ($dD/dy \neq 0$), inter-domain lattice mismatch is observed, generating elastic stresses in its surroundings. For description of elastic stresses of the system, the method of fictitious dislocations is implemented (see, e.g., [13, 14]), in framework of which the stresses in the system $\sigma_{ij}(x, y)$ can be found as the elastic fields generated by fictitious dislocations equivalently representing the lattice mismatches in the system:

$$\sigma_{ij}(x, y) = \iint \sigma_{ij}^{kl}(x, y; x_0, y_0) \alpha_{kl}(x_0, y_0) dx_0 dy_0, \quad (4.1)$$

where $\sigma_{ij}^{kl}(x, y; x_0, y_0)$ is the elastic stress field generated by a unit dislocation located at (x_0, y_0) , having Burgers vector directed along r_l and dislocation line along r_k direction, α_{kl} is the

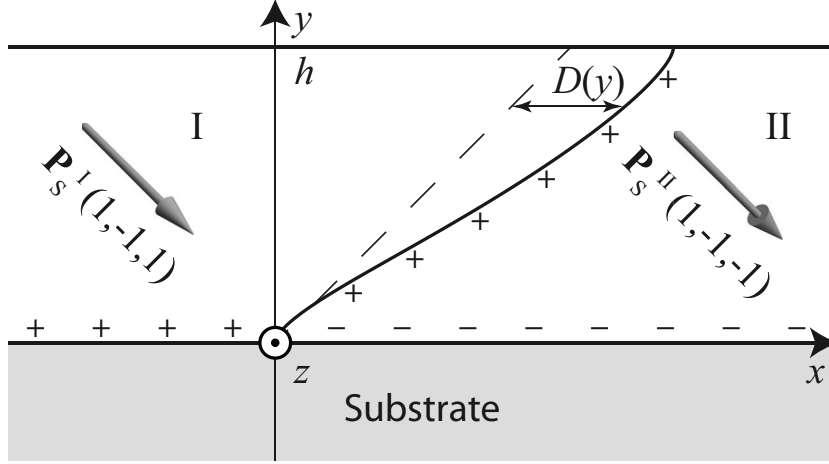


Figure 4.1: Schematics of the BiFeO₃ used for calculations in sparse domain structures. Symbols '+' represent screw dislocations having positive Burgers vector density db^{DW}/dy and db^{sub}/dx , symbols '-' represent dislocations with negative Burgers vector density – see the text. Dashed line shows the mechanically compatible orientation of the DW.

dislocations density tensor defined as [43]:

$$\alpha_{kl} = -e_{ijk} \frac{\partial \beta_{S_{jl}}}{\partial r_i}, \quad (4.2)$$

e_{ijk} is the Levi-Civita permutation symbol, $\beta_{S_{jl}} = \partial u_l / \partial r_j$ is the unsymmetrized misfit strain tensor describing spontaneous deformations of the lattices of the domains with respect to the substrate lattice, and u_l is the spontaneous displacement with respect to the unstrained substrate.

In the considered domain structure, domains I and II are characterized by the following unsymmetrized misfit strain tensors $\beta_{S_{ij}}^{(I)}$ and $\beta_{S_{ij}}^{(II)}$, respectively:

$$\beta_{S_{ij}}^{(I)} = \begin{pmatrix} \epsilon_s & 0 & \beta \\ -\beta & \epsilon_s & -\beta \\ 0 & 0 & \epsilon_s \end{pmatrix}, \quad \beta_{S_{ij}}^{(II)} = \begin{pmatrix} \epsilon_s & 0 & -\beta \\ -\beta & \epsilon_s & \beta \\ 0 & 0 & \epsilon_s \end{pmatrix}, \quad (4.3)$$

where $\epsilon_s = (a_f - a_s)/a_s$ is the film-substrate lattice constant mismatch, a_f and a_s are the lattice constants of the film and of the substrate, respectively, $\beta = \pi/2 - \alpha_{th}$ is the film-substrate angular mismatch, α_{th} is the angle between $\langle 100 \rangle$ directions of the perovskite unit cell of the film.

Using Eqs. (4.2) and (4.3), the system of fictitious dislocations that equivalently describes elastic fields generated by inter-domain and film-substrate lattice mismatches was obtained.

The system of dislocations is comprised of the sets of edge and screw dislocations at the film-substrate interface (following [42]) and of the set of screw dislocations on the wall. The edge dislocations in the system describe the mismatch between the lattice constants of the film and of the substrate. It was shown (see Appendix A) that the mismatch between the film and substrate lattice constants does not have any effect on the DW orientation, therefore edge dislocations are excluded from the consideration.

Hereafter, only elastic fields generated by screw dislocations in the system are described. All screw dislocations in the system have their lines directed along z . The set of the screw dislocations situated on the film-substrate interface describes the lattice mismatch between the rhombohedral film and the cubic substrate [42]. The second set of the screw dislocations, situated on the domain wall, describes the mismatch between domain I and II that appears because of different orientations of domains I and II unit cell rhombohedra.

Using Eqs. (4.2) and (4.3), expression for stress in the structure (4.1) is rewritten in the following form:

$$\sigma_{ij}(x, y) = \sigma_{ij}^{\text{sub}}(x, y) + \sigma_{ij}^{\text{DW}}(x, y), \quad (4.4)$$

$$\sigma_{ij}^{\text{sub}}(x, y) = \int_{-\infty}^{\infty} \sigma_{ij}^{33}(x, y; x_0, 0) \frac{db^{\text{sub}}}{dx}(x_0) dx_0, \quad (4.5)$$

$$\sigma_{ij}^{\text{DW}}(x, y) = \int_0^h \sigma_{ij}^{33}(x, y; y_0 + D(y_0), y_0) \frac{db^{\text{DW}}}{dy}(y_0) dy_0, \quad (4.6)$$

$$\frac{db^{\text{sub}}}{dx}(x) = -\beta \text{sign } x, \quad (4.7)$$

$$\frac{db^{\text{DW}}}{dy}(y) = 2\beta \cdot \frac{dD}{dy} = 2\beta \cdot (\cot \phi(y) - 1). \quad (4.8)$$

Here, $\sigma_{ij}^{\text{sub}}(x, y)$ and $\sigma_{ij}^{\text{DW}}(x, y)$ are the elastic stresses generated by the sets of the screw dislocations situated at the film-substrate interface and at the domain wall, respectively, db^{sub}/dx and db^{DW}/dy are 'Burgers vector densities' of dislocations located at the film-substrate interface and at the domain wall, respectively, and $\phi(y)$ is the local angle of the DW inclination. In the geometry of the problem (Fig. 4.1), non-zero components of the elastic field $\sigma_{ij}^{33}(x, y; x_0, y_0)$ generated at point (x, y) by a unit screw dislocation having line along z , located at coordinates (x_0, y_0) in an elastically isotropic medium with the free surface at $y = h$ are described by the following expressions (henceforth, the film and the substrate are considered elastically

isotropic with identical shear moduli G):

$$\sigma_{13}^{33}(x, y; x_0, y_0) = -\frac{G}{2\pi} \left(\frac{y - y_0}{(x - x_0)^2 + (y - y_0)^2} + \frac{2h - y - y_0}{(x - x_0)^2 + (2h - y - y_0)^2} \right), \quad (4.9)$$

$$\sigma_{23}^{33}(x, y; x_0, y_0) = \frac{G}{2\pi} \left(\frac{x - x_0}{(x - x_0)^2 + (y - y_0)^2} - \frac{x - x_0}{(x - x_0)^2 + (2h - y - y_0)^2} \right), \quad (4.10)$$

The first terms of r.h.s. of Eqs. (4.9) and (4.10) correspond to the stresses of a screw dislocation located at (x_0, y_0) in the infinite isotropic medium [44]. The second terms of r.h.s. are added in order to fulfil the requirement of zero σ_{23} stress component at the mechanically free surface ($y = h$), which corresponds to the elastic stresses generated by a 'mirror dislocation' with Burgers vector of the opposite sign, in close analogy with the 'mirror charges' method in electrostatics (as discussed in [45]).

The energy of the domain structure is composed of the elastic energy of the stresses $\sigma_{ij}(x, y)$ and of the DW self-energy. It is known that the energy of elastic fields generated by dislocations can be equivalently represented as the energy of interaction between dislocation lines (see, e.g., [13]). This follows along similar lines with electrostatics, where the energy of electric fields is equivalent to the energy of interaction between charged particles. In the following, we will discuss the elastic energy of the system from the point of view of interaction between the dislocations in the structure. The second part of the contribution to the energy of the system, DW self-energy, is taken dependent only in the DW surface area, and independent of the DW inclination.

For any shape of the DW defined by the deviation function $D(y)$, the total energy of the system U (per unit length in z -direction) is calculated using the following expressions:

$$U = U_{\text{el}}^{\text{sub}} + U_{\text{el}}^{\text{DW}} + U_{\text{el}}^{\text{int}} + U_{\text{self}}, \quad (4.11)$$

$$U_{\text{el}}^{\text{sub}} = \frac{1}{2} \int_{-\infty}^{\infty} \int_{-\infty}^{\infty} E \left(x_1, 0, \frac{db^{\text{sub}}}{dx}(x_1); x_2, 0, \frac{db^{\text{sub}}}{dx}(x_2) \right) dx_1 dx_2, \quad (4.12)$$

$$U_{\text{el}}^{\text{DW}} = \frac{1}{2} \int_0^h \int_0^h E \left(y_1 + D(y_1), y_1, \frac{db^{\text{DW}}}{dy}(y_1); y_2 + D(y_2), y_2, \frac{db^{\text{DW}}}{dy}(y_2) \right) dy_1 dy_2, \quad (4.13)$$

$$U_{\text{el}}^{\text{int}} = \int_0^h \int_{-\infty}^{\infty} E \left(x_1, 0, \frac{db^{\text{sub}}}{dx}(x_1); y_2 + D(y_2), y_2, \frac{db^{\text{DW}}}{dy}(y_2) \right) dx_1 dy_2, \quad (4.14)$$

$$U_{\text{self}} = \lambda \int_0^h \sqrt{1 + (1 + D'(y))^2} dy, \quad (4.15)$$

4.1. Isolated elastic domain walls in thin films

where h is the film thickness, λ is the DW self-energy per unit area, $U_{\text{el}}^{\text{sub}}$ is the film-substrate misfit elastic energy, $U_{\text{el}}^{\text{DW}}$ is the DW mechanical incompatibility energy penalty, $U_{\text{el}}^{\text{int}}$ is the energy of interference of the elastic fields generated by film-substrate and inter-domain lattice mismatches, U_{self} is the DW self-energy which is taken proportional to the length of the wall, $E(x_1, y_1, b_1; x_2, y_2, b_2)$ is the energy of interaction between two screw dislocations located at points (x_1, y_1) and (x_2, y_2) , having Burgers vectors $(0, 0, b_1)$ and $(0, 0, b_2)$, respectively. The expression for the energy of interaction between dislocation was obtained as (see Appendix a)

$$E(x_1, y_1, b_1; x_2, y_2, b_2) = \frac{b_1 b_2 G}{4\pi} \ln \left(\frac{(x_1 - x_2)^2 + (2h - y_1 - y_2)^2}{(x_1 - x_2)^2 + (y_1 - y_2)^2} \right). \quad (4.16)$$

Analysing Eqs. (4.11)–(4.15), it is possible to draw preliminary conclusions about changes of the energy U with the DW deviation. For instance, a deviation of the DW in clockwise direction, given by positive dD/dy , results in appearance at the DW of screw dislocations with positive Burgers vector density db^{DW}/dy . Similarly to electrostatics, generation of such dislocations is preferable in presence of film-substrate dislocations having negative Burgers vector density db^{sub}/dx , and unfavourable in presence of ones with positive Burgers vector density (can be seen from Eqs. (4.14) and (4.16)). In the geometry of the problem (see Fig. 4.1) the interaction of such 'positive' DW dislocations is stronger with 'negative' film-substrate dislocations than with 'positive', which follows in negative energy of interaction $U_{\text{el}}^{\text{int}}$. At the same time, a clockwise rotation of the DW is characterized by positive elastic energy of the generated DW incompatibility elastic distortions $U_{\text{el}}^{\text{DW}}$ (i.e., positive energy of interaction between the DW dislocations of the same sign) and by increase of the DW self-energy U_{self} proportional to the DW length. Competition between decreasing $U_{\text{el}}^{\text{int}}$ and increasing $U_{\text{el}}^{\text{DW}} + U_{\text{self}}$, which is the subject to analysis in the following part, defines whether the deviation of the DW in clockwise direction is overall favourable. Along similar lines, in case of a deviation in counter-clockwise direction, given by negative dD/dy , elastic energies $U_{\text{el}}^{\text{int}}$ and $U_{\text{el}}^{\text{DW}}$ increase, and the DW self-energy U_{self} decreases due to shortening of the DW.

The shape of the DW corresponding to the minimal energy of the system is sought using the method of variations to the expression for the energy of the system U [Eq. (4.11)]. The criterion for the DW shape was formulated in the form of nonlinear Fredholm integral equation:

$$\int_0^1 K(\tilde{y}_1, \tilde{y}_2) \tilde{D}'(\tilde{y}_1) d\tilde{y}_1 + f(\tilde{y}_2) = 0. \quad (4.17)$$

Here dimensionless coordinates $\tilde{x}_i = x_i/h$, $\tilde{y}_i = y_i/h$ and dimensionless function of deviation

Chapter 4. Mechanically incompatible ferroelastic domain walls in thin films

$\tilde{D}(\tilde{y}) = D(h\tilde{y})/h$ were used. Kernel $K(\tilde{y}_1, \tilde{y}_2)$ and function $f(\tilde{y}_2)$ are defined as follows (see Appendix B for derivation):

$$K(\tilde{y}_1, \tilde{y}_2) = 2e(\tilde{y}_1 + \tilde{D}(\tilde{y}_1), \tilde{y}_1; \tilde{y}_2 + \tilde{D}(\tilde{y}_2), \tilde{y}_2) + 2 \int_{\tilde{y}_2}^1 \frac{\partial e}{\partial \tilde{x}_2}(\tilde{y}_1 + \tilde{D}(\tilde{y}_1), \tilde{y}_1; t + \tilde{D}(t), t) \tilde{D}'(t) dt, \quad (4.18)$$

$$f(\tilde{y}_2) = e_s(\tilde{y}_2 + \tilde{D}(\tilde{y}_2), \tilde{y}_2) + \int_{\tilde{y}_2}^1 \frac{\partial e_s}{\partial \tilde{x}_2}(t + \tilde{D}(t), t) \tilde{D}'(t) dt + \frac{2\pi\lambda}{G\beta^2 h} \frac{1 + \tilde{D}'(\tilde{y}_2)}{\sqrt{1 + (1 + \tilde{D}'(\tilde{y}_2))^2}}, \quad (4.19)$$

$$e(\tilde{x}_1, \tilde{y}_1; \tilde{x}_2, \tilde{y}_2) = \ln \left(\frac{(\tilde{x}_1 - \tilde{x}_2)^2 + (2 - \tilde{y}_1 - \tilde{y}_2)^2}{(\tilde{x}_1 - \tilde{x}_2)^2 + (\tilde{y}_1 - \tilde{y}_2)^2} \right), \quad (4.20)$$

$$e_s(\tilde{x}_2, \tilde{y}_2) = - \int_{-\infty}^{\infty} \text{sign}(\tilde{x}_1) e(\tilde{x}_1, 0; \tilde{x}_2, \tilde{y}_2) d\tilde{x}_1. \quad (4.21)$$

Equation (4.17) was solved numerically for varying film thicknesses, the method of conjugated gradients was implemented. Following parameters for BiFeO₃ were used: $G = 56$ GPa, $\beta = 0.0113$, $\lambda = 0.092$ J/m². Domain wall shapes corresponding to the minimal energies of sparse domain structures in films of different thicknesses are shown in Fig. 4.2, the variation of the DW shape with the film thickness change is observed. The average angle between the DW and the film surface increases with the film thickness decrease, breaking the condition of mechanical compatibility of the DW in ultrathin BiFeO₃ films. The variation of the DW shape with the film thickness results from different thickness dependencies of the two contributions to the energy of the structure.

It can be readily obtained from Eqs. (4.12)–(4.15) that the elastic part of the total energy of the system scales with the film thickness as h^2 , while the DW self-energy scales as h . As a result, with decreasing the film thickness, the DW self-energy makes an increasingly more prominent contribution to the total energy of the structure compared to the elastic one, the DW tending to orient closer to the orientation of the minimal length despite the increase of the elastic energy. In the limiting case of the film thickness tending to zero, the DW orients normally to the film surface, which corresponds to the the minimal DW self-energy U_{self} (shown in Fig. 4.2 by the thick line).

In turn, increasing the thickness of the film h makes the contribution of the elastic energy $U_{\text{el}}^{\text{int}} + U_{\text{el}}^{\text{DW}}$ more important compared to the DW self-energy. In the limiting case of the thickness tending to infinity, the orientation of the wall is determined by the requirement of the minimal elastic energy of the structure, which is, interestingly, differs from the orientation

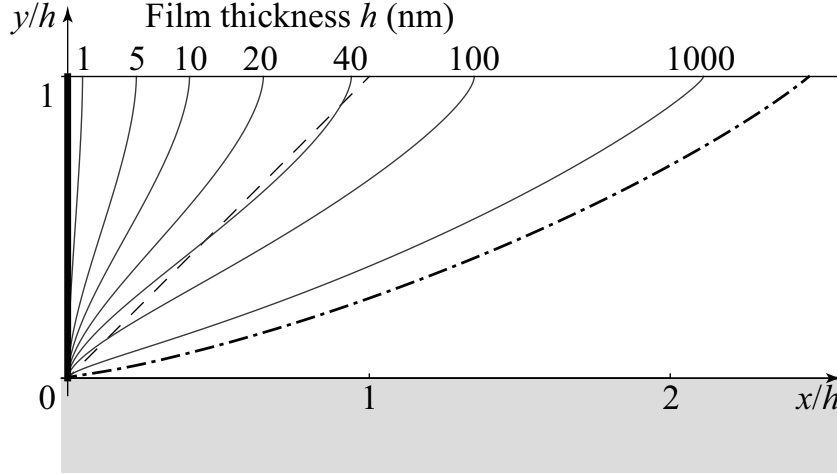


Figure 4.2: Shapes of the bent 71° domain walls at different thicknesses of the BiFeO_3 film (thin solid lines), compared to the mechanically compatible DW inclination (dashed line). The thick line shows the DW shape in the limiting case of film thickness tending to zero, determined by the condition of the minimal DW self-energy. Dash-dot line shows the DW shape in the limiting case of film thickness tending to infinity, determined by the condition of the minimal elastic energy of the system. With varying the film thickness, the wall attains a shape laying between these two limiting cases.

of mechanical compatibility. As it was mentioned before, a rotation of the wall in the clockwise direction from the mechanically compatible state leads to relaxation of the film-substrate misfit stresses by the elastic fields generated by the domain wall lattice mismatches, decreasing the elastic energy of the system and making such a rotation favourable. When the deviation of the wall is small, the negative energy of elastic interaction between the domain wall and film-substrate lattice mismatches $U_{\text{el}}^{\text{int}}$ depends linearly on the angle of domain wall rotation, due to the linear dependence of magnitude of the elastic fields generated by the wall on the rotation angle. At the same time, there is also the positive elastic energy of the incompatibility fields $U_{\text{el}}^{\text{DW}}$, which is proportional to the square of the angle of deviation. From these considerations, one can see that the orientation of the domain wall that corresponds to the minimal elastic energy of the structure differs from the mechanically compatible orientation formulated in [23], and is defined by the competition between $U_{\text{el}}^{\text{int}}$ and $U_{\text{el}}^{\text{DW}}$. In the considered BiFeO_3 structure, the shape of such domain wall is shown in Fig. 4.2 by the dash-dotted line.

Remarkably, each shape of the domain wall shown in Fig. 4.2 is defined by the only parameter $G\beta^2 h/\lambda$. The results obtained for BiFeO_3 sparse structures are applicable to other rhombohedral films having a similar geometry.

4.2 Ferroelastic domain walls in non-sparse domain structures

In the previous section, the shape of an individual DW is investigated in thin films, showing that large deviations of the wall off the mechanically compatible state are possible. At the same time, in thin ferroelectric films non-sparse domain structures are most often observed, and the applicability of the results obtained for an individual DW to such systems is questioned. In the following, estimations are given to the behaviour of the DW in films having non-sparse structures.

For the systems with non-sparse domain structures, a description for small angles of DW deviation is developed; the validity of this approach will be shown a posteriori. Films having periodic I-II alternate domain structures are considered, with DWs of straight planar shape, inclined with the same angle to the surface at all points. Similarly to the previous section, the elastic fields in the film are described by fictitious dislocations equivalently representing the inter-domain and film-substrate lattice mismatches. The mechanical incompatibility elastic distortions are generated by screw dislocations located at the DW, the film-substrate mismatch fields are generated by screw and edge dislocations at the film-substrate interface. Hereafter, only elastic fields generated by screw dislocations are described, since, as in previous section, edge dislocations do not have any influence on the DW orientation. Smallness of the DW deviations allows us to consider only linear effects of the DW inclination on the incompatibility elastic fields: for all considered DW inclinations the DW screw dislocations are fixed in the position of the mechanically compatible wall oriented at angle 45° to the film surface, their displacements with the domain wall deviation are neglected as a high-order effect. The Burgers vector density of dislocations has the constant value along the DW: $db^{\text{DW}}/dy = \pm 2\beta(\cot\phi - 1)$, where ϕ is the angle of inclination of the DW, sign '+' corresponds to the I-II transition between the domains with increasing x , sign '-' corresponds to the II-I transition between the domains with increasing x .

The considered geometry of the non-sparse structure is shown in Fig. 4.3. Elastic stresses are calculated using expression (4.4), with stresses generated by film-substrate screw dislocations $\sigma_{ij}^{\text{sub}}(x, y)$ and stresses generated by DW screw dislocations $\sigma_{ij}^{\text{DW}}(x, y)$ redefined for the

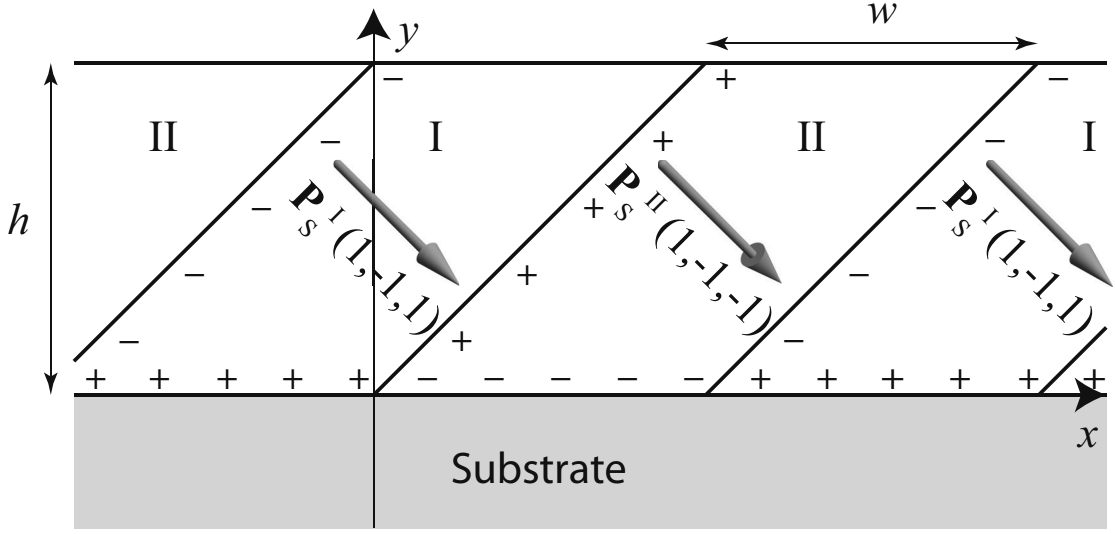


Figure 4.3: Schematics of the BiFeO₃ used for calculations in non-sparse domain structures. Symbols '+' represent screw dislocations having positive Burgers vector density db^{DW}/dy and db^{sub}/dx , symbols '-' represent dislocations with negative Burgers vector density – see the text. Here, the signs of the dislocations on the DW are shown for the case of a small deviation of the DW orientation in clockwise direction.

case of the non-sparse structure as follows:

$$\sigma_{ij}^{sub}(x, y) = -\beta \sum_k \int_0^w (-1)^k \sigma_{ij}^{33}(x, y; kw + x_0, 0) dx_0, \quad (4.22)$$

$$\sigma_{ij}^{DW}(x, y) = 2\beta \cdot (\cot \phi - 1) \sum_k \int_0^h (-1)^k \sigma_{ij}^{33}(x, y; kw + y_0, y_0) dy_0, \quad (4.23)$$

where w is the width of a domain. The energy of the system per one domain wall, comprised of the elastic energy of the fields generated by screw dislocations and of the DW self-energy, is calculated using the expression

$$U = \frac{\lambda h}{\sin \phi} + \frac{1}{2G} \int_{-\infty}^h \int_0^w (\sigma_{13}^2(x, y) + \sigma_{23}^2(x, y)) dx dy. \quad (4.24)$$

The angle of the DW inclination corresponding to the minimal energy of the system U [Eq. (4.24)] is computed numerically for varying thicknesses of BiFeO₃ film. For the calculation, the dependence of the domain width on the BiFeO₃ film thickness is taken from Ref. [42]. Figure 4.4 shows DWs inclination angles obtained for BiFeO₃ non-sparse structures, compared with the average DW inclination angle calculated for sparse structures. In films thicker than 40

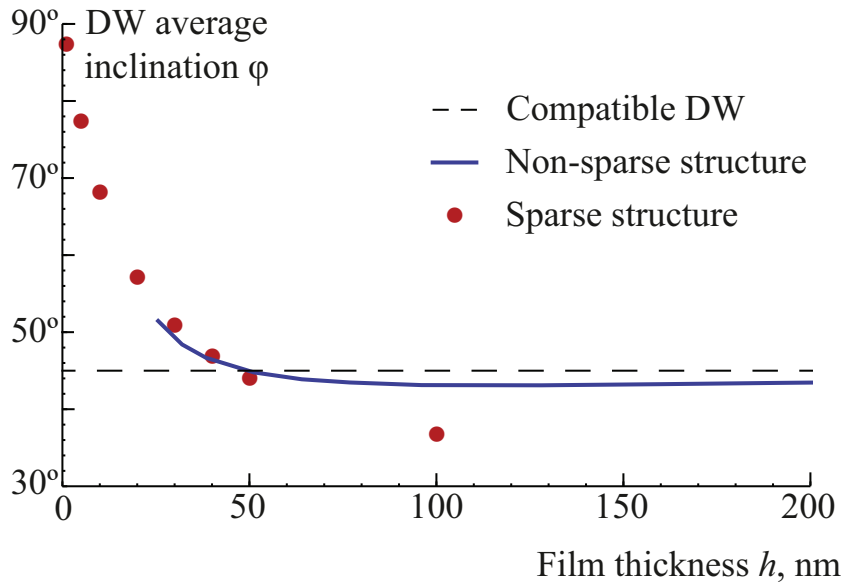


Figure 4.4: Average angles of inclination at different thicknesses of the BiFeO_3 film. Dots represent the results obtained in framework of the model developed for sparse structures, solid line shows the results for non-sparse structures. Dashed line shows the inclination of 45° of mechanically compatible DW.

nm, the inclination of the DW lies within 3° from the mechanically compatible DW orientation of 45° . With increasing the film thickness, the deviation of the DW off the mechanically compatible state decreases, which opposes to the behaviour of the single DW. In structures with a single wall, whole film is stressed due to the film-substrate lattice mismatch, and the DW tends to deviate by a large angle in order to relax the σ_{13} and σ_{23} shear stresses and minimize the elastic energy of the structure. In non-sparse structures, stress components σ_{13} and σ_{23} are essentially different from zero only within the region near the substrate of the size of the order of the domain width. Outside this region, a deviation of the wall leads to generation of additional elastic fields rather than relaxation. As a consequence, the deviation of the wall in non-sparse structures is not as favourable as in the structures with a single DW. In the limiting case of the film thickness tending to infinity, the film is characterized by dense domain pattern, stress components σ_{13} and σ_{23} are absent in the whole film, and the minimal elastic energy of the structure is given by the DW inclination of 45° to the surface since any deviation of the DW would lead to increase of the elastic energy.

4.3 Conclusions

To conclude, the shape of the ferroelastic DWs in films of rhombohedral geometry was investigated using BiFeO₃ thin films on substrate as an example, and the applicability of the requirement of the mechanical compatibility of the DW, conventionally used for description of domain structures, to ultrathin films was tried. A strong deviation of the DW off the mechanically compatible DWs was shown in films characterized by sparse domain structures. In ultrathin films, the DW orients normally to the film surface, which is the consequence of following the condition of minimal DW self-energy. In thick films, the DW orients according to the requirement of the minimal elastic energy of the system, also breaking the aforementioned condition and generating DW incompatibility elastic distortions. The shape of the DW in thick films corresponds to the most efficient relaxation of the film-substrate mismatch elastic fields by DW incompatibility elastic distortions. The results obtained for rhombohedral BiFeO₃ films with sparse structures can be easily extrapolated to other materials with similar geometries. In films with dense domain patterns, minimizing the elastic energy of the structure leads to the mechanically compatible orientation of the DW.

Appendix A. Energy of interaction between dislocations

The energy of interaction between two dislocations can be obtained as the change of the energy of the system as a result of creation of one dislocation in presence of the elastic field generated by the other.

In general, a dislocation having Burgers vector \mathbf{b} placed in an elastic field σ_{ij} interacts with the field via the Peach-Koehler force \mathbf{p} [46]:

$$p_i = e_{ijk} \sigma_{jl} b_l \tau_k, \quad (4.25)$$

where τ_k is a unit vector directed along the line of the dislocation. In the elastically isotropic medium with free surface at $y = h$, the energy of creation of a screw dislocation with line directed along z with Burgers vector $(0, 0, b_{1z})$ at the point (x_1, y_1) in the stress field $\sigma_{ij}(x, y)$ is equivalent to the work required to move the dislocation from the film surface (x_1, h) , i.e., from the state where dislocations do not interact, to the point (x_1, y_1) :

$$E_{\text{inter}}(x_1, y_1) = - \int_h^{y_1} p_2(x_1, y) dy = -b_{1z} \int_{y_1}^h \sigma_{13}(x_1, y) dy. \quad (4.26)$$

Chapter 4. Mechanically incompatible ferroelastic domain walls in thin films

The stress fields in the problem are generated by dislocations of three types: screw dislocations with lines directed along z , edge dislocations with lines directed along x , and edge dislocations having lines along z . Notably, the elastic fields generated by edge dislocations in the problem have zero component σ_{13} [47], therefore, as it follows from Eq. (4.26), screw and edge dislocations in the system do not interact with each other. Only interaction between screw dislocations in the system results in non-zero elastic energy which may control the DW orientation.

In order to find the energy of interaction between screw dislocations $E(x_1, y_1, b_{1z}; x_2, y_2, b_{2z})$, Eq. (4.26) is used with the stress component $\sigma_{13}(x, y) = b_{2z}\sigma_{13}^{33}(x, y; x_2, y_2)$, with $\sigma_{13}^{33}(x, y; x_2, y_2)$ given by Eq. (4.9). As a result, the expression (4.16) is obtained.

Appendix B. Derivation of equation (4.17) describing domain wall shape

Introducing dimensionless coordinates $\tilde{x}_i = x_i/h$, $\tilde{y}_i = y_i/h$ and dimensionless deviation function $\tilde{D}(\tilde{y}) = D(h\tilde{y})/h$, Eqs. (4.11)–(4.16) with Burgers vector densities db^{sub}/dx and db^{DW}/dy defined in Eqs. (4.7) and (4.8), respectively, can be rewritten as follows:

$$\begin{aligned}
 U = & \frac{\beta^2 Gh^2}{8\pi} \int_{-\infty}^{\infty} \int_{-\infty}^{\infty} e(\tilde{x}_1, 0; \tilde{x}_2, 0) d\tilde{x}_1 d\tilde{x}_2 \\
 & + \frac{\beta^2 Gh^2}{2\pi} \int_0^1 \int_0^1 e(\tilde{y}_1 + \tilde{D}(\tilde{y}_1), \tilde{y}_1; \tilde{y}_2 + \tilde{D}(\tilde{y}_2), \tilde{y}_2) \tilde{D}'(\tilde{y}_1) \tilde{D}'(\tilde{y}_2) d\tilde{y}_1 d\tilde{y}_2 \\
 & + \frac{\beta^2 Gh^2}{2\pi} \int_0^1 \int_{-\infty}^{\infty} e(\tilde{x}_1, 0; \tilde{y}_2 + \tilde{D}(\tilde{y}_2), \tilde{y}_2) \tilde{D}'(\tilde{y}_2) \text{sign } \tilde{x}_1 d\tilde{x}_1 d\tilde{y}_2 + \lambda h \int_0^1 \sqrt{1 + (1 + \tilde{D}'(\tilde{y}))^2} d\tilde{y}.
 \end{aligned} \tag{4.27}$$

In order to determine the shape of the domain wall that leads to the minimal energy of the system U , the energy is rewritten in the form suitable for application of variational methods

introducing the functional $L[\tilde{D}](\tilde{y}_2)$:

$$U = U_{\text{el}}^{\text{sub}} + \frac{\beta G h^2}{2\pi} \int_0^1 L[\tilde{D}(\tilde{y})](\tilde{y}_2) d\tilde{y}_2, \quad (4.28)$$

$$\begin{aligned} L[\tilde{D}](\tilde{y}_2) = & \int_0^1 e(\tilde{y}_1 + \tilde{D}(\tilde{y}_1), \tilde{y}_1; \tilde{y}_2 + \tilde{D}(\tilde{y}_2), \tilde{y}_2) \tilde{D}'(\tilde{y}_1) \tilde{D}'(\tilde{y}_2) d\tilde{y}_1 \\ & + e_s(\tilde{y}_2 + \tilde{D}(\tilde{y}_2), \tilde{y}_2) \tilde{D}'(\tilde{y}_2) + \frac{2\pi\lambda}{G\beta^2 h} \sqrt{1 + (1 + \tilde{D}'(\tilde{y}_2))^2}. \end{aligned} \quad (4.29)$$

A small variation of the function of deviation $\delta\tilde{D}(\tilde{y})$ is considered (restriction $\delta\tilde{D}(0) = 0$ is imposed). One can rewrite the functional L keeping only terms of the first order of smallness:

$$L[\tilde{D} + \delta\tilde{D}](\tilde{y}_2) \approx L[\tilde{D}](\tilde{y}_2) + \delta L[\tilde{D}, \delta\tilde{D}](\tilde{y}_2), \quad (4.30)$$

$$\begin{aligned} \delta L[\tilde{D}, \delta\tilde{D}](\tilde{y}_2) = & \int_0^1 \frac{\partial e}{\partial \tilde{x}_1}(\tilde{y}_1 + \tilde{D}(\tilde{y}_1), \tilde{y}_1; \tilde{y}_2 + \tilde{D}(\tilde{y}_2), \tilde{y}_2) \delta\tilde{D}(\tilde{y}_1) \tilde{D}'(\tilde{y}_1) \tilde{D}'(\tilde{y}_2) d\tilde{y}_1 \\ & + \int_0^1 \frac{\partial e}{\partial \tilde{x}_2}(\tilde{y}_1 + \tilde{D}(\tilde{y}_1), \tilde{y}_1; \tilde{y}_2 + \tilde{D}(\tilde{y}_2), \tilde{y}_2) \delta\tilde{D}(\tilde{y}_2) \tilde{D}'(\tilde{y}_1) \tilde{D}'(\tilde{y}_2) d\tilde{y}_1 \\ & + \int_0^1 e(\tilde{y}_1 + \tilde{D}(\tilde{y}_1), \tilde{y}_1; \tilde{y}_2 + \tilde{D}(\tilde{y}_2), \tilde{y}_2) \delta\tilde{D}'(\tilde{y}_1) \tilde{D}'(\tilde{y}_2) d\tilde{y}_1 \\ & + \int_0^1 e(\tilde{y}_1 + \tilde{D}(\tilde{y}_1), \tilde{y}_1; \tilde{y}_2 + \tilde{D}(\tilde{y}_2), \tilde{y}_2) \tilde{D}'(\tilde{y}_1) \delta\tilde{D}'(\tilde{y}_2) d\tilde{y}_1 \\ & + \frac{\partial e_s}{\partial \tilde{x}}(\tilde{y}_2 + \tilde{D}(\tilde{y}_2), \tilde{y}_2) \delta\tilde{D}(\tilde{y}_2) \tilde{D}'(\tilde{y}_2) + e_s(\tilde{y}_2 + \tilde{D}(\tilde{y}_2), \tilde{y}_2) \delta\tilde{D}'(\tilde{y}_2) \\ & + \frac{2\pi\lambda}{G\beta^2 h} \frac{1 + \tilde{D}'(\tilde{y}_2)}{\sqrt{1 + (1 + \tilde{D}'(\tilde{y}_2))^2}} \delta\tilde{D}'(\tilde{y}_2). \end{aligned} \quad (4.31)$$

Following the theory of variations, the shape of the wall defined by deviation $\tilde{D}(\tilde{y})$ corresponds to the minimal energy of the system when, for any variation $\delta\tilde{D}(\tilde{y})$, the corresponding variation of the energy is zero: $\int_0^1 \delta L[\tilde{D}, \delta\tilde{D}](\tilde{y}_2) d\tilde{y}_2 = 0$. Since function e is symmetric,

Chapter 4. Mechanically incompatible ferroelastic domain walls in thin films

$e(\tilde{x}_1, \tilde{y}_1; \tilde{x}_2, \tilde{y}_2) = e(\tilde{x}_2, \tilde{y}_2; \tilde{x}_1, \tilde{y}_1)$, the criterion on the DW shape can be rewritten as:

$$\int_0^1 (A(\tilde{y}_2) \delta \tilde{D}(\tilde{y}_2) + B(\tilde{y}_2) \delta \tilde{D}'(\tilde{y}_2)) d\tilde{y}_2 = 0, \quad (4.32)$$

$$A(\tilde{y}_2) = 2 \int_0^1 \frac{\partial e}{\partial \tilde{x}_2}(\tilde{y}_1 + \tilde{D}(\tilde{y}_1), \tilde{y}_1; \tilde{y}_2 + \tilde{D}(\tilde{y}_2), \tilde{y}_2) \tilde{D}'(\tilde{y}_1) d\tilde{y}_1 \tilde{D}'(\tilde{y}_2) + \frac{\partial e_s}{\partial \tilde{x}}(\tilde{y}_2 + \tilde{D}(\tilde{y}_2), \tilde{y}_2) \tilde{D}'(\tilde{y}_2) \quad (4.33)$$

$$B(\tilde{y}_2) = 2 \int_0^1 e(\tilde{y}_1 + \tilde{D}(\tilde{y}_1), \tilde{y}_1; \tilde{y}_2 + \tilde{D}(\tilde{y}_2), \tilde{y}_2) \tilde{D}'(\tilde{y}_1) d\tilde{y}_1 + e_s(\tilde{y}_2 + \tilde{D}(\tilde{y}_2), \tilde{y}_2) + \frac{2\pi\lambda}{G\beta^2 h} \frac{1 + \tilde{D}'(\tilde{y}_2)}{\sqrt{1 + (1 + \tilde{D}'(\tilde{y}_2))^2}} \quad (4.34)$$

After integration by part, the condition attains the following form:

$$\int_0^1 \left(\int_{\tilde{y}_2}^1 A(t) dt + B(\tilde{y}_2) \right) \delta \tilde{D}'(\tilde{y}_2) d\tilde{y}_2 = 0. \quad (4.35)$$

Requirement of fulfillment of this condition for any variation of deviation $\delta \tilde{D}(\tilde{y})$ leads to the following expression:

$$\int_{\tilde{y}_2}^1 A(t) dt + B(\tilde{y}_2) = 0, \quad (4.36)$$

from which the non-linear Fredholm integral equation (4.17) follows directly.

5 Inclined ferroelectric domain walls as reconfigurable metallic-like channels

Electronic transport at domain walls [26, 30, 48–51] or wall-interface junctions [52], a required cornerstone for domain wall nanoelectronics, is difficult to control due to the sensitivity of the conduction to the defect chemistry of the material [26, 53], its strong temperature dependence [26, 49, 54], and polarization-related hysteresis effects [48, 55]. Furthermore, displaced domain walls leave conductive footprints due to accumulated mobile defects [56], which questions the feasibility of rewritable domain wall based circuits. Because of these issues, electronic conductivity in domain walls since its first demonstration by Seidel et al. [30] remained elusive with a large dispersion in the reported transport data [26, 49, 50, 55, 57]. Metallic-like conductivity at domain walls was shown only transiently in individually switched nanodomains [58] or in so-called charged domain walls [29, 59–61], prepared individually using a special poling procedure. Stable metallic-type conduction was so far only shown in the case of strongly charged domain walls [29, 61, 62]. In strongly charged walls, where the normal component of the polarization to the wall experiences a discontinuity of the order of the spontaneous polarization, the generation of the bound charge at the domain boundary may result in its compensation with a narrow metallic-like conductive layer leading to the nonthermally activated transport [29]. However, the formation energy of charged domain walls is very high [63]. In addition, strong depolarizing fields, inversely proportional to the domain wall spacing, destabilize the walls when they are located in close proximity to each other (e.g., $< 1\mu\text{m}$ for BaTiO_3 crystals) [59].

While strongly charged domain walls might therefore be difficult to implement in electronics, another possibility exists that offers both the high conductivity of charged walls and the positional stability of neutral walls: when neutral ferroelectric domain walls are forced to bend off their neutral position, these nominally uncharged walls inevitably become partly

Chapter 5. Inclined ferroelectric domain walls as reconfigurable metallic-like channels

charged and thus may display metallic-like conductivity. The desired stability can be obtained for bent ferroelastic walls, as shown below.

Domain walls in bulk ferroelastic crystals acquire elastically compatible orientations [23]. As it was shown in Chapter 4, a small deviation of a wall from this equilibrium orientation results in the appearance of elastic fields of amplitude proportional to the rotation angle $\Delta\phi$, implying an energy increase in the system proportional to $(\Delta\phi)^2$. In the case of ferroelastic thin films, a lattice mismatch with the substrate produces elastic fields that can be relaxed by the rotation of the walls. The energy release due to this rotation is proportional to the rotation angle $\Delta\phi$. Therefore, in thin films the stable orientation of ferroelastic walls is tilted off the bulk equilibrium orientation by the angle $\Delta\phi$ which gives the highest overall energy reduction. This implies a possibility to tune the orientation of ferroelectric/ferroelastic walls in thin films via the control of the film-substrate lattice misfit and the configuration of the domain pattern. The higher the rotation angle $\Delta\phi$, the higher is the charge density in the wall and its conductivity.

Here, this reasoning is applied to the tetragonal $\text{Pb}(\text{Zr}, \text{Ti})\text{O}_3$ (PZT) films, and the concept of appearance of charged domain walls is given. A simplified model is developed, in framework of which the orientation of the wall is defined by the condition of minimal elastic energy of the system. The features of behaviour of the domain wall driven by elasticity are confirmed by more rigorous numerical phase-field modelings, which take into account effects of elasticity and electrostatics on the domain wall orientation. The conclusions of the model, namely the presence of the charged domain walls in the film, are confirmed by the experimental investigation of real PZT films.

5.1 Theoretical description of domain wall bending

A ferroelectric (001) tetragonal film with a/c domain patterns is investigated, where c -domains have their c -axis (the polar axis) perpendicular to the surface of the film and a -domains have their c -axis in the plane of the film, as illustrated in Fig. 5.1. The film is clamped on a cubic substrate with a lattice constant a_s slightly exceeding the lattice constant of the ferroelectric a ($a_s - a \ll c - a$, where c is the larger lattice constant of the ferroelectric), which leads to the domain structure composed of a c -monovariant with narrow a -domain inclusions [64]. Following the conditions of the domain wall electric neutrality and mechanical compatibility (see Chapter 2.2 for explicit expressions of the conditions), the walls surrounding a -domain inclusions are oriented by the angle 45° to the film surface. Any deviation of the walls off this

5.1. Theoretical description of domain wall bending

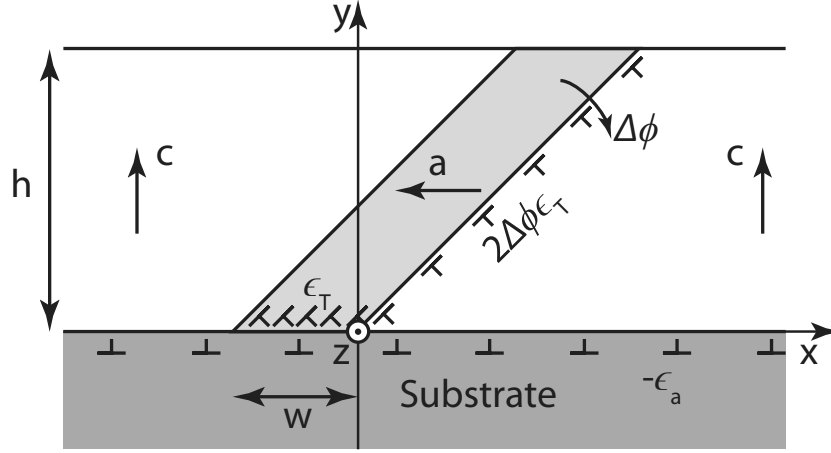


Figure 5.1: Schematic drawing of a film containing c -domain and a narrow a -domain. Fictitious dislocations describe the elastic fields in the ferroelastic thin film on a substrate, containing a narrow a -domain inclusion into c -domain. Symbol \perp denotes a -misfit dislocations with density $-\epsilon_a$, \sphericalangle – tetragonality dislocations having density ϵ_T under the a -domain and density $2\Delta\phi\epsilon_T$ on the right domain wall (see the text). $\Delta\phi$ is the rotation angle of the right domain wall from the compatible orientation.

permissible inclination leads to violation of electrical and mechanical conditions, generating bound charges and lattice mismatches on the domain walls.

Here, the methods developed in Chapter 4 are implemented for description of the elasticity-driven deviation of the domain walls off their permissible orientation (hereafter, also called *rotation* of the domain walls). Compared to BiFeO_3 films, which were investigated in Chapter 4, the impact of elastic effects on the domain structures in PZT is expected to be much stronger [20], therefore, the energy change related to the variation of the domain wall self-energy is neglected. For a sake of simplicity, as a mean to show the concept of elasticity-driven generation of charged domain walls, it is assumed that the bound charge on the domain walls is perfectly screened by the free charges, and the effects of electrostatics are excluded from the consideration of the problem. The orientation of the domain walls in PZT films is thus solely defined by the condition of the minimal elastic energy of the structure.

The lattice misfit between the film and the substrate, along with the lattice mismatches on the domain walls, generate mechanical incompatibility elastic fields in the film. In the considered system, only small angles of domain wall rotation are expected – which is shown a posteriori. This allows us to consider only linear effects of the domain wall rotation on the energy of the structure, and the following simplifications are made. The domain wall is considered to always have the planar shape, with the same angle of inclination to the film

Chapter 5. Inclined ferroelectric domain walls as reconfigurable metallic-like channels

surface in all its points. The lattice mismatches that generate the domain wall incompatibility elastic fields are considered to be fixed at the position of the mechanically compatible domain wall inclined by 45° to the film surface, their displacements with the domain wall rotation are neglected as a high order effect. Following the same logic as given in Chapter 4, the distribution of elastic stresses in the film $\sigma_{ij}(x, y)$ is sought by implementing the method of fictitious dislocations (see, e.g., [13, 14]):

$$\sigma_{ij}(x, y) = \iint \sigma_{ij}^{kl}(x, y; x_0, y_0) \alpha_{kl}(x_0, y_0) dx_0 dy_0, \quad (5.1)$$

where $\sigma_{ij}^{kl}(x, y; x_0, y_0)$ is the elastic stress field generated by a unit dislocation located at (x_0, y_0) , having Burgers vector directed along r_l and dislocation line along r_k direction, α_{kl} is the dislocations density tensor defined as [43]:

$$\alpha_{kl} = -e_{ijk} \frac{\partial \beta_{S_{jl}}}{\partial r_i}, \quad (5.2)$$

e_{ijk} is the Levi-Civita permutation symbol, $\beta_{S_{jl}} = \partial u_l / \partial r_j$ is the unsymmetrized misfit strain tensor describing spontaneous deformations of the lattices of the domains with respect to the substrate lattice, and u_l is the spontaneous displacement with respect to the unstrained substrate.

In the considered domain structure, a - and c -domains are characterized by the following unsymmetrized misfit strain tensors $\beta_{S_{ij}}^{(a)}$ and $\beta_{S_{ij}}^{(c)}$, respectively:

$$\beta_{S_{ij}}^{(c)} = \begin{pmatrix} \epsilon_a & 0 & 0 \\ 0 & \epsilon_c & 0 \\ 0 & 0 & \epsilon_a \end{pmatrix}, \quad \beta_{S_{ij}}^{(a)} = \begin{pmatrix} \epsilon_c & \epsilon_T & 0 \\ -\epsilon_T & \epsilon_a & 0 \\ 0 & 0 & \epsilon_a \end{pmatrix}, \quad (5.3)$$

where $\epsilon_a = (a - a_s) / a_s$ and $\epsilon_c = (c - a_s) / a_s$ are a and c film-substrate lattice mismatches, respectively, $\epsilon_T = (c - a) / a \approx \epsilon_c - \epsilon_a$ is the film tetragonality factor.

Using Eqs. (5.2) and (5.3), the system of fictitious dislocations that equivalently describes elastic fields generated by inter-domain and film-substrate lattice mismatches was obtained.

5.1. Theoretical description of domain wall bending

As a result, expression for the stress in the structure (5.1) was rewritten in the following form:

$$\sigma_{ij}(x, y) = \sigma_{ij}^c(x, y) + \sigma_{ij}^a(x, y) + \sigma_{ij}^{\text{DWR}}(x, y) + \sigma_{ij}^{\text{DWL}}(x, y), \quad (5.4)$$

$$\sigma_{ij}^c(x, y) = \sum_k \int_{\Gamma_c} \sigma_{ij}^{3k}(x, y; x_0, 0) \frac{db_k^c}{dx} dx_0, \quad (5.5)$$

$$\sigma_{ij}^a(x, y) = \sum_k \int_{\Gamma_a} \sigma_{ij}^{3k}(x, y; x_0, 0) \frac{db_k^a}{dx} dx_0, \quad (5.6)$$

$$\sigma_{ij}^{\text{DWR}}(x, y) = \sum_k \int_0^h \sigma_{ij}^{3k}(x, y; y_0, y_0) \frac{db_k^{\text{DWR}}}{dy} dy_0, \quad (5.7)$$

$$\sigma_{ij}^{\text{DWL}}(x, y) = \sum_k \int_0^h \sigma_{ij}^{3k}(x, y; y_0 - w, y_0) \frac{db_k^{\text{DWL}}}{dy} dy_0, \quad (5.8)$$

$$\frac{d\mathbf{b}^c}{dx} = (-\epsilon_a, 0, 0), \quad (5.9)$$

$$\frac{d\mathbf{b}^a}{dx} = (\epsilon_T - \epsilon_a, \epsilon_T, 0), \quad (5.10)$$

$$\frac{d\mathbf{b}^{\text{DWR}}}{dy} = 2(\Delta\phi)_R \cdot (\epsilon_T, \epsilon_T, 0), \quad (5.11)$$

$$\frac{d\mathbf{b}^{\text{DWL}}}{dy} = -2(\Delta\phi)_L \cdot (\epsilon_T, \epsilon_T, 0), \quad (5.12)$$

where $\Gamma_c = (-\infty, -w) \cup (0, \infty)$ is the range of x -coordinates corresponding to the c -domain, $\Gamma_a = (-w, 0)$ is the range of x -coordinates corresponding to the a -domain, $(\Delta\phi)_{R,L}$ are the angles of rotation of the right (index R) and of the left (index L) domain wall in the clockwise direction as depicted in Fig. 5.1. In these notations, $\sigma_{ij}^c(x, y)$ and $\sigma_{ij}^a(x, y)$ are the elastic stresses generated by the sets of dislocations located at the c -domain/substrate and a -domain/substrate interfaces, correspondingly, $\sigma_{ij}^{\text{DWR},L}(x, y)$ are the elastic stresses generated by the sets of dislocations located at the right (index R) and at the left (index L) domain wall. The notation of Burgers vector density is also introduced: $(d\mathbf{b}^c/dx)$, $(d\mathbf{b}^a/dx)$, $(d\mathbf{b}^{\text{DWR}}/dy)$, and $(d\mathbf{b}^{\text{DWL}}/dy)$ describe the dislocations under the c -domain, under the a -domain, at the right domain wall, and at the left wall, respectively. In all cases, the dislocations are edge dislocations with lines directed along z . The elastic field $\sigma_{ij}^{3k}(x, y; x_0, y_0)$ describes the stresses generated by a unit dislocation having line along z , located at point (x_0, y_0) in an elastically isotropic medium with the free surface at $y = h$ and having Burgers directed along r_k . Explicit expressions for the fields $\sigma_{ij}^{3k}(x, y; x_0, y_0)$ ($k = 1, 2$) are given in Appendix A.

Strictly speaking, expression (5.4) should also include the stress fields generated by the set of edge dislocations at the film-substrate interface having the line directed along x and

Chapter 5. Inclined ferroelectric domain walls as reconfigurable metallic-like channels

the Burgers vector density $d\mathbf{b}/dz = (0, 0, \epsilon_a)$. This set of dislocations describes the lattice mismatch between the film and the substrate in z -direction, and is characterized by the uniform distribution of the dislocations at the whole film-substrate interface. However, it was shown that this elastic field does not interfere with any of the stress contributions included in Eq. (5.4) and thus does not have any effect on the orientation of the domain walls (see Appendix A for details). For this reason, this type of dislocations is excluded from the consideration of the problem.

As it can be seen from Eqs. (5.4)–(5.12), there are two principal types of fictitious dislocations that control the domain wall orientation: $d\mathbf{b}/dx = (-\epsilon_a, 0, 0)$, hereafter called a -misfit edge dislocations, and $d\mathbf{b}/dx = (\epsilon_T, \epsilon_T, 0)$, hereafter called tetragonality edge dislocations. In these terms, the substrate/ c -domain incompatibility is described by the a -misfit dislocations, while the incompatibility between the substrate and a -domain is explained by the superposition of a -misfit and tetragonality dislocations; the a/c -domain incompatibility is described by tetragonality dislocations with Burgers vector density reduced by a factor of $2(\Delta\phi)_R$ at the right wall and $-2(\Delta\phi)_L$ at the left wall. The system of dislocations controlling the domain walls orientation is schematically shown in Fig. 5.1 for the case where only the right domain wall deviates off its permissible orientation. Hereafter, in order to show the concept of deviation of the domain wall off its permissible inclination, only rotation of the right domain wall is considered.

Similarly to electric charges in electrostatics, the appearance of the domain wall fictitious dislocations is favourable in presence of a -misfit dislocations, which have opposite sign, and unfavourable in presence of tetragonality dislocations of the same sign. A competition between these two interactions leads to either increase or decrease of elastic energy proportional to the bending angle $\Delta\phi$ for the case of a small angle of the domain wall rotation. Besides, introducing the domain dislocations themselves costs energy proportional to $(\Delta\phi)^2$. The $\Delta\phi$ -dependencies of the aforementioned energies are clear from the fact that the elastic energy of the system is proportional to the square of the elastic stress, which has two contributions: one associated with the mechanical incompatibility of the wall, proportional to $\Delta\phi$, and the other due to the film-substrate mismatch, which is independent of $\Delta\phi$. Calculations based on the dislocation theory (elastic isotropy approximation), given in Appendix A, yields the energy of the system in the following form:

$$\Delta U(\Delta\phi) = \frac{1}{2}k_1\epsilon_T^2(\Delta\phi)^2 - k_2\epsilon_T^2\Phi\Delta\phi - k_2\epsilon_T^2f\left(\frac{w}{h}\right)\Delta\phi, \quad (5.13)$$

where $\Phi = (a_s - a)/(c - a)$ is the relative coherency strain, k_1 and k_2 are positive coefficients

5.1. Theoretical description of domain wall bending

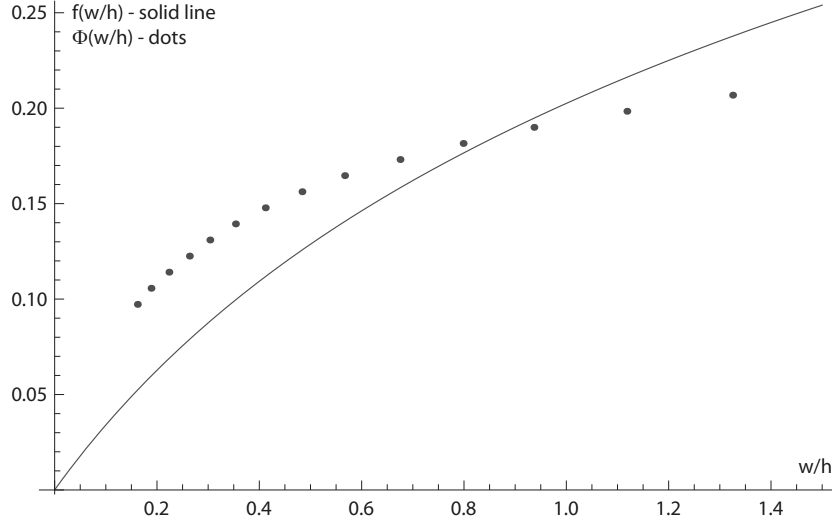


Figure 5.2: Functions f and Φ , entering Eqs. (5.13) and (5.15) for domain wall rotation angle dependence on the a -domain width to film thickness ratio w/h . The function f (solid line) describes interaction of the domain wall with tetragonality fictitious dislocations under the a -domain. The relative coherency strain Φ (dots) enters the expression for the interaction between domain wall and a -misfit dislocations. The relationship between $\Phi = (a_s - a)/(c - a)$ and a -domain width w was taken from the phase-field simulations for PZT film of thickness $h = 60$ nm.

satisfying the relation

$$\frac{k_2}{k_1} = \frac{\pi}{1 + \ln 4}, \quad (5.14)$$

$f(w/h)$ is a positive function that does not depend on parameters of the system except for w/h (Fig. 5.2) – see Appendix A for the details of its calculation. This function describes the impact of the a -domain misfit dislocations on the wall and thus it naturally goes to zero once the domain width w goes to zero. In expression (5.13), the first term in r.h.s. is the incompatibility energy of the wall, proportional to $(\Delta\phi)^2$. The second and the third terms control the stress release due to the wall rotation. The second term is the wall/ c -domain misfit coupling energy while the third is the coupling energy between the wall and the lattice misfit in the narrow a -domain; the positive function behaviour $f(w/h) \rightarrow 0$ once $w/h \rightarrow 0$ (Fig. 5.2) reflects the fact that the interaction with the a -domain vanishes when its width goes to zero.

Minimizing the energy Eq. (5.13) with respect to $\Delta\phi$, one can find that the equilibrium angle of rotation depends only on two parameters: the relative coherency strain $\Phi = (a_s -$

Chapter 5. Inclined ferroelectric domain walls as reconfigurable metallic-like channels

$a)/(c - a)$ and relative domain width w/h . It reads:

$$\Delta\phi = \frac{\pi}{1 + \ln 4} \left(\Phi - f\left(\frac{w}{h}\right) \right). \quad (5.15)$$

Thus, one can recognize two channels controlling the orientation of the wall: via the relative coherency strain Φ and via the a -domain width w . Analysis of Eq. (5.15) shows that a reduction in a -domain width (and consequently also reduction of $f(w/h)$) leads to an *increase* of the rotation angle, deviation of the wall from its compatible orientation, and generation of charged domain wall. This reasoning is oversimplified but its consequence, namely, the increase of the rotation angle upon reduction of the a -domain width, does hold.

One should remark that, in the real situation, Φ and w are not independent and, in the case of an equilibrium domain pattern, they are strongly correlated: a reduction of w corresponds to that of Φ . Thus, the impact of the domain width on the wall orientation will be opposed by that of the relative coherency strain. Analysis of this competition was conducted for the case of PZT of thickness $h = 60$ nm. For this, dependence of a -domain width on the coherency strain Φ was taken from phase-field simulations [40]. As a result, for the case of interest ($w \ll h$), the impact of domain width still controls the magnitude of the domain wall rotation, while the counteraction of that of the relative coherency strain just reduces the total effect. This is illustrated in Fig. 5.2 where the functions $f(w/h)$ (calculated in Appendix A) and $\Phi(w/h)$ (obtained in numerical simulations [40]) are plotted vs. (w/h) . It is seen that, for $w < 0.8h$, the difference $\Phi(w/h) - f(w/h)$ increases on decreasing the a -domain width, implying, according to Eq. (5.15), larger wall rotation for thinner a -domains.

The similar treatment is available for the left domain wall of the a -domain shown in Fig. 5.1. In contrast to the right wall addressed above, at such wall the dislocations with positive Burgers vector density $d\mathbf{b}/dx$ appear once the wall is rotated in *counter-clockwise* direction [Eq. (5.12)]. This entails its counter-clockwise elasticity-driven rotation off the permissible orientation. The trends controlling the rotation remain the same as in the case of the right domain wall. It was shown that the angle of rotation of the left domain wall is, in general, smaller than the angle of the right wall rotation.

5.2 Comparison with numerical simulations

The features of deviation of the domain walls in the considered a/c -structure off the permissible orientation were confirmed by the numerical phase-field simulations (performed by T. Sluka, see [40] for details) – see Fig. 5.3 where the principal conclusions of the numerical

simulations are shown. In accordance to the predictions of the theory, the decrease of the lattice constant of the substrate leads to decrease of the domain width and, consequently, to increase of the angle of deviation (Fig. 5.3(a)). In a deviated domain wall, the electric neutrality of the wall breaks, generating the bound charges. It was shown in numerical calculations that a larger deviation of the domain wall off its mechanically compatible state leads to a higher density of the free electrons on the wall, which compensate the generation of the bound charges. As a consequence, a larger conductivity in narrower a -domain inclusion is predicted.

Dependence of the density of free charges on the width of the a -domain inclusion obtained during numerical simulations, shown in Fig. 5.3(c), can be qualitatively explained in the framework of the theory developed in Chapter 5.1. In the approximation where all bound charges at the domain walls are compensated by free electrons, the surface density n of the carriers on the domain wall can be found using the formula

$$n = \frac{1}{e} (\mathbf{P}_S^{(c)} - \mathbf{P}_S^{(a)}) \cdot \mathbf{n} = \frac{P_S}{e} (\cos \phi - \sin \phi) \approx \frac{\sqrt{2} P_S}{e} \Delta \phi = \frac{\sqrt{2} \pi P_S}{e(1 + \ln 4)} \left(\Phi\left(\frac{w}{h}\right) - f\left(\frac{w}{h}\right) \right), \quad (5.16)$$

where e is electron charge, $\mathbf{P}_S^{(a)}$ and $\mathbf{P}_S^{(c)}$ are spontaneous polarizations of a - and c -domain, correspondingly, \mathbf{n} is the normal to the domain wall, ϕ is the angle of the domain wall inclination. Here, results obtained in Eq. (5.15) were used. Dependence of the concentration on the a -domain width obtained in Eq. (5.16) is shown in Fig. 5.3(c).

To sum up the theoretical description of the a/c -domain structure, in order to have stable domain walls with non-thermally activated conduction, the presence of narrow a -domain inclusion in the film is necessary. This can be reached in a highly tetragonal film on a cubic substrate whose lattice parameter is slightly larger than the small lattice parameter of the film [64]. It is demonstrated experimentally by Stolichnov et al that this concept works [40].

5.3 Comparison with experiments

In [40], highly tetragonal PZT films (Zr/Ti=10:90) were grown on DyScO₃ (DSO) substrate having a small tensile lattice mismatch with respect to the c -domains of the PZT. Twenty nanometres of SrRuO₃ bottom electrodes were introduced between DSO and PZT. The 60 nm thick PZT film was mainly c -oriented having 10 nm wide a -domains (Fig. 5.4a). Ambient conductive atomic force microscope (cAFM) measurements showed stable current traces that closely reproduced the a -domain pattern, Fig. 5.4b,c. Ultrahigh vacuum (UHV) scanning force microscope using conductive diamond probes showed similar results with clear conduction

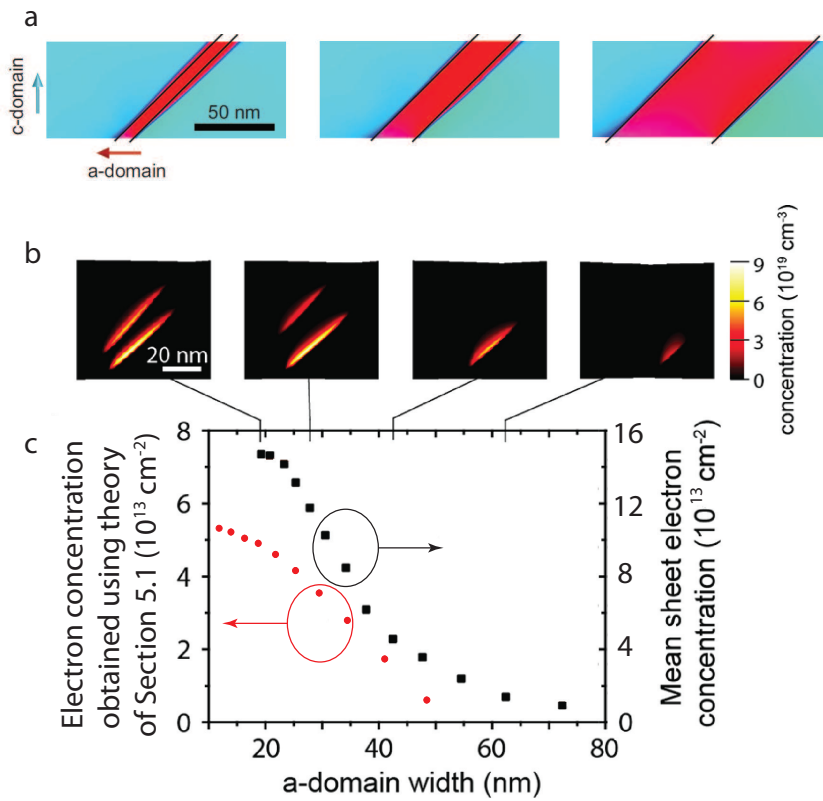


Figure 5.3: Results of the numerical simulations of PZT 60 nm films [40] at temperature 50 K. (a) Illustration of domain wall bending on phase field calculated a -domains of different widths. Inclination of domain walls (boundaries between the blue and red regions) is shown with respect to the ideal neutral orientation (indicated by the black lines). The domain walls bending is larger at narrower a -domains. (b) Colour scale map of the phase-field calculated electron concentration for different a -domain widths. (c) Plot of mean free electron concentration at the domain walls versus the a -domain width compared with the electron concentration obtained using the results of theoretical description developed in Chapter 5.1.

signal from a -domains. Remarkably the measured conduction at the a -domains showed very weak temperature dependence throughout a wide temperature range from 300 down to 4 K. cAFM scans measured under constant tip bias of -7 V at 54 K (Fig. 5.4e) and 4 K (Fig. 5.4g) are shown with their corresponding topography maps, Fig. 5.4d,f, respectively. The a -domains seen on the topography images are signaled in cAFM scans by clear conduction traces, while the c -domains show no current. The current measured through the cross-section of the conduction line (averaged over 40 lines) at 4 K (Fig. 5.4j) and 54 K (Fig. 5.4i) are similar to each other and comparable with the ambient measurements (Fig. 5.4h). The conduction maps were reproducible and the measured currents did not change significantly when a sequence of maps was taken under identical conditions.

5.4 Conclusions

To conclude, the concept of elasticity-driven deviation of the ferroelastic domain wall by relaxation of the film-substrate misfit stresses, which was developed in Chapter 4, was implemented to tetragonal (001) PZT film with a/c -domain structure. Specifically, the structures having narrow a -domain inclusions were investigated. It was shown that as a result of interaction of domain walls with the film-substrate misfit elastic fields, the walls deviate off their permissible orientation, breaking their electric neutrality. The deviation of the wall is favourable in the presence of c -domain and unfavourable in the presence of a -domain. As a result, in thin films with a narrower a -domain inclusion the deviation of the walls is more prominent. The theoretical development is supported by experimental observations of PZT films by Stolichnov et al, where metallic-like conductivity of domain walls of narrow a -domain inclusions was reported. The conductivity of the walls originates from the generation of free electrons compensating the bound charges appearing at the walls during their deviation.

Appendix A. Derivation of the elastic energy vs domain wall rotation angle dependence

To obtain expression (5.13) for the energy change during domain wall rotation, the following logic is used. We begin with the expression for Peach-Koehler force p_i with which a stress field σ_{ij} acts on a dislocation with Burgers vector b_i [46]:

$$p_i = e_{ijk} \sigma_{jl} b_l \tau_k \quad (5.17)$$

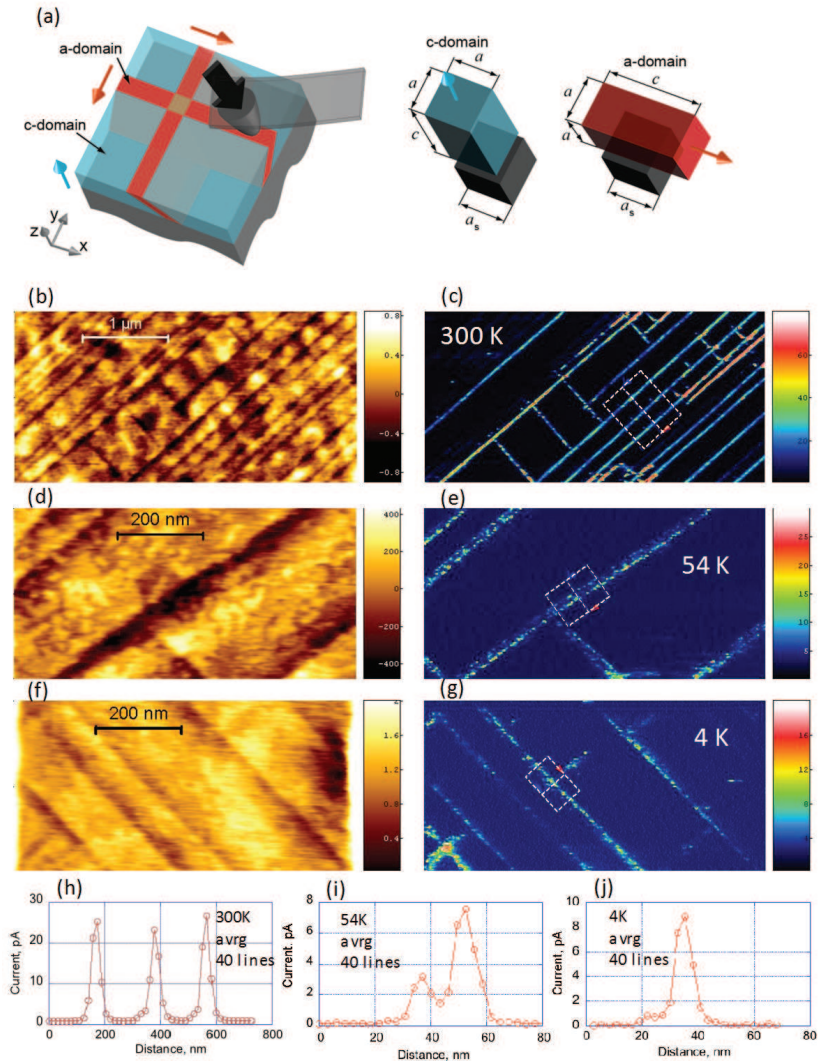


Figure 5.4: Conduction along *a*-domains in 60 nm thick PZT film measured by cAFM. (a) Illustration of the *a/c*-domain pattern in the tetragonal film on the substrate with the AFM tip probing the surface. The *c*-domains (*a*-domains) have their *c* (*a*) lattice parameter perpendicular to the surface. The colour scheme is substrate (dark gray), *c*-domains (blue), and *a*-domains (red). Blue and red arrows show the polarization direction for *c*- and *a*-domains, respectively. (b,c) Topography and conduction map measured at ambient conditions under dc tip bias of -6.5 V. (d,e) Topography and conduction map measured at 54 K under dc tip bias of -7 V. (f,g) Topography and conduction map measured at 4 K under dc tip bias of -7 V. (h-j) Cross sections of the conductive traces averaged over 40 lines measured on the images (c,e,g), respectively. The areas used for the measurements are marked on the corresponding images with white dashed frames.

where e_{ijk} is Levi-Civita permutation symbol, τ_k is the unit vector parallel to the dislocation line.

In the framework of the problem, in the elastically isotropic medium with free surface at $y = h$, the energy of creation of a screw dislocation with line directed along z with Burgers vector $\mathbf{b} = (b_1, b_2, 0)$ at the point (x, y) in the stress field $\sigma_{ij}(x, y)$ is equivalent to the work required to move the dislocation from the film surface (x, h) , i.e., from the state where dislocations do not interact, to the point (x, y) :

$$E_{\text{inter}}(x, y; \mathbf{b}) = - \int_h^y p_2(x, y_0) dy_0 = - \int_y^h (b_1 \sigma_{11}(x, y_0) + b_2 \sigma_{12}(x, y_0)) dy_0. \quad (5.18)$$

To calculate the energy (5.18), the explicit expressions for the stresses generated by a unit dislocation in semi-infinite space obtained by Head [47] in the approximation of elastic

isotropy (dislocation is located at point (x_0, y_0) , film surface is at $y = h$) are used:

$$\sigma_{11}^{31}(x, y; x_0, y_0) = \frac{E}{4\pi(1-\nu^2)} \left(-\frac{y'(3x'^2 + y'^2)}{(x'^2 + y'^2)^2} - \frac{(2h' - y')(3x'^2 + (2h' - y')^2)}{(x'^2 + (2h' - y')^2)^2} - 2h' \frac{x'^4 - 6x'^2(h' - y')(2h' - y') - (2h' - y')^3 y'}{(x'^2 + (2h' - y')^2)^3} \right), \quad (5.19)$$

$$\sigma_{22}^{31}(x, y; x_0, y_0) = \frac{E}{4\pi(1-\nu^2)} \left(\frac{y'(x'^2 - y'^2)}{(x'^2 + y'^2)^2} + \frac{(2h' - y')(x'^2 - (2h' - y')^2)}{(x'^2 + (2h' - y')^2)^2} - 2h' \frac{x'^4 + 6x'^2(h' - y')(2h' - y') - (h' + 3(h' - y'))(2h' - y')^3}{(x'^2 + (2h' - y')^2)^3} \right), \quad (5.20)$$

$$\sigma_{12}^{31}(x, y; x_0, y_0) = \frac{E}{4\pi(1-\nu^2)} \left(\frac{x'(x'^2 - y'^2)}{(x'^2 + y'^2)^2} - \frac{x'(x'^2 - (2h' - y')^2)}{(x'^2 + (2h' - y')^2)^2} + 4h' x' \frac{(x'^2 - 3(2h' - y')^2)(h' - y')}{(x'^2 + (2h' - y')^2)^3} \right), \quad (5.21)$$

$$\sigma_{11}^{32}(x, y; x_0, y_0) = \frac{E}{4\pi(1-\nu^2)} \left(\frac{x'(x'^2 - y'^2)}{(x'^2 + y'^2)^2} - \frac{x'(x'^2 - (2h' - y')^2)}{(x'^2 + (2h' - y')^2)^2} - 4h' x' \frac{x'^2(2h' + 3(h' - y')) + (2h' - y')^2(h' + y')}{(x'^2 + (2h' - y')^2)^3} \right), \quad (5.22)$$

$$\sigma_{22}^{32}(x, y; x_0, y_0) = \frac{E}{4\pi(1-\nu^2)} \left(\frac{x'(x'^2 + 3y'^2)}{(x'^2 + y'^2)^2} - \frac{x'(x'^2 + 3(2h' - y')^2)}{(x'^2 + (2h' - y')^2)^2} + 4h' x' \frac{(x'^2 - 3(2h' - y')^2)(h' - y')}{(x'^2 + (2h' - y')^2)^3} \right), \quad (5.23)$$

$$\sigma_{12}^{32}(x, y; x_0, y_0) = \frac{E}{4\pi(1-\nu^2)} \left(\frac{y'(x'^2 - y'^2)}{(x'^2 + y'^2)^2} + \frac{(2h' - y')(x'^2 - (2h' - y')^2)}{(x'^2 + (2h' - y')^2)^2} - 2h' \frac{x'^4 - 6x'^2(h' - y')(2h' - y') - (2h' - y')^3 y'}{(x'^2 + (2h' - y')^2)^3} \right), \quad (5.24)$$

where notations $x' = x - x_0$, $y' = y - y_0$, $h' = h - y_0$ are used.

Expressions (5.19)–(5.24) are applied directly to Eqs. (5.4)–(5.12), and the distribution of the elastic field generated by the set of dislocations is calculated. For simplicity and clearness of the analysis of the energy of interaction between dislocations, expression (5.4) for the stresses is rewritten in the following equivalent form:

$$\sigma_{ij}(x, y) = \sigma_{ij}^{a\text{-mis}}(x, y) + \sigma_{ij}^T(x, y) + \sigma_{ij}^{\text{DW}_R}(x, y) + \sigma_{ij}^{\text{DW}_L}(x, y), \quad (5.25)$$

where $\sigma_{ij}^{a\text{-mis}}(x, y)$ is the field generated by a -misfit dislocations (shown by symbols \perp in

Fig. 5.1), and $\sigma_{ij}^T(x, y)$ is the stress generated by the tetragonality dislocations (\sphericalangle in Fig. 5.1):

$$\sigma_{ij}^{a\text{-mis}}(x, y) = - \int_{-\infty}^{\infty} \epsilon_a \sigma_{ij}^{31}(x, y; x_0, 0) dx_0, \quad (5.26)$$

$$\sigma_{ij}^T(x, y) = \int_{-w}^0 (\epsilon_T \sigma_{ij}^{31}(x, y; x_0, 0) + \epsilon_T \sigma_{ij}^{32}(x, y; x_0, 0)) dx_0. \quad (5.27)$$

Below, the case is considered where there is only rotation of the right domain wall. During the rotation of the wall, the tetragonality dislocations appear, and the elastic energy of the system changes via three types of interaction: interaction of the wall dislocations with the stress generated by a -misfit dislocations ΔU^{w-a} , interaction between the wall dislocations and the field generated by film-substrate tetragonality dislocations ΔU^{w-T} , and self-interaction of the wall dislocations with the field generated by the wall ΔU^{w-w} . The explicit expressions for the change of the elastic energy as a result of these interactions are as follows:

$$\Delta U(\Delta\phi) = \Delta U^{w-w} + \Delta U^{w-T} + \Delta U^{w-a}, \quad (5.28)$$

$$\begin{aligned} \Delta U^{w-w} &= \frac{1}{2} \int_0^h E_{\text{inter}}^{w-w} \left(y, y; \frac{d\mathbf{b}^{DW_R}}{dy} \right) dy \\ &= -\frac{1}{2} \int_0^h \int_y^h (2\Delta\phi \epsilon_T \sigma_{11}^{DW_R}(y, y_0) + 2\Delta\phi \epsilon_T \sigma_{12}^{DW_R}(y, y_0)) dy_0 dy, \end{aligned} \quad (5.29)$$

$$\begin{aligned} \Delta U^{w-T} &= \int_0^h E_{\text{inter}}^{w-T} \left(y, y; \frac{d\mathbf{b}^{DW_R}}{dy} \right) dy \\ &= - \int_0^h \int_y^h (2\Delta\phi \epsilon_T \sigma_{11}^T(y, y_0) + 2\Delta\phi \epsilon_T \sigma_{12}^T(y, y_0)) dy_0 dy, \end{aligned} \quad (5.30)$$

$$\begin{aligned} \Delta U^{w-a} &= \int_0^h E_{\text{inter}}^{w-a} \left(y, y; \frac{d\mathbf{b}^{DW_R}}{dy} \right) dy \\ &= - \int_0^h \int_y^h (2\Delta\phi \epsilon_T \sigma_{11}^{a\text{-mis}}(y, y_0) + 2\Delta\phi \epsilon_T \sigma_{12}^{a\text{-mis}}(y, y_0)) dy_0 dy, \end{aligned} \quad (5.31)$$

where $E_{\text{inter}}^{w-w}(x, y; \mathbf{b})$, $E_{\text{inter}}^{w-T}(x, y; \mathbf{b})$, and $E_{\text{inter}}^{w-a}(x, y; \mathbf{b})$ are the energies of interaction of a dislocation with Burgers vector $\mathbf{b} = (b_1, b_2, 0)$ and line along z with stress fields $\sigma_{ij}^{DW_R}(x, y)$, $\sigma_{ij}^T(x, y)$ and $\sigma_{ij}^{a\text{-mis}}(x, y)$, respectively ($E_{\text{inter}}(x, y; \mathbf{b})$ [Eq. (5.18)] with corresponding stress fields used in place of $\sigma_{ij}(x, y)$).

Chapter 5. Inclined ferroelectric domain walls as reconfigurable metallic-like channels

Substituting Eqs. (5.7),(5.11),(5.26),(5.27) along with Eqs. (5.19)–(5.24) into Eqs. (5.28)–(5.31) leads to the following expressions for energies of interactions:

$$\Delta U^{w-w} = \frac{(1 + \ln 4)Eh^2}{2\pi(1 - \nu^2)} \epsilon_T^2 (\Delta\phi)^2, \quad (5.32)$$

$$\Delta U^{w-T} = -\frac{Eh^2}{1 - \nu^2} \epsilon_T^2 f\left(\frac{w}{h}\right) \Delta\phi, \quad (5.33)$$

$$\Delta U^{w-a} = -\frac{Eh^2}{1 - \nu^2} \epsilon_T \epsilon_a \Delta\phi, \quad (5.34)$$

$$(5.35)$$

where $f(w/h)$ is a positive non-dimensional function obtained numerically, depicted in Fig. 5.2. The obtained expressions for the energies ΔU^{w-w} , ΔU^{w-T} and ΔU^{w-a} correspond to the first, second and third term, respectively, of Eq. 5.13, where coefficients k_1 and k_2 are defined as:

$$k_1 = \frac{(1 + \ln 4)Eh^2}{\pi(1 - \nu^2)}, \quad (5.36)$$

$$k_2 = \frac{Eh^2}{1 - \nu^2}. \quad (5.37)$$

A remark should be made about the interaction between the domain wall dislocations and the dislocations on the film-substrate interface. As it was mentioned in Section 5.1, the elastic stresses (5.25), strictly speaking, should also include the stresses generated by the set of edge dislocations at the film-substrate interface having the line directed along x and the Burgers vector density $d\mathbf{b}/dz = (0, 0, \epsilon_a)$. This set of dislocations describes the lattice mismatch between the film and the substrate in z -direction, and is characterized by the uniform distribution of the dislocations at the whole film-substrate interface. It can be shown (see, e.g., [14]) that this set of dislocation generates the uniform stress field characterized by the only non-zero component σ_{33} of the stress tensor. Substituting this result to the expression (5.18) for energy of interaction of domain wall dislocations with a stress field, one immediately comes to the conclusion that this interaction is absent, and the aforementioned set of dislocations does not have any influence on the domain wall orientation.

6 Narrow ferroelastic domains and their sparse patterns in tetragonal ferroelectric thin films

Ferroelastic domain structures in thin films are of high interest for both fundamental and applied research. It is known that domain patterns to a great extent determine electromechanical properties of a ferroelectric thin film, which can be profitably used for applications ranging from tunnelling diodes to actuators and sensors [65]. The type of the ferroelastic domains and patterns that arise in the film is determined by the symmetry of the material, the crystallographic orientation of the film, and the mismatch between the lattice constants of the substrate and of the thin film [20]. With the development of nanotechnology there is growing interest in individual narrow domains and domain walls [7]. Engineering of nano-scale domain patterns for potential agile electronic applications became a hot topic [64, 66, 67]. Widespread examples are so called *c/a/c* domain structures, which arise in tetragonal films when lattice constants of the substrate are between the shorter "a" and longer "c" film's lattice constants. A smart method to control the domain structure that appear is the use of substrates with anisotropic mismatch strain [64, 66, 68]. The mismatch anisotropy allows to control the direction in which the domains grow, which was not possible in case of conventionally used substrates with square lattice termination. In the systems with small tensile mismatch for *c*-domains, the fraction of *a*-domains is typically small and they exist in the form of narrow inclusions into *c*-monovariant. A cross-hatched or parallel - stripe (lamellar) pattern may appear depending on growth conditions. These domains appear naturally and may be modified using Piezo-Force-Microscopy (PFM) [69]. Of interest is the dependence of domain widths and periodicity on the parameters of the system. A classical theory by Roytburd [70] suggests that both the domain periodicity and width of the domains is proportional to the square root of the film's thickness in analogy to Kittel's law for ferromagnetic systems. This theoretical prediction has found confirmation in relatively thick ferroelectric films [7]. However in thinner films large deviations from this law were documented [66]. The reason for this is that the classical theory

Chapter 6. Narrow ferroelastic domains and their sparse patterns in tetragonal ferroelectric thin films

[70] is written for a system of domains with periodicity much smaller than film thickness (so-called dense pattern), whereas in very thin films domain spacing becomes comparable with film thickness. A comprehensive study of periodical $c/a/c$ domain patterns with arbitrary domain width and fraction was offered by Pertsev *et al.* in Ref. 14. Individual a-domain stripe inclusions in c - monovariant were considered in Ref. 16. However these theories cover only the case of isotropic substrates. Beside that, the complexity of the mathematical treatment for the general case obscures the analysis in application to experimental observations. In this context a specialized theory for domain patterns having narrow inclusions of one domain type into the matrix of the other dominant one is of interest – which is the topic of this chapter.

In this chapter, theoretical description for narrow domain inclusions into dominant variant is developed. The existing theory [14, 16] is generalized for the case of anisotropic substrates and introduce simplifications related to the narrowness of the inclusions, which allows obtaining explicit expressions for their width and period. The chapter is organized as follows. In section 6.1, fictitious dislocation approach is introduced, and stress fields around a narrow inclusion is derived. Section 6.2 is devoted to energetics of narrow a-domain inclusions. In section 6.3 the minimal and equilibrium widths of an individual narrow inclusion are derived. In section 6.4 the interaction between the narrow inclusions is considered, their widths and period are derived in a sparse pattern.

6.1 Stress fields around narrow a-domain inclusions from fictitious dislocation method

Consider a cubic-to-tetragonal ferroelectric thin film on isotropic (cubic) or anisotropic (orthorhombic) substrate. The unit cell of the substrate in the plane of the film has rectangular shape with the lengths a_{s1} and a_{s2} ($a_{s1} = a_{s2}$ for cubic substrates). The dimensions of the unit cell of the free standing material of the film are $a \times a \times c$. We will be interested in the case where $c > a_{s1} \geq a_{s2} > a$, and will specifically consider a sample with narrow a-domain inclusions into c -monovariant. As it is customarily done (see, e.g., Ref. 16), the following conventional assumptions are made.

(i) the medium is assumed to be elastically isotropic, which is a justifiable approximation, e. g., for perovskites in view of small anisotropy of elastic compliance and small variation of elastic parameters from the substrate to the thin film.

(ii) the absolute value of the polarization inside domains is equal to the spontaneous

6.1. Stress fields around narrow a-domain inclusions from fictitious dislocation method

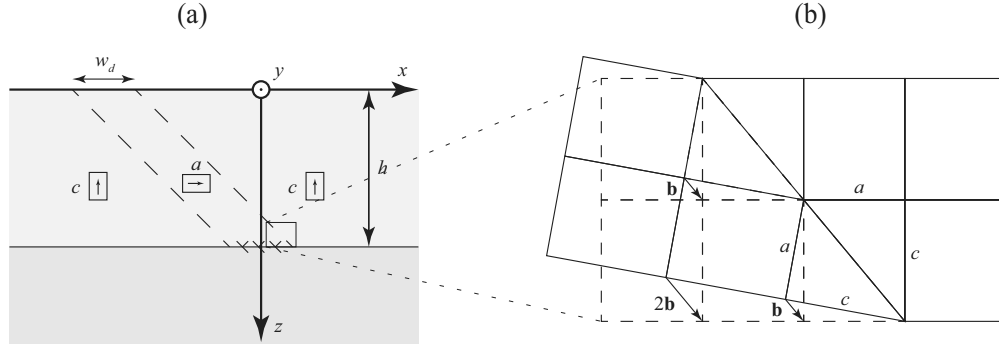


Figure 6.1: Geometry of the problem and its representation in terms of fictitious dislocations. (a)- Ferroelastic thin film ($0 < z < h$) on a substrate ($z > h$), (b) – Magnified area showing Burgers vector per unit cell $\mathbf{b} = (c - a)\{1, 0, 1\}$.

polarization value P_s in a free-standing film and its variation caused by strains is negligible. This assumption, justified for typical perovskite ferroelectric films far from transition to their parent phase [20], allows considering only the elastic sub-problem.

(iii) Domain walls of the inclusion are mechanically compatible implying that the two domain walls of the inclusion are flat and parallel to each other. As it was shown in Chapter 5, the domain walls, in principle, may deviate off their permissible orientation by small angles. However, incompatibility elastic fields generated by such walls are characterized by negligible magnitudes compared to the film-substrate misfit elastic fields, therefore, the effect of domain wall rotation on the domain structure formation can be neglected.

The relevant parameters for the fictitious dislocation model are: h - film thickness, w_d - a-domain width, $\xi = \frac{w_d}{h}$ - relative domain width, $\epsilon_T = \frac{c-a}{a}$ - tetragonality factor. Besides, relative coherency strains Φ_i in r_1 and r_2 directions are introduced:

$$\Phi_1 = \frac{a_{s1} - a}{c - a}, \quad \Phi_2 = \frac{a_{s2} - a}{c - a}. \quad (6.1)$$

Consider an individual stripe of a-domain in the bulk of c-variant thin film, Fig. 6.1. The total stress $\sigma_{ij}^{(t)}$ in the sample can be presented in the form

$$\sigma_{ij}^{(t)} = \sigma_{ij}^{(c)} + \sigma_{ij}^{(a)}, \quad (6.2)$$

where $\sigma_{ij}^{(c)}$ is the stress field inside an infinite c-monovariant and $\sigma_{ij}^{(a)}$ is the stress field inhomogeneity due to an a-domain inclusion. The latter can be calculated as a stress field generated by an a-domain inclusion embedded into the matrix with lattice constants of the

Chapter 6. Narrow ferroelastic domains and their sparse patterns in tetragonal ferroelectric thin films

c-monovariant everywhere (in the film and in the substrate).

In the c-monovariant the mechanical state of the film corresponds to that of a strained plate with deformations $\epsilon_{11} = \Phi_1 \frac{c-a}{a}$, $\epsilon_{22} = \Phi_2 \frac{c-a}{a}$, $\epsilon_{12} = 0$ and with stresses $\sigma_{33} = \sigma_{31} = \sigma_{32} = 0$ (hereafter $c - a \ll a$ is used which implies $\frac{c-a}{c} \approx \frac{c-a}{a}$). According to the Young's law the plate will have only two nonzero stress components:

$$\sigma_{11}^{(c)} = \frac{E\alpha(\Phi_1 + \Phi_2\nu)H(h-z)}{1-\nu^2}, \quad (6.3)$$

$$\sigma_{22}^{(c)} = \frac{E\alpha(\Phi_2 + \Phi_1\nu)H(h-z)}{1-\nu^2}, \quad (6.4)$$

where E is Young's modulus, ν is Poisson ratio, $H(h-z)$ is the Heaviside function, which is 1 if $z < h$ and 0 if $z \geq h$. Relationships (6.3) and (6.4) are valid for the conventional case of a hard thick substrate.

The expression for $\sigma_{ij}^{(a)}$ may be found using fictitious dislocation model, see Fig. 6.1. For the fictitious dislocation model assumption (iii) implies that fictitious lattice defects are located only at the interface between the film and the substrate [16]. The Burgers vector of the dislocations corresponds to the displacement, caused by the transition of the inclusion from c-state to a-state, see Fig. 6.1, (b). One finds that the system is equivalent to that containing fictitious dislocations with Burgers vector $\mathbf{b} = (c-a)\{1, 0, 1\}$ in each unit cell on the substrate-film interface, which corresponds to density $\rho(x) = (c-a)/a = \epsilon_T$ of edge dislocations with Burgers vector $\{1, 0, 1\}$. Thus elastic field of the dislocation ensemble may be readily presented in the form

$$\sigma_{ij}^{(a)} = \int_{-w_d/2}^{w_d/2} \sigma_{ij}^{(ED)}(x-\chi, z) \rho(\chi) d\chi, \quad (6.5)$$

$$\rho(\chi) = \epsilon_T. \quad (6.6)$$

Here $\sigma_{ij}^{(ED)}(x, z)$ is the elastic field around edge dislocation having Burgers vector $\{1, 0, 1\}$ and located in the point $\{0, 0, h\}$ in the semi-infinite isotropic medium. It consists of three contributions, calculated by Head [47]:

$$\sigma_{ij}^{(ED)}(\vec{r}) = \sigma_{ij}^{(1)}(\vec{r}) + \sigma_{ij}^{(2)}(\vec{r}) + \sigma_{ij}^{(3)}(\vec{r}). \quad (6.7)$$

Here $\vec{r} = \{x, z\}$, $\sigma_{ij}^{(1)}$ describes elastic field from dislocation itself (as if it were in the bulk). $\sigma_{ij}^{(2)}$ is elastic field from its image with burgers vector $\{-1, 0, -1\}$ located in $\{0, 0, -h\}$. Further, additional stress $\sigma_{ij}^{(3)}$ is introduced as to satisfy mechanically free boundary conditions at the

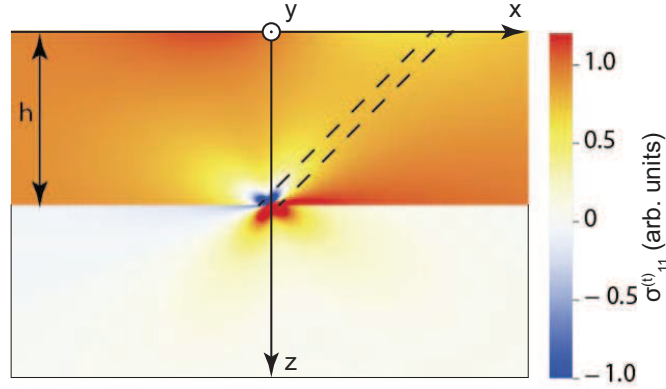


Figure 6.2: The distribution of the in-plane stress $\sigma_{11}^{(t)}$ in the XZ cross-section of the sample. Domain width to film thickness ratio $\xi = 0.12$

free surface $z = 0$:

$$\sigma_{33}^{(ED)}(x, 0) = \sigma_{13}^{(ED)}(x, 0) = 0. \quad (6.8)$$

Explicit expressions for the stress components of $\sigma_{ij}^{(ED)}$ are given in Appendix A. As an illustration, the distribution of the resulting in-plane stress $\sigma_{11}^{(t)}$ in the XZ cross-section of the sample containing a narrow a-domain inclusion into c-monovariant is shown in Fig. 6.2.

6.2 Energetics of narrow a-domain inclusions

For the case of isotropic substrate ($a_{s1} = a_{s2}$), the energetics of individual a-domain-stripe inclusions into c-monovariant film was studied in Ref. 16. As the output of this theory elastic energy of a-domain inclusion relative to the c-monovariant (per unit length in Y-direction) was found in the form

$$U = \frac{h^2 E \epsilon_T^2 (-2\pi\Phi(1+\nu)\xi + 2\xi \arctan[\frac{\xi}{2}] + \frac{1}{4}\xi^2 \ln[1 + \frac{4}{\xi^2}] - 2\ln[1 + \frac{\xi^2}{4}])}{2\pi(1-\nu^2)}. \quad (6.9)$$

Here $\Phi = \Phi_1 = \Phi_2$ (see Eq. (6.1)). As it is expected, the a-domain inclusions with all four possible orientations in this case are energetically equivalent: in addition to (101) orientation of the inclusion shown in Fig. 6.1 and (10 $\bar{1}$) orientation of the inclusion, both described by fictitious dislocation with line along Y-axis, there are two more possible orientations of the inclusions: (110) and (1 $\bar{1}$ 0) which correspond to fictitious dislocation along the X-axis.

The anisotropy of the substrate is expected to make a distinction between the a-domain

Chapter 6. Narrow ferroelastic domains and their sparse patterns in tetragonal ferroelectric thin films

inclusions into "easy" ones, $(10\bar{1})$ and (101) , with polarization vector along the axis with longer substrate unit-cell a_{s1} and "hard" ones - $(1\bar{1}0)$ and (110) . To incorporate this new feature the theory developed in Refs. 14, 16 is generalized to cover the case of anisotropic substrate. Below "easy" domains ($(10\bar{1})$ and (101)) are considered. The result for the "hard" domains may be then obtained by interchanging a_{s1} and a_{s2} lattice constants in the expressions for "easy" domains.

The elastic energy excess over that of the c-monovariant may be calculated as (see Eq. (6.2)):

$$U_a = \frac{1}{2} \int_0^\infty \int_{-\infty}^\infty s_{ijkl} (\sigma_{ij}^{(t)} \sigma_{kl}^{(t)} - \sigma_{ij}^{(c)} \sigma_{kl}^{(c)}) dx dz. \quad (6.10)$$

Here s_{ijkl} is the compliance tensor. Using Eq. (6.2), the energy U_a can be presented as the sum

$$U_a = U_{ac} + U_{aa} \quad (6.11)$$

of the energy related to the stress release (interaction of the inclusion with the stress from the c-monovariant)

$$U_{ac} = \int_0^\infty \int_{-\infty}^\infty s_{ijkl} (\sigma_{ij}^{(a)} \sigma_{kl}^{(c)}) dx dz, \quad (6.12)$$

and the energy penalty related to the inclusion's self-energy

$$U_{aa} = \frac{1}{2} \int_0^\infty \int_{-\infty}^\infty s_{ijkl} (\sigma_{ij}^{(a)} \sigma_{kl}^{(a)}) dx dz. \quad (6.13)$$

It is known that the energy of elastic fields generated by dislocations can be equivalently represented as the energy of interaction between dislocations (see, e.g., [13]). Using this representation, the energy penalty U_{aa} can be rewritten as

$$U_{aa} = \frac{h^2}{2} \int_0^\xi \int_0^\xi E_{\text{disl}}^{(1)}(e_T; \tilde{x}_1 - \tilde{x}_2) d\tilde{x}_1 d\tilde{x}_2, \quad (6.14)$$

where $E_{\text{disl}}^{(1)}(q; \tilde{r})$ is the energy of interaction between two edge dislocations located at distance h from the free surface and at distance $r = \tilde{r}h$ from each other, both having Burgers vectors $q\{1, 0, 1\}$. For the derivation of $E_{\text{disl}}^{(1)}(q; \tilde{r})$ see Appendix B, where its explicit form is given, Eq. (6.51).

The contributions U_{ac} and U_{aa} are calculated to obtain:

$$U_{ac} = \frac{-h^2 E \epsilon_T^2 (\Phi_1 + \Phi_2 \nu) \xi}{1 - \nu^2}, \quad (6.15)$$

$$U_{aa} = \frac{h^2 E \epsilon_T^2 g(\xi)}{(1 - \nu^2)}, \quad (6.16)$$

$$g(\xi) = \frac{1}{\pi} \left(\xi \arctan\left[\frac{\xi}{2}\right] + \frac{1}{8} \xi^2 \ln\left[1 + \frac{4}{\xi^2}\right] - \ln\left[1 + \frac{\xi^2}{4}\right] \right). \quad (6.17)$$

One readily checks that in case $\Phi_1 = \Phi_2$ the results (6.11) , (6.15)-(6.17) are consistent with the result from Ref. 16 given by Eq. (6.9).

Further, following Ref. 12, the theory is extended by including a contribution to the energy, associated with domain walls

$$U_w = 2\sqrt{2}\lambda h \quad (6.18)$$

in the energy balance. Here λ is the energy density per unit area of the domain wall (DW), the coefficient $2\sqrt{2}$ comes from presence of 2 DWs in each inclination and their inclination of 45 degrees. In contrast to the elastic energy, Eqs. (6.15) and (6.16), which scales as a square of film thickness, DW energy, Eq. (6.18) increases linearly with h . This makes DWs relatively more costly in thinner films. One obtains for "easy" domains:

$$U_1 = U_a + U_w = \frac{h^2 E \epsilon_T^2 (- (\Phi_1 + \Phi_2 \nu) \xi + g(\xi))}{1 - \nu^2} + 2\sqrt{2}\lambda h. \quad (6.19)$$

Expression (6.19) can be cast in a form convenient for further analysis:

$$U_1 = \frac{h^2 E \epsilon_T^2 (-\gamma \xi + g(\xi) + 0.46 h_0 / h)}{1 - \nu^2}, \quad (6.20)$$

$$\gamma = \Phi_1 + \Phi_2 \nu, \quad (6.21)$$

$$h_0 = 6.1 \frac{\lambda(1 - \nu^2)}{E \epsilon_T^2}. \quad (6.22)$$

Here the γ parameter is introduced (hereafter called coherency factor) which characterizes the stress state of the film and takes into account anisotropy of the substrate. Also, here length scale h_0 is used, which was coined by Roytburd [70] for the description of the a/c patterns in ferroelectric thin films. For typical perovskites like PZT, h_0 is of the order of 1 nm. In Eq. (6.20) the function $g(\xi)$ is given by expression (6.17). In the interval of the a-domain width

Chapter 6. Narrow ferroelastic domains and their sparse patterns in tetragonal ferroelectric thin films

$0.02 < \xi < 0.5$, the function $g(\xi)$ may be fitted with 6% error margin by expression

$$g(\xi) \approx 0.17\xi^{7/4}. \quad (6.23)$$

6.3 Equilibrium and minimal a-domain widths

6.3.1 Equilibrium domain width

Equilibrium width of the a-domain inclusion may be found from minimization of its energy (6.19) with respect to ξ . One readily obtains

$$w_d = hG(\gamma), \quad (6.24)$$

where $G = (g')^{-1}$ is the inverse of the derivative of the function g . An important conclusion may be drawn that under constant mismatch, domain width scales linearly with film thickness. However we should recall that this result is obtained for an individual inclusion, while density of inclusions may increase with increase of film thickness, resulting in a correction to this linear law; this issue will be addressed in section 6.4.

Using approximate relationship Eq. (6.23) and Eq. (6.24) one obtains for the equilibrium normalized domain width

$$\xi = 5\gamma^{4/3}. \quad (6.25)$$

From expression (6.25) it is seen that equilibrium domain width is controlled by the coherency factor γ . The dependence of the domain width on the coherency factor is plotted in Fig. 6.3.

As one can see from this plot, the a-domain inclusion is expected to be narrower than a half of film thickness (implying the applicability of the approximate relationships (6.23) and (6.25) with 6% error margin) in case where the γ -parameter does not exceed 0.18. Such situation may happen when the film fits almost perfectly on the substrate, or when a major portion of the misfit strain is released by other mechanisms than domain formation (e.g. misfit dislocations).

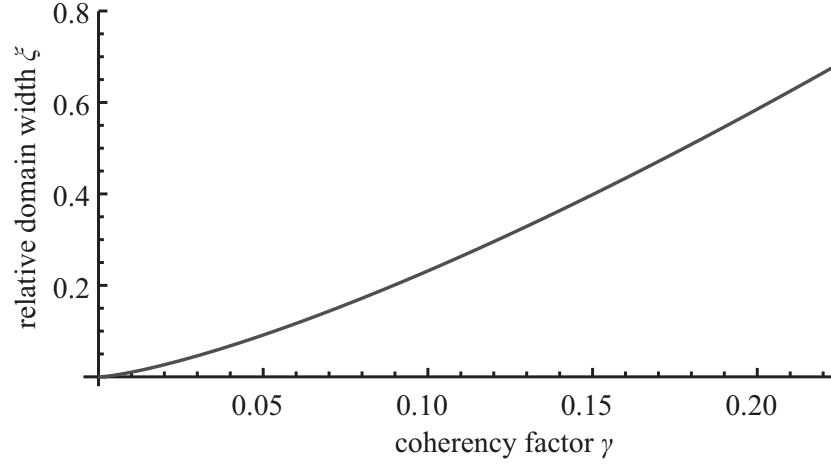


Figure 6.3: Dependence of the a-domain width to film thickness ratio ξ on the coherency factor γ .

6.3.2 Minimal domain width

In spite of the fact that domain wall energy is commensurate with other energies, it does not depend on the a-domain width, which explains that the above results on the equilibrium domain width are independent of domain wall energies¹. Nevertheless, taking into account domain wall energy has an important consequence.

Combining (6.25) with (6.20), one obtains expression for the energy of the equilibrium inclusion

$$\Delta U = \frac{h^2 E \epsilon_T^2}{1 - \nu^2} \left(0.46 \frac{h_0}{h} - 2.16 \gamma^{7/3} \right). \quad (6.26)$$

The formation of the a-domain will occur only if its energy excess over the c-monovariant is negative, which means $\Delta U < 0$. This requirement can be formulated as

$$h > h_{\text{cr}} = 0.21 h_0 \gamma^{-7/3}. \quad (6.27)$$

Thus formation of a-domain inclusions is expected only if the film thickness exceeds a critical value for which the power law, Eq. (6.27), is found in terms of mismatch factor γ . For

¹In principle, U_w may depend on w if the interaction between the opposite domain walls of the inclusion is taken into account. However we assume such interaction to be negligible

Chapter 6. Narrow ferroelastic domains and their sparse patterns in tetragonal ferroelectric thin films

films with sub-critical thickness c-monovariant is the lowest-energy state.

6.4 Interaction between a-domain inclusions, equilibrium 1D pattern

A system with multiple inclusions can be described using the same approach. Consider a parallel-stripe pattern of a-domain inclusions into the c-monovariant containing n "easy" a-domains, ((101) or (10-1)), all having width w_d .

Mean energy of such system (excess over c-monovariant) per unit area is given by the sum

$$U = \frac{nU_1 + U_{\text{int}}}{L}. \quad (6.28)$$

where U_1 is coming from expressions (6.20) - (6.22), L is the length of the sample in X -direction. Energy U_{int} of all interactions between different a-domain inclusions may be presented as a sum of interaction energies of each pair of domains:

$$U_{\text{int}} = \frac{1}{2} \sum_{i=1}^n \sum_{j=1}^n u_{\text{int}}(x_i - x_j), \quad i \neq j, \quad (6.29)$$

where x_i is the x -coordinate of the i^{th} domain, $u_{\text{int}}(r)$ is the energy of interaction of two a-domains with distance r between them.

Depending on the inclination of each individual domain in the interacting pair, there are three distinct cases possible: bottom-to-top, top-to-top², and bottom-to-bottom, which are illustrated in Fig. 6.4. We will be interested in the situation where $r \gg w_d$ for which an approximation is justified where each domain is represented by a single fictitious dislocation under it with Burgers vector $\epsilon_T w_d \{1, 0, \pm 1\}$. In case of bottom-to-top pair, the energy of interaction may be calculated as

$$u_{\text{int}}^{(\parallel)}(r) = E_{\text{disl}}^{(1)} \left(\epsilon_T w_d; \frac{r}{h} \right), \quad (6.30)$$

where $E_{\text{disl}}^{(1)}(q; \tilde{r})$ is the energy of interaction between two edge dislocations with parallel Burgers vectors, expression of which is given in Appendix B, Eq. (6.51). In the two other cases

$$u_{\text{int}}^{(V),(\Lambda)}(r) = E_{\text{disl}}^{(2)} \left(\epsilon_T w_d; \pm \frac{r}{h} \right), \quad (6.31)$$

²We do not discuss interaction of the domains for the case $r < 2h$, where overlapping of a -domains exists.

6.4. Interaction between a-domain inclusions, equilibrium 1D pattern

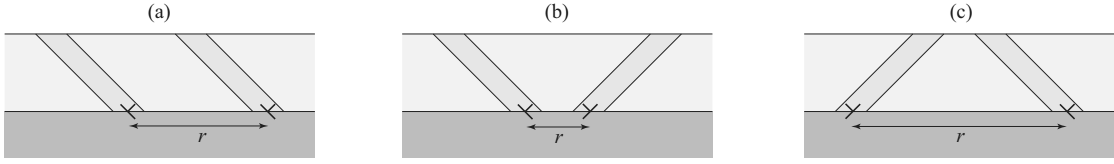


Figure 6.4: Possible domain orientations in the interacting domain pair: (a) – top-to-bottom; (b)– bottom-to-bottom; (c) – top-to-top, and their representation by fictitious dislocations.

where $E_{disl}^{(2)}(q; \bar{r})$ is given by Eq. (6.52).

Using Eqs. (6.29)-(6.31), one may readily calculate energy for an arbitrary sparse³ pattern.

For the long-range interaction, in case where $h/r \ll 1$, using this smallness in Eqs. (6.30) and (6.31), one readily obtains that interaction energy has the same long-range asymptote for all the three cases, which is

$$u_{int}(r) = E\epsilon_T^2 w_d^2 \frac{2h^2}{\pi r^2}. \quad (6.32)$$

Hereafter we will be interested in equally spaced sparse pattern, where all distances between the neighboring stripes are $l = L/n$ and $l \gg h$. In such case the energy of interaction between i^{th} and j^{th} stripes becomes

$$u_{int}(l) = \frac{2}{\pi(1-\nu^2)} E\epsilon_T^2 w_d^2 h^2 / (l(i-j))^2 \quad (6.33)$$

and that of all pairs U_{int} calculated using (6.29) is

$$U_{int} = \frac{\pi}{3(1-\nu^2)} LE\epsilon_T^2 w_d^2 h^2 / l^3. \quad (6.34)$$

The total mean energy per unit area together with other contributions (6.28) becomes

$$U = \frac{\epsilon_T h^2 E(-\gamma\xi + g(\xi) + \frac{\pi h^2 \xi^2}{3l^2} + 0.46 \frac{h_0}{h})}{l(1-\nu^2)}, \quad (6.35)$$

where $g(\xi)$ is the function defined in Eq. (6.17).

For the case of narrow a-domain, $w_d < h/2$, the approximation (6.23) is used on function $g(\xi)$. Minimization of Eq. (6.35) with respect to l and ξ and following simplification of the

³where distances between each pair of inclusions is much larger than film thickness

Chapter 6. Narrow ferroelastic domains and their sparse patterns in tetragonal ferroelectric thin films

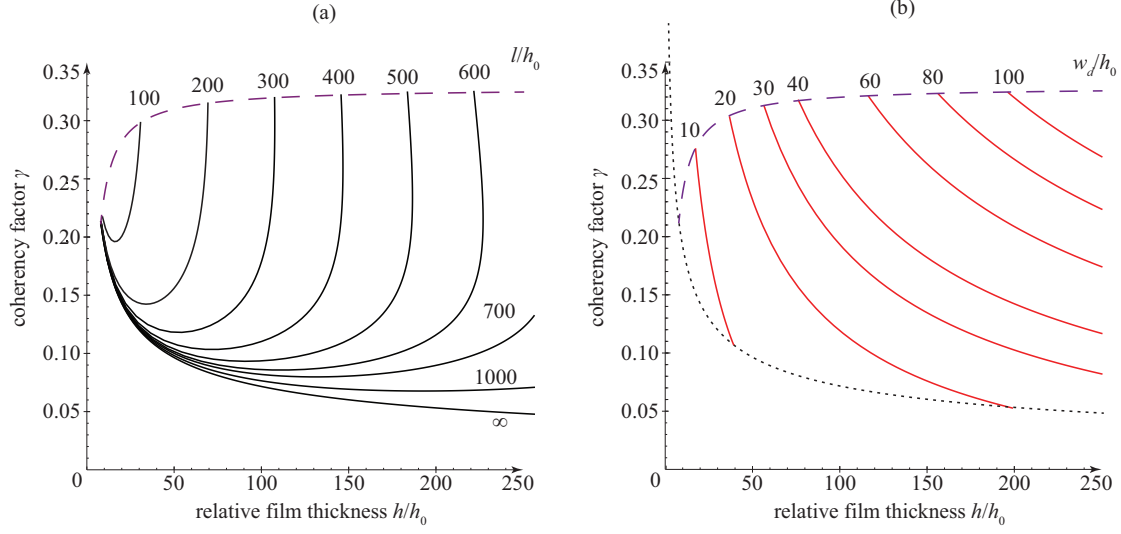


Figure 6.5: Diagrams for 1D domain pattern control in terms of the film thickness h and the coherency factor γ . (a) The solid curves correspond to a constant period of the pattern; the numbers at the curves give the period measured in h_0 units. (b) The solid curves correspond to a constant width of the a-domains w_d ; the numbers at the curves give the domain width w_d in h_0 units. The upper dashed curves show the limit of the applicability of the approximation used in the calculation, $w_d/h < 1/2$. The area in (b) below the dotted curve corresponds to the c-monovariant.

system of equations leads to:

$$l^2 = \frac{\pi h^2 \xi^2}{-1.38 \frac{h_0}{h} + 0.3825 \xi^{7/4}}, \quad (6.36)$$

$$\gamma \xi = 0.5525 \xi^{7/4} - 0.92 \frac{h_0}{h}. \quad (6.37)$$

Numerical solution for the set of Eqs. (6.36) and (6.37) is illustrated in Fig 6.5, where domain periodicity l (a) and width $w_d = h\xi$ (b) are plotted in the axes of the film thickness h and coherency factor γ (all lengths are in units h_0). One can note that the domain period diverges on approaching the critical thickness $h_{cr} \approx 0.21 h_0 \gamma^{-7/3}$. (Eq. (6.27)) corresponding to the dotted line in Fig 6.5(b).

In summary, the geometrical parameters of the 1D lamellar pattern, the width $w_d = h\xi$ and period l of the a-domains are controlled by the film thickness h and two material-related parameters: the length scale h_0 which is a property of the ferroelectric (Eq. (6.22)) and the coherency factor γ which characterizes the stress state of the film and can be presented in the

form (see Eq. (6.21))

$$\gamma = \frac{a_{s1} + \nu a_{s2} - (1 + \nu)a}{c - a} \quad (6.38)$$

where a and c are the lattice constants of the film in directions perpendicular to and along the polarisation vector, while a_{s1} and a_{s2} are that of the substrate in directions perpendicular to and along the a-domain stripe respectively.

6.5 New periodicity scaling law

This section discusses the dependence of periodicity of domain structure on the film thickness. For a fixed coherency factor γ , the typical dependence $l(h)$ obtained from Eqs. (6.36) and (6.37) is shown in Fig. 6.6. It is of interest to note that in thick films the dependence of the domain period on the film thickness attains the linear form, which opposes the Kittel-like square root law which is conventionally used for description of domain structures. This behaviour follows directly from Eqs. (6.36) and (6.37) once one solves them in approximation $h_0/h \ll 1$. Keeping only terms (h_0/h) of the first order of smallness, one can obtain:

$$w_d \approx w_0 + 2.22\gamma^{4/3}h, \quad w_0 = 1.22h_0/\gamma, \quad (6.39)$$

$$l \approx l_0 + 3.17\gamma^{1/6}h, \quad l_0 = 1.642h_0\gamma^{-13/6}. \quad (6.40)$$

The linear dependence $l(h)$ described by Eq. (6.40) is shown in Fig. 6.6 by the dashed line.

It is possible to draw simple considerations that can explain why the domain structures in the considered system do not follow the Kittel's square-root law of periodicity. One can say that the square-root law is the characteristic feature of dense domain patterns and typically is the result of competition of energy of the domain walls (U_W in Fig. 2.2) with, in case of ferroelastic domain structures, the energy of microstresses (U_{mic} in Fig. 2.2), which change with opposite signs with variation of the domain size. It is possible to show (see, e.g., Chapter 4) that with increase of the film thickness h and with conservation of all proportions between the lengths in the system (such as (l/h) , (w_d/h) , etc.), the elastic energy of the structure scales as h^2 , while the self-energy of a domain wall scales as h . As a consequence, in the limit of thick films $h \rightarrow \infty$, the energy of domain walls can be neglected, and the period of domain structure is defined by the condition of minimal elastic energy. In typical dense patterns, the minimal elastic energy of the structure is characterized by the infinitesimally small domain period; thus, at $h \rightarrow \infty$ where energy of domain walls is neglected, $w_d/h \rightarrow 0$. Further investigation of

Chapter 6. Narrow ferroelastic domains and their sparse patterns in tetragonal ferroelectric thin films

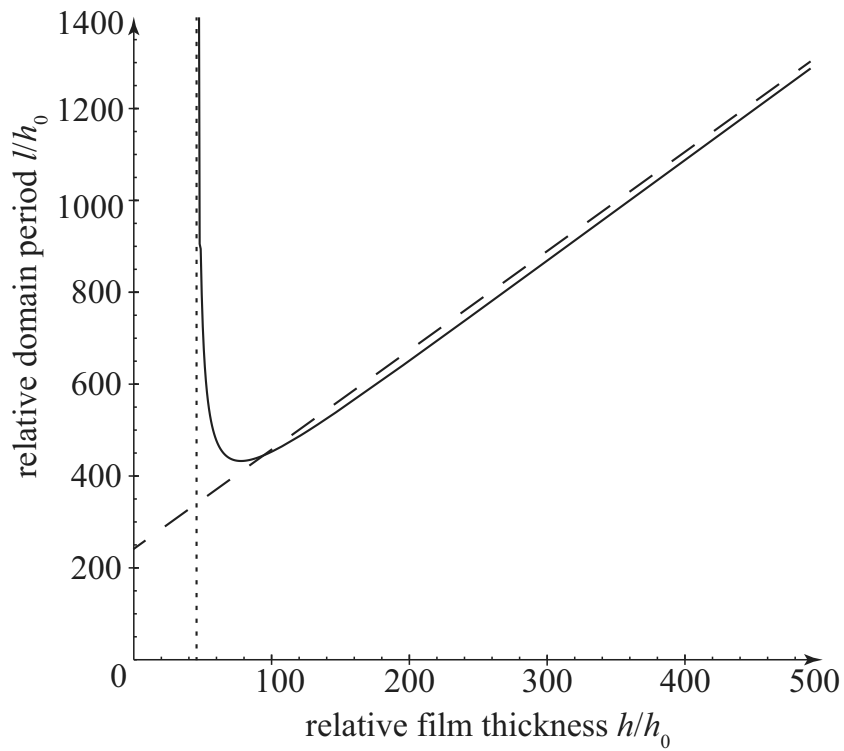


Figure 6.6: Period of the domain structure of narrow a -domain inclusion to c -monovariant vs the thickness of the film, plotted for coherency factor $\gamma = 0.1$. All lengths are shown in units of the characteristic length h_0 . The dashed line shows the linear scaling law of the periodicity of the structure in thick films, described by Eq. (6.40). The dotted line represents the critical thickness h_{cr} below which c -monovariant is formed instead of a/c -domain structure.

the asymptotical behaviour of (w_d/h) at large film thicknesses taking into account domain wall self-energies gives $w_d/h \propto h^{-1/2}$, or, more conventionally, Kittel-like $w_d \propto \sqrt{h}$.

In sharp contrast, in the structure considered in this chapter, the minimal elastic energy is reached at *non-zero* values of (w_d/h) and (l/h) . This section does not discuss the reasons of preference of sparse domain structures over dense structures; nevertheless, one can see that when in the limit of thick films ($h \rightarrow \infty$) sparse domain structures are formed, lengths corresponding to the minimal energy of the system should have linear dependence on the film thickness – as confirmed by Eqs. (6.36) and (6.37).

As another feature of the solution (Eqs. (6.36) and (6.37)), one can see from Fig. 6.6 that, with decreasing the film thickness, the distance between *a*-domain inclusions increases to values $l \gg h$. In this case, interaction between *a*-domains can be neglected, and the conclusions made in Chapter 6.3 are applicable to this case: below the critical thickness h_{cr} , described by Eq. (6.27), *c*-domain monovariant forms instead of the *a/c*-structure. As a consequence, the dependence $l(h)$ diverges when the film thickness decreases approaching to $h \rightarrow h_{cr}$, which is seen in Fig. 6.6.

6.6 Comparison with experiment

The above theoretical results allow predicting domain width and periodicity in (100)-oriented tetragonal ferroelectric thin films if the lattice constants of the film and that of the substrate are known. Importantly, the use of the actual lattice constants of the film (in a free standing form), is required which often differ from the standard lattice parameters of the material [71]. Here a method is described, suggested and implemented by P. Yudin, of recalculation of the free-standing film's lattice constants using X-ray diffraction (XRD) data for the film on the substrate. Then this method is applied using example of $\text{Pb}(\text{Zr,Ti})\text{O}_3$ (PZT) on Dysprosium Scandate (DSO) substrate to match experimental data of Ref. 64 with the theory.

6.6.1 Lattice constants of free - standing film

It is known that thin films may have different stoichiometry than the bulk material and, as a consequence, different lattice constants. This effect was particularly identified for pulsed laser deposition (PLD) method, where the lattice constants of the grown films were often appreciably different from those, expected from the target. For example, for STO films grown on STO substrates, where a perfect match is expected, there was still a mismatch of some 1%

Chapter 6. Narrow ferroelastic domains and their sparse patterns in tetragonal ferroelectric thin films

[71]. Customarily, theoretical description of the film's parameters (e.g. width of a-domains in c/a/c structure) is done using lattice constants a_{ref} and c_{ref} known from literature for the corresponding bulk material (hereafter the reference lattice constants). Meanwhile, the "true" lattice constants entering the theoretical expressions are that of a free-standing film a and c . Here a method of recalculation of the "true" film's lattice constants using XRD data and the reference lattice constants is provided. This recalculation is of particular importance for the case of the narrow domain inclusions which are very sensitive to the mismatch between the film and the substrate.

Consider a ferroelectric material in a free standing (stress free) state. For both the thin film and the reference bulk material, the a and c lattice constants may be calculated using equations (see e.g. Ref. 20):

$$\begin{aligned} c &= a_c(1 + \epsilon_{s_{11}}) \\ a &= a_c(1 + \epsilon_{s_{12}}) \end{aligned} \quad (6.41)$$

where a_c is the material's cubic lattice constant (with temperature dependance extrapolated from the cubic phase), $\epsilon_{s_{ij}} = Q_{ij}P_s^2$ are spontaneous strains, written in terms of electrostrictive constants Q_{ij} and spontaneous polarization P_s . To trace the source of difference in lattice constants driven by non-stoichiometry, consider the relative variation of the lattice constants $\delta a = a - a_{ref}$ and $\delta c = c - c_{ref}$, which may be derived using (6.41) to obtain

$$\begin{aligned} \frac{\delta c}{c} &\approx \frac{\delta a_c}{a_c} + \frac{\delta \epsilon_{s_{11}}}{\epsilon_{s_{11}}} \frac{\epsilon_{s_{11}}}{1 + \epsilon_{s_{11}}} \approx \frac{\delta a_c}{a_c}, \\ \frac{\delta a}{a} &\approx \frac{\delta a_c}{a_c} + \frac{\delta \epsilon_{s_{12}}}{\epsilon_{s_{12}}} \frac{\epsilon_{s_{12}}}{1 + \epsilon_{s_{12}}} \approx \frac{\delta a_c}{a_c}. \end{aligned} \quad (6.42)$$

As controlled by Eq. (6.42) there are two contributions to the non-stoichiometry-driven shift of the lattice constant: the first one related to the shift of the cubic lattice constant and the second related to the shift of the spontaneous strain. As stated above, the expected relative shift of the cubic lattice constant $\frac{\delta a_c}{a_c}$ is of the order of 1%. In view of smallness of spontaneous strain, $\epsilon_s \approx 1\%$, the second contribution contains a small factor $\frac{\epsilon_s}{1 + \epsilon_s}$. To compete with the shift of the cubic lattice constant the variation of the spontaneous strain must be of the order of 100%, which does not seem to be realistic. This justifies the second approximate equality in Eq. (6.42). Thus the shift of the lattice constants is mainly due to the correction in the cubic lattice constant, caused by non-stoichiometry of the film, while the impacts of the changes in spontaneous polarization and electrostrictive coefficients are expected to be negligible. All in

all, one obtains

$$\frac{c - c_{ref}}{c} \approx \frac{a - a_{ref}}{a} \approx \frac{\delta a_c}{a_c} \equiv \Delta. \quad (6.43)$$

In a thin film on a substrate, containing $c/a/c$ pattern, lattice constants vary with position in the film. From XRD measurements one can extract lattice constants a_m and c_m corresponding to the peaks for c -domains. Here an approximation is used where the two a_m lattice constants are equal in the two in-plane directions, which is justified for weakly anisotropic substrate and sparse $c/a/c$ pattern. Mechanically free condition in the out-of-plane direction for the film yields

$$\sigma_{33} = \frac{E}{(1+\nu)(1-2\nu)} \left[2\nu \left(\frac{a_m - a}{a} \right) + (1-\nu) \left(\frac{c_m - c}{c} \right) \right] = 0 \quad (6.44)$$

Using Eq. (6.43), Eq. (6.44) may be presented in the form

$$2\nu(\alpha_m - \Delta) + (1-\nu)(\kappa_m - \Delta) = 0, \quad (6.45)$$

$$\alpha_m = \frac{a_m - a_{ref}}{a} \approx \frac{a_m - a_{ref}}{a_{ref}}, \quad (6.46)$$

$$\kappa_m = \frac{c_m - c_{ref}}{c} \approx \frac{c_m - c_{ref}}{c_{ref}}. \quad (6.47)$$

Expression Eq. (6.45) is readily solved with respect to Δ to obtain

$$\Delta = \frac{(1-\nu)\kappa_m + 2\nu\alpha_m}{1+\nu} = 0.54 \frac{c_m - c_{ref}}{c_{ref}} + 0.46 \frac{a_m - a_{ref}}{a_{ref}}, \quad (6.48)$$

where typical value for the Poisson ratio $\nu = 0.3$ is used. Using Eq. (6.48) and the results of XRD lattice constant measurements a_m and c_m , one may readily calculate the shift of the actual film's lattice constants a and c with respect to the reference lattice constants a_{ref} and c_{ref} , known e. g. for ceramics.

Expression (6.48) is suitable for the correction of γ -factor via Eq. (6.38). For $\nu = 0.3$ one obtains

$$\gamma = \left(\frac{a_{s1} + 0.3a_{s2} - 1.3a_{ref}(1+\Delta)}{(c_{ref} - a_{ref})(1+\Delta)} \right). \quad (6.49)$$

Chapter 6. Narrow ferroelastic domains and their sparse patterns in tetragonal ferroelectric thin films

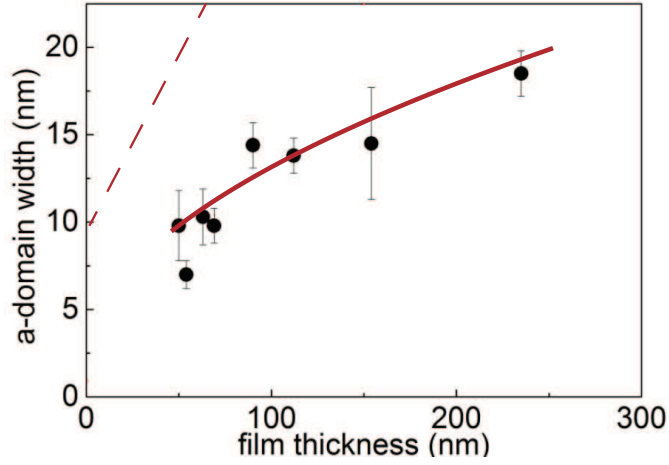


Figure 6.7: Dependence of the domain width on the film thickness. Black rounds - experiment; dotted line - theoretically expected domain width for the film using ceramics lattice constants ($\gamma=0.2$, linear approximation given by Eq. (6.39) is used); solid line - theoretically expected domain width using recalculated lattice constants for the free-standing film ($\gamma=0.015$, Eq. (6.37))

6.6.2 Domain widths for $\text{Pb}(\text{Zr,Ti})\text{O}_3$ on DyScO_3 substrate

Let us apply this approach to $\text{Pb}(\text{Zr}_{0.1},\text{Ti}_{0.9})\text{O}_3$ (PZT) on DyScO_3 (DSO) substrate, the system addressed in Ref. 64. For a number of samples with different film thicknesses ranging from 50 to 250 nm an analysis of domain structures was made. The films were grown using PLD method and domain widths were measured using piezo force microscopy (PFM) and transmission electron microscopy (TEM) imaging techniques. For the case of TEM observations, (010) lamellae were cut out of the samples using mechanical polishing and ion milling, for more details see Ref. 64. The dependence of the domain width on film thickness is shown in Fig. 6.7.

At room temperature in DSO $a_{s1}=0.39505$ nm and $a_{s2}=0.39468$ nm. The calculation using the ceramics room temperature values for lattice constants of PZT (90/10) ($a_{ref} = 0.3914$ nm, $c_{ref} = 0.4138$ nm) leads to $\gamma = 0.2$ and results in the dotted line in Fig. 6.7, which is in a sharp conflict with the observed experimental data. The XRD measurements indicated that the true a and c indeed exceed a_{ref} and c_{ref} . To recalculate the lattice constants the XRD data shown in Fig. 2(d) of Ref. 69 have been used, re-scaled to fit the in-plane lattice constant of the substrate to the corresponding maximum in the reciprocal space. As a result, it was obtained that the value of Δ , within experimental error margins, lies between 0.2% and 1%. In Fig. 6.7, the theoretical dependence of a -domain width on the film thickness is plotted for $\gamma = 0.015$, which corresponds to $\Delta = 0.84\%$, consistent with the experimental data. The values of lattice constants of the film corresponding to this case are: $a_m = 0.39469$ and $c_m = 0.41728$.

It is important to remark that for the recalculated value of $\gamma = 0.015$, the theory developed in this section predicts formation of c -monovariant in the case of the equilibrium domain structure. It follows from Eq. (6.27) that formation of a/c -structures in the film is expected only for thicknesses $h > 5 \mu\text{m}$, which is in strong disagreement with the experimentally obtained $h_{cr} = 50 \text{ nm}$. It is likely that in real PZT films the formation of domain structures has non-equilibrium character, thus, a theoretical description explaining this aspect is needed.

6.7 Conclusions

A specialized theoretical description is provided for narrow domain inclusions into a dominant domain state in ferroelectric films. The case of a tetragonal film on an anisotropic (orthorhombic) substrate is covered. Theoretical predictions demonstrate that for the considered patterns domain periodicity and a -domain width follow the linear scaling at large film thicknesses, lying in contrast with the classical Kittel-like square root dependence traditionally applied to thin films. Essentially, the geometrical parameters of the 1D lamellar pattern are controlled by the film thickness h and two material-related parameters: the length scale h_0 (Eq. (6.22)), which is a property of the ferroelectric, and the coherency factor γ (Eq. (6.21)), which characterizes the stress state of the film. The outputs of the theory are expressions for the domain width w_d and the domain equilibrium periodicity l . The theoretical findings were compared with the experimental data on the domain width.

When applying the theoretical results, one should take into account that lattice constants a and c for a thin film may be substantially different from those known for a bulk material a_{ref} and c_{ref} . The effect is driven by non-stoichiometry and an approximation is justified where the ratio between lattice constants remains the same as for the bulk: $c/a = c_{ref}/a_{ref}$. The approach was developed allowing to obtain the "true" lattice constants of the film using XRD measurement results, and was implemented for fitting of the theoretical curves to experimental data on a -domain width.

Appendix A. Expressions for the stress field around dislocations in a semi-infinite isotropic media

$$\begin{aligned}\sigma_{11}^{(1)} &= \frac{E(-x^3 + 3x^2(-h+z) + x(-h+z)^2 + (-h+z)^3)}{4\pi(x^2 + (-h+z)^2)^2(1-\nu^2)} \\ \sigma_{11}^{(2)} &= -\frac{E(-x^3 + 3x^2(h+z) + x(h+z)^2 + (h+z)^3)}{4\pi(x^2 + (h+z)^2)^2(1-\nu^2)} \\ \sigma_{11}^{(3)} &= -\frac{Eh(x^3(2h+x) + 6(h-x)x^2(h+z) - 6x(h+x)(h+z)^2 + 2(-h+x)(h+z)^3 + (h+z)^4)}{2\pi(x^2 + (h+z)^2)^3(1-\nu^2)} \\ \sigma_{22}^{(1)} &= \frac{\nu E(-h-x+z)}{2\pi(x^2 + (-h+z)^2)(1-\nu^2)} \\ \sigma_{22}^{(2)} &= -\frac{\nu E(h-x+z)}{2\pi(x^2 + (h+z)^2)(1-\nu^2)} \\ \sigma_{22}^{(3)} &= \frac{\nu Eh(-x^2 + 2x(h+z) + (h+z)^2)}{\pi(x^2 + (h+z)^2)^2(1-\nu^2)} \\ \sigma_{33}^{(1)} &= -\frac{E(x^3 + x^2(-h+z) + 3x(-h+z)^2 - (-h+z)^3)}{4\pi(x^2 + (-h+z)^2)^2(1-\nu^2)} \\ \sigma_{33}^{(2)} &= \frac{E(x^3 + x^2(h+z) + 3x(h+z)^2 - (h+z)^3)}{4\pi(x^2 + (h+z)^2)^2(1-\nu^2)} \\ \sigma_{33}^{(3)} &= -\frac{Eh(x^4 + 2x^3z + 6x^2z(h+z) - 6xz(h+z)^2 - (h+z)^3(h+3z))}{2\pi(x^2 + (h+z)^2)^3(1-\nu^2)} \\ \sigma_{13}^{(1)} &= \frac{E(-h-x+z)(-h+x+z)^2}{4\pi(x^2 + (-h+z)^2)^2(1-\nu^2)} \\ \sigma_{13}^{(2)} &= -\frac{E(h-x+z)(h+x+z)^2}{4\pi(x^2 + (h+z)^2)^2(1-\nu^2)} \\ \sigma_{13}^{(3)} &= -\frac{Eh(h+x+z)(x^2(-2h+x) + x(8h+x)(h+z) - (2h+7x)(h+z)^2 + (h+z)^3)}{2\pi(x^2 + (h+z)^2)^3(1-\nu^2)}\end{aligned}$$

Appendix B. Energy of interaction between two dislocations

Consider two edge dislocations with Burgers vectors $\mathbf{b}_1 = \{b_{1,x}, 0, b_{1,z}\}$ and $\mathbf{b}_2 = \{b_{2,x}, 0, b_{2,z}\}$ located in the points $(0, h)$ and (r, h) , respectively. The energy E_{disl} of interaction between them is equivalent to the work exerted when the second dislocation is displaced from the film

surface to the point (r, h) in the elastic field σ_{ij} of the first dislocation:

$$E_{disl} = - \int_0^h p_3(r, z) dz, \quad (6.50)$$

where p_i is the Peach-Koehler force [46] defined as $p_i = e_{ijk} \sigma_{jl} b_{2,l} \tau_k$, e_{ijk} is the Levi-Civita permutation symbol, τ_k is the unit vector in the direction of the dislocation line.

We will be interested in two cases: (i) - $\mathbf{b}_1 = \{q, 0, q\}$ and $\mathbf{b}_2 = \{q, 0, q\}$; (ii) - $\mathbf{b}_1 = \{q, 0, q\}$ and $\mathbf{b}_2 = \{q, 0, -q\}$. In both cases the Peach-Koehler force component p_3 has form $p_3 = q\sigma_{11}^{(ED)} b_{2x} + q\sigma_{13}^{(ED)} b_{2z}$, with expressions for stresses $\sigma_{11}^{(ED)}$, $\sigma_{13}^{(ED)}$ given in Appendix A.

In the case (i) one readily obtains:

$$E_{disl}^{(1)}(q; \tilde{r}) = \frac{Eq^2}{\pi(1-\nu^2)} \left(\frac{\tilde{r}^2 - 4}{(\tilde{r}^2 + 4)^2} + \frac{1}{4} \log\left(1 + \frac{4}{\tilde{r}^2}\right) \right), \quad (6.51)$$

where $\tilde{r} = r/h$.

For the case (ii) the interaction energy becomes:

$$E_{disl}^{(2)}(q; \tilde{r}) = \frac{2Eq^2}{\pi(1-\nu^2)} \frac{\tilde{r}^2 - 2\tilde{r} + 4}{(\tilde{r}^2 + 4)^2}. \quad (6.52)$$

7 Moving antiphase boundaries using an external electric field

The past decade has seen increasing attention paid to the study of domain walls, often due to their tendency to demonstrate properties significantly different from those usually observed in the individual domains. Tagantsev *et al.* [72] predicted the appearance of a ferroelectric instability around 40K in structural domain boundaries called antiphase boundaries (henceforth APBs) of the incipient ferroelectric SrTiO₃. More recently, spontaneous polarization was observed at ambient temperatures in the APBs of antiferroelectric PbZrO₃ [31]. Alongside, twin walls of paraelectric CaTiO₃ [27, 28, 73] and SrTiO₃ [74] were also observed to be polar, the former having a polarization comparable to the bulk spontaneous polarization of BaTiO₃. These observations provide for the possibility of a potential shift from using domains to using domain walls as individual, functional entities. The low dimensionality of domain walls would prove beneficial towards further miniaturization of devices in applications such as information storage. In light of describing domain walls as functional entities, it becomes necessary to analyse the possibility of displacing them. The current study thus investigates the displacive responses from APBs in a SrTiO₃-like material under the influence of an external inhomogeneous electric field.

In contrast to common ferroelectric domain boundaries, which can be displaced using homogeneous electric fields, polar APBs – polar regions in non-polar materials – are only sensitive to the field gradient. Here it is theoretically demonstrated that in thin films of a SrTiO₃-like material an APB may be readily displaced using an atomic force microscopy (AFM) tip with a voltage applied to it. Initially a flat APB is considered whose in-built polarization is aligned normal to the plane of the film. Across this APB, an inhomogeneous electric field is generated by placing an AFM tip in the vicinity of the APB (illustrated in Fig. 7.1), causing its displacement. The value of the displacement is analysed as a function of parameters such as the film thickness

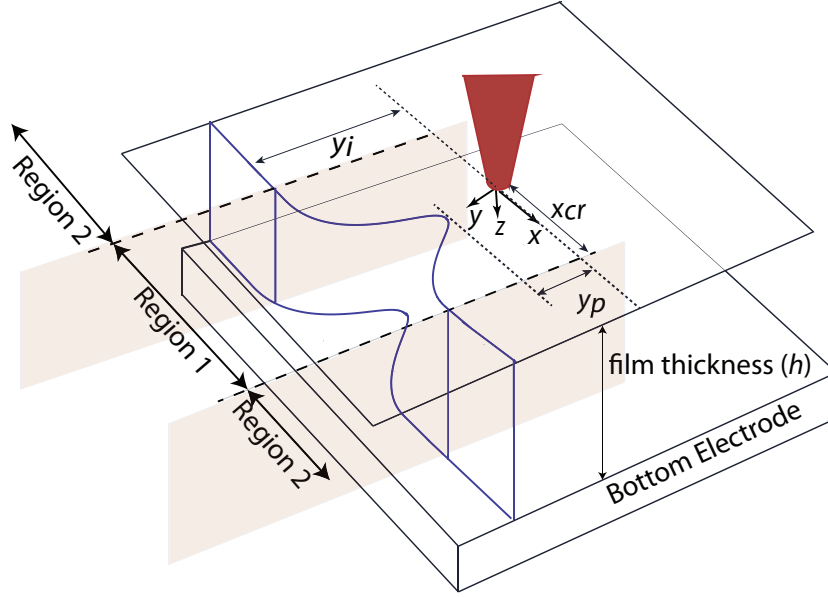


Figure 7.1: Schematic of the problem statement under consideration and its geometry. The AFM tip is initially placed at the distance y_i from a flat wall. The profile of the wall is divided into two regions: Region 1 where the wall is displaced, and Region 2 where the wall remains flat.

and the applied voltage. The residual displacement on the subsequent removal of the applied voltage on the AFM tip is estimated, showing the same order of magnitude as the initial displacement.

7.1 Equilibrium of forces at the antiphase boundary in an electric field

The profile of the displaced wall on the application of the voltage on the AFM tip can be found through the requirement of the equilibrium of forces in each point along the wall. These forces are the electrostatic force p_{el} arising from the interaction of the polarization profile with the inhomogeneous electric field, the mechanical force p_{me} associated with the wall bending and the friction force p_{pe} associated with the pinning of the movable boundary. For the latter the concept of dry friction is applied, meaning that $p_{pe} = \min(p_{pe}^{max}, |p_{el} + p_{me}|)$, where p_{pe}^{max} is the limiting friction force.

At points far away from the AFM tip, where p_{el} is smaller than p_{pe}^{max} , the driving force for the displacement is not large enough to overcome the maximum pinning force and, hence, the

7.1. Equilibrium of forces at the antiphase boundary in an electric field

wall does not displace (region 2 in Fig. 7.1). The equilibrium of forces in this region is given by

$$p_{pe} + p_{el} = 0, \quad p_{me} = 0. \quad (7.1)$$

Conversely, in region 1 from Fig. 7.1 the magnitude of p_{el} is larger than p_{pe}^{max} , causing the wall to displace. The mechanical force p_{me} now obtains a non-zero magnitude owing to a curvature associated with the displaced wall, and the wall is displaced till p_{me} at all points in the final profile is in equilibrium with p_{el} and p_{pe}^{max} . The final state of the wall in region 1 thus satisfies the balance of forces given by

$$p_{el} + p_{me} + p_{pe}^{max} = 0. \quad (7.2)$$

To derive the forces p_{el} and p_{me} , variational principles are used. Following Mokry *et al.* [75], we start from the thermodynamic potential

$$U = \int \lambda dS - \int \vec{E}(x, y, z) \cdot \vec{P}(y - (y_i + \xi(x, z))) dy dS, \quad (7.3)$$

where λ is the surface tension, dS is the element of the wall's surface, $\vec{E}(x, y, z)$ is the spatially varying electric field from the AFM tip, $\vec{P}(y)$ is the polarization profile in the wall centred at $y = 0$, and $\xi(x, z)$ is the wall's displacement away from its initial separation from the AFM tip (y_i). The wall is considered to be isotropic in nature, i.e. the surface tension σ is assumed to be constant for all orientations of the wall. The current model has been developed to obtain a preliminary idea of the behaviour of APBs and hence is limited to a linear interaction between the polarisation profile and the field gradient. Though the higher order contributions such as the dependence of the polarisation profile on the electrical field [76] or the interaction between the field gradient with the dielectric susceptibility [77] might be significant, these are not considered for this first-approximation study. Similarly, the dependence of the polarisation profile on wall bending is also neglected. As a side note, using such higher order contributions it might also be possible to displace walls with a variation in dielectric susceptibility such as those observed in quartz [78].

Given the small thickness of the domain wall compared to the typical scale of the electric field variation [72], the approximation

$$\int \vec{E}(x, y, z) \cdot \vec{P}(y - (y_i + \xi)) dy = (\vec{E}(x, y_i + \xi, z) \vec{P}_s) w \quad (7.4)$$

is used, where \vec{P}_s is the average polarization over the width of the APB (w) defined as $\vec{P}_s = \frac{1}{w} \int \vec{P}(y) dy$. Finally, only weak bending response from the wall is considered, i.e. the deflection angle (between the normal to the wall and y-axis) is assumed to be small. In accordance with the coordinate axes as shown in Fig. 7.1, the elemental surface area dS for a curved wall is expressed via $\xi(x, z)$, allowing us to rewrite the thermodynamic potential (7.3) as

$$U = \int [\lambda - (\vec{E}(x, y_i + \xi, z) \vec{P}_s) w] \sqrt{1 + (\nabla_2 \xi)^2} dx dz, \quad (7.5)$$

where $\nabla_2 = \left(\frac{\partial}{\partial x}, \frac{\partial}{\partial z} \right)$ is the two-dimensional del operator.

After taking the variational derivative of the thermodynamic potential (7.5) (refer Appendix A for details) one obtains the mechanical and electrostatic parts of the force balance (refer Eqs. (7.1),(7.2)) in the form

$$p_{me} = \nabla_2 \cdot [[\lambda - (\vec{E}(x, y_i + \xi, z) \vec{P}_s) w] \nabla_2 \xi] \quad (7.6)$$

$$p_{el} = w \left(\vec{P}_s \frac{\partial}{\partial \xi} \vec{E}(x, y_i + \xi, z) \right). \quad (7.7)$$

Thus, the electrostatic force p_{el} , which is the driving force for the displacement, in the approximation considered is proportional to the field gradient. In the expression for the mechanical force, (Eq. (7.6)) one recognizes the standard equation of an elastic membrane [79], where the mechanical surface tension is corrected by the additional electrostatic energy density. Hence, strictly speaking, this force is not purely mechanical, however we use this term for the sake of simplicity. Both contributions explicitly depend on the spontaneous polarization \vec{P}_s in the APB and the electric field \vec{E} from the AFM tip.

7.2 Displacement of an antiphase boundary induced by the electric field from an AFM tip

We consider the case where the polarization in the APB is oriented normally to the surface of the film, thus it interacts with the normal component (E_z) of the inhomogeneous electrical field from the AFM tip. It is of common knowledge that the electric field under an AFM tip with an applied voltage easily exceeds the theoretical coercive field for macroscopic domains in conventional ferroelectrics. Thus, irrespective of the sign of the field, the polarization in the APB at such fields is assumed to reorient itself to be aligned codirectional with the electric field, resulting in an attractive interaction with the tip. Henceforth, only such attractive interactions

7.2. Displacement of an antiphase boundary induced by the electric field from an AFM tip

of the APB towards the AFM tip are discussed.

The magnitude of the electric field is calculated using the expression for the field from an AFM tip with an applied voltage in a semi-infinite crystal[80], modified by using the method of image charges (second term within brackets in Eq. (7.8)) which corresponds to the case of a thin film with a bottom electrode. The normal component of the electric field has thus the following form:

$$E_z(x, y, z) = \frac{C_v V}{4\pi\epsilon_0 \frac{\kappa_c}{\kappa_a} (\sqrt{\kappa_c \kappa_a} + 1)} \left[\frac{\frac{z}{\kappa_c/\kappa_a} + R}{(x^2 + y^2 + (\frac{z}{\kappa_c/\kappa_a} + R)^2)^{3/2}} + \frac{\frac{2h-z}{\kappa_c/\kappa_a} + R}{(x^2 + y^2 + (\frac{2h-z}{\kappa_c/\kappa_a} + R)^2)^{3/2}} \right], \quad (7.8)$$

where V is the voltage applied to the AFM tip, h is the thickness of the film, ϵ_0 is the permittivity of the vacuum, κ_a and κ_c are the relative permittivities in directions in and out of the x-y plane, respectively, R is the radius of the AFM tip and C_v is the interfacial capacitance between the AFM tip and the surface. Here the case is considered where the AFM tip touches the film surface, and the interfacial capacitance is calculated accordingly using the sphere-plane model [81].

The boundary conditions for this model were derived to ensure the absence of localised forces at x_{cr} (x-coordinate of the point of transition from region 1 to region 2, refer Fig. 7.1) and as well at the free surface ($z = 0$) and at the interface with the bottom electrode ($z = h$):

$$\xi|_{x=\pm x_{cr}} = 0 = \frac{\partial \xi}{\partial x}|_{x=\pm x_{cr}} = \frac{\partial \xi}{\partial z}|_{z=0} = \frac{\partial \xi}{\partial z}|_{z=h}. \quad (7.9)$$

Using this model and the boundary conditions, the profile of the displaced APB is calculated starting from Eqs. (7.1) and (7.2).

All parameters used for the calculations are summarized in Table 7.1. The value of p_{pe}^{max} in this study is estimated assuming that the main pinning source is the Peierls barrier. Owing to lack of data on the values for the surface tension σ and the Peierls barrier p_{pe}^{max} in SrTiO₃, these are approximated from the values corresponding to 180° walls in BaTiO₃. All calculations were carried out in COMSOL Multiphysics Version 4.3a.

The profiles of the displaced wall are derived for APBs in thin films of various thicknesses with varying initial separations (y_i) and tip voltages. Figure 7.2 shows the coordinate y_p of the point on the wall lying closest to the AFM tip (at $x = 0$, see Fig. 7.1), in a 15 nm thick film as a function of the applied voltage for different values of the initial separation y_i . It is

| Parameter | Numerical Value(s) | Reference |
|----------------|-------------------------------|-----------|
| P_s | $4.2 \mu\text{C}/\text{cm}^2$ | 72 |
| λ | $10 \text{ mJ}/\text{m}^2$ | 82 |
| p_{Pe}^{max} | $0.05 \text{ mJ}/\text{m}^3$ | 83 |
| w | 10 nm | 72 |
| R | 10 nm | - |
| V | 10-50 V | - |
| κ_a | 5500 | 84 |
| κ_c | 8000 | 84 |

Table 7.1: Parameters for the calculation of displaced profiles of APBs in an SrTiO₃ like system. The values of the surface tension (λ) and the Peierls barrier (p_{Pe}^{max}) are approximated from 180° walls in BaTiO₃.

found that for all separations with increasing applied voltage the wall is drawn closer to the tip. At a certain voltage (varying with y_i) the wall is seen to 'collapse' towards the AFM tip, which is represented by a sharp drop in the coordinate y_p in Fig. 7.2. The 'collapse' occurs when with movement of the APB towards the tip the electric attraction of the wall to the tip increases more rapidly than it can be compensated by increase of the restoring mechanical 'force' associated with the surface area of the wall. As seen from Fig. 7.2, for larger initial separations y_i the 'collapse' occurs at larger voltages, which is the consequence of a generally weaker electric attraction of more distant APBs to the AFM tip at similar voltages.

In Fig. 7.3, the coordinates y_p near the free surface and near the bottom electrode are plotted against the applied voltage for the fixed initial displacement y_i (30 nm) for varying film thicknesses. The difference in the displacements observed at the upper and the lower interfaces is 10 % in the 50 nm thick film, and decreases with decreasing the film thickness down to negligible values (for a non-collapsed APB) in the 15 nm thick film. The average displacement of the wall, for the same voltage applied to the tip, is larger in thinner films. Besides, the applied voltage required for the collapse of the wall towards the tip decreases with the film thickness decrease. This behaviour follows from the variation in the electric field gradient ($\partial E_z / \partial \xi$) with z . For the parameters used in the study this results in lower APB displacements and higher collapse voltages with increasing film thickness.

7.2. Displacement of an antiphase boundary induced by the electric field from an AFM tip

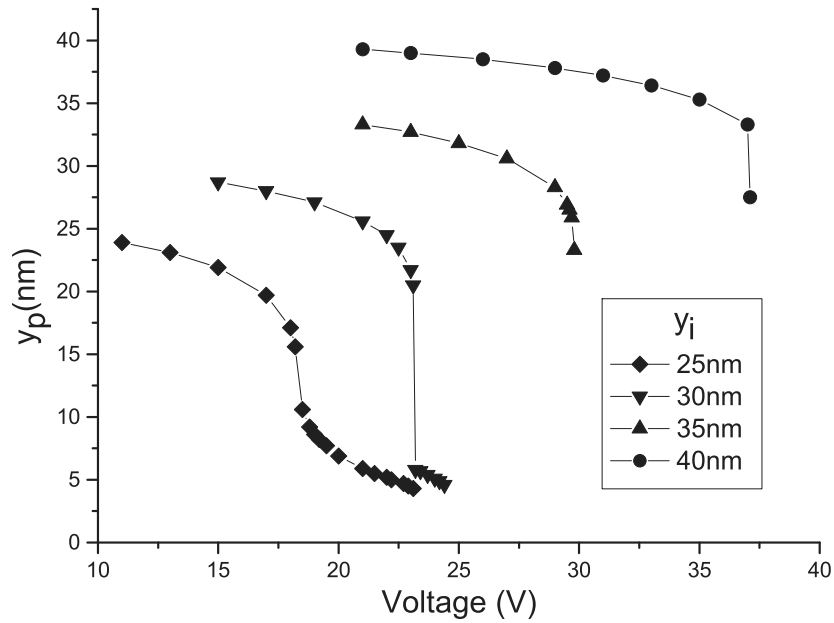


Figure 7.2: The coordinate y_p of the point on the wall lying closest to the AFM tip of radius 10 nm plotted as a function of the applied voltage for varying initial separation y_i in the 15 nm thick film. For all y_i , beyond a certain voltage the wall 'collapses' towards the AFM tip, represented by a sharp decrease in y_p .

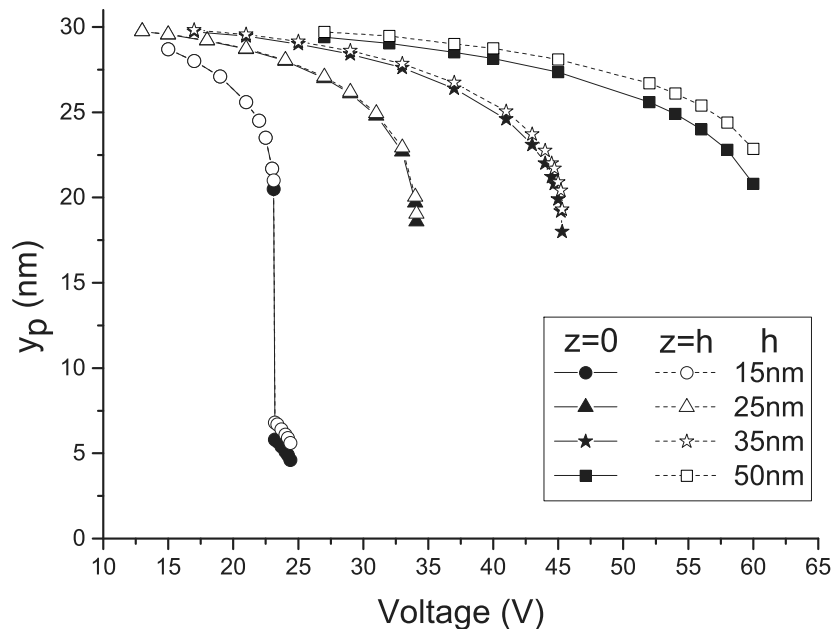


Figure 7.3: The coordinates y_p of the point on the wall lying closest to the AFM tip of radius 10nm near the free surface ($z = 0$, filled symbols) and near the bottom electrode ($z = h$, hollow symbols) as a function of the applied voltage for the initial separation $y_i = 30$ nm, calculated for three different film thicknesses h .

7.3 Retainment of the antiphase boundary displacement upon removal of the electric field

It is also to be ascertained that the displacement achieved on the application of the field is retained even on the removal of the applied voltage. After the voltage is removed (i.e. $p_{el} = 0$), the APB buckles back towards its initial flat profile. During the buckling the pinning force reorients itself opposite to the direction of the local curvature of the wall at all its points, until the new equilibrium is reached, which is described by the modified Eq. (7.2): $p_{pe} + p'_{me} = 0$, where p'_{me} is the mechanical force p_{me} (Eq. (7.6)) at $E = 0$. The final profile can be split into two regions (see inset in Fig. 7.4): region 1', where the profile buckles until the condition $|p'_{me}| = p_{pe}^{max}$ is reached, and region 2', where the wall profile remains unchanged, with $|p'_{me}| \leq p_{pe}^{max}$. In order to describe the profile of the APB after the buckling, the approximation of a two-dimensional profile is used, which was shown to be valid in thin films (see Fig. 7.3). In such a case, the curvature of the wall along the thickness is zero ($\frac{\partial^2 \xi}{\partial z^2} = 0$), and the equilibrium for region 1' can be written as

$$\left| \frac{\partial^2 \xi}{\partial x^2} \right| = \frac{\lambda}{p_{fe}^{max}}, \quad (7.10)$$

which describes the parabolic shape of the profile. The final profile of the wall after the buckling back on the removal of the voltage is obtained from the seamless integration of this parabola onto the profile obtained with the applied voltage (i.e. assuring continuity of ξ and $\partial \xi / \partial x$ between regions 1' and 2'), and the retained displacement is thus evaluated (see inset Fig. 7.4). The retraction of the wall on the removal of the electrical field ($\delta \xi$ in Fig. 7.4 inset) is then calculated as a percentage of the displacement with the voltage on.

Figure 7.4 shows the retraction percentage calculated for a 15 nm thick film for varying y_i after the application and subsequent removal of voltage. In all cases, the calculations indicate that more than 50% of the displacement caused with the application of the field is retained upon the removal of the electric field.

A remark should be made about the behaviour of the APBs in bulk crystals. It was shown that in such systems, if compared with thin films, the application of much higher voltages on the AFM tip is needed to reach similar displacements of the wall. Thus, thin films are more conducive for the experimental observations of the phenomenon discussed in this chapter.

7.3. Retainment of the antiphase boundary displacement upon removal of the electric field

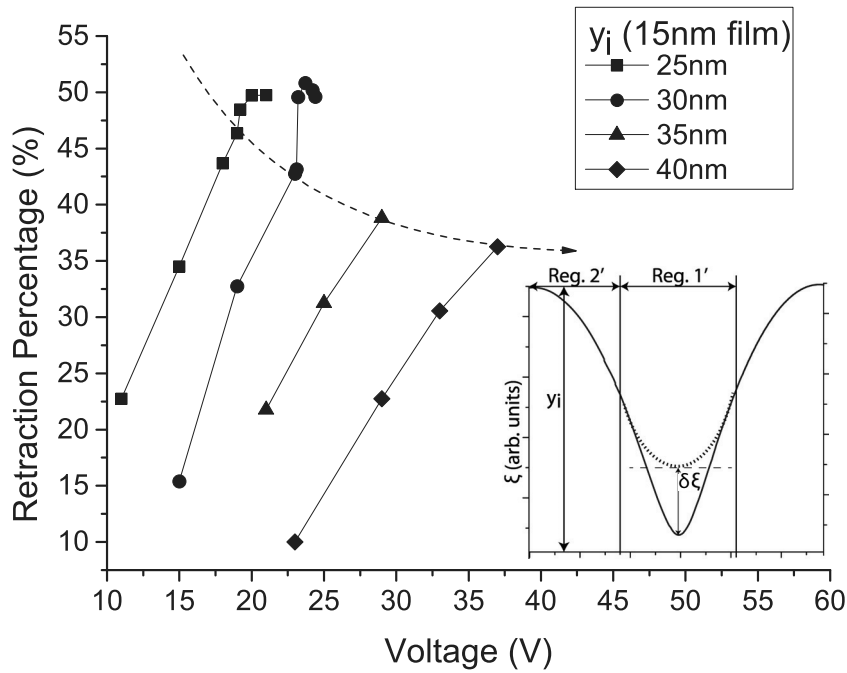


Figure 7.4: The retraction of an APB on the removal of the applied field calculated as a percentage of the total displacement for a 15nm thick film, plotted against the initial applied field from an AFM tip of radius 10nm placed at different distances (y_i) from the APB. The contour of the collapse voltage for the increasing y_i is represented by the dashed arrow. Inset: Illustration demonstrating the evolution of the profile of the APB on the application of voltage (full line) and upon its removal (dotted line).

7.4 Conclusions

In conclusion, drawing from previous works which predicted and observed the presence of polar APBs, the current work provides guidelines for future experimental work related to manipulation of polar APBs. On the application of moderate voltages (e.g., 40 V) to an AFM tip lying in the vicinity of an APB (e.g., in 20 nm from the APB) in a SrTiO₃-like material, the APB would be attracted to the tip and, at a certain voltage, collapse towards the tip. The voltage, upon application of which the wall collapses, decreases remarkably with decreasing the film thickness. On removing the voltage applied on the AFM tip at least 50% of the displacement is expected to be retained in thin films. Thin films would hence be more conducive for the experimental observations of the moving antiphase boundaries. The high retention of the displacement could be of high interest for the development of applications such as information storage.

Appendix A. Derivation of expressions of forces \mathbf{p}_{pe} , \mathbf{p}_{me}

In accordance with the coordinate system presented in Fig.1 of the main text, the thermodynamical potential of the system is given by

$$U = \int [\lambda - (\vec{E}(x, y_i + \xi, z) \vec{P}_s) w] \sqrt{1 + (\nabla_2 \xi)^2} dx dz, \quad (7.11)$$

where σ is the surface tension, \vec{P}_s is the average polarization over the width of the APB (w), $\vec{E}(x, y_i + \xi, z)$ is the spatially varying electric field from the AFM tip, $\xi(x, z)$ is the wall's displacement away from its initial separation from the AFM tip (y_i) and $\nabla_2 = \left(\frac{\partial}{\partial x}, \frac{\partial}{\partial z} \right)$ is the two-dimensional del operator. The integrand in Eq. (7.11) defines the functional that can be minimized using variational principles in order to estimate the equilibrium profile of the deformed wall. To this effect, on applying the Euler-Lagrange equation (Eq. (7.12)) to the potential described in Eq.7.11, a non-linear equation is obtained:

$$\frac{\partial L}{\partial \xi} - \left[\frac{\partial L}{(\partial \xi / \partial x)} + \frac{\partial L}{(\partial \xi / \partial z)} \right] = 0. \quad (7.12)$$

In this first approximation study, only weak bending response from the wall is considered, i.e. the deflection angle (between the normal to the wall and y-axis) are approximated to be small enough to neglect the deviation of the normal to the wall from the spatial coordinate y at all points. From the non-linear solution, using the weak bending approximation, only linear

terms with \vec{E} or ξ are retained to obtain Eq. (7.13):

$$\nabla_2 \cdot [\lambda - (\vec{E} \cdot \vec{P}_s) w] \nabla_2 \xi + w \left(\vec{P}_s \cdot \frac{\partial \vec{E}}{\partial \xi} \right) \left(\sqrt{1 + (\nabla_2 \xi)^2} \right) = 0. \quad (7.13)$$

The first term on the l.h.s. in Eq. (7.13) represents the standard equation for an elastic membrane with an additional electrostatic energy term, which has been retained despite being a bilinear term in the linear model in case of eventual cancellation with the surface tension. Although the first term is not purely mechanical, it is described as the mechanical force (Eq. (7.14) or p_{me} in the main text) for the sake of simplicity:

$$p_{me} = \nabla_2 \cdot [\lambda - (\vec{E} \cdot \vec{P}_s) w] \nabla_2 \xi. \quad (7.14)$$

The second term on the l.h.s. in Eq. (7.13) describes the electrostatic force (F_{el} in the main text) and describes the interaction between the electrical field gradient and the polarization profile. By neglecting $(\nabla_2 \xi)^2$ as of the second order of smallness F_{el} can be further simplified as follows:

$$p_{el} = w \left(\vec{P}_s \cdot \frac{\partial \vec{E}}{\partial \xi} \right) \left(\sqrt{1 + (\nabla_2 \xi)^2} \right) \approx w \left(\vec{P}_s \cdot \frac{\partial}{\partial \xi} \vec{E}(x, y_i + \xi, z) \right). \quad (7.15)$$

8 Summary and Outlook

Some properties of ferroelectric domain patterns, such as the internal structure of domain walls, orientation of the walls, which have been described for the case of infinite ferroelectrics, are typically believed by the scientific community to be applicable to thin films as well. This work shows the importance of thin-film-specific elastic effects on the formation of ferroelectric domain structures. Theoretical findings obtained in this work can help to understand better the properties of domain patterns in thin films and may serve as guidelines for controllable generation of domain structures with needed properties in ferroelectric films and for their application to potential new ferroelectrics-based devices.

It was shown that nonferroelastic domain walls may acquire elastic properties in ferroelectric thin films. Interaction of the domain wall, which is always stressed due to the electrostrictive coupling of the stresses with polarization, with the surfaces of the film results in redistribution of the elastic stresses inside the wall into the regions surrounding the wall. The distance of propagation of the redistributed stresses away from the wall is of the order of the film thickness. As a result, nonferroelastic domain walls can interact with each other by elastic means on distances far exceeding the correlation length, which has been conventionally considered as the maximal range of interaction between nonferroelastic walls. In certain configurations, the force of repulsion between nonferroelastic domain walls was shown to be large enough to compete with the action of typical electric fields of coercive values for the material. The effect may have a substantial impact on the polarization switching and domain pattern control in ferroelectric thin films.

Further, the orientation of ferroelastic domain walls was investigated, and mechanisms that can drive the walls off their permissible inclination were formulated. Elastic energy penalty associated with violation of the principle of mechanical compatibility of ferroelastic

domain walls was shown to be small enough in thin films to be comparable with other contributions to the energy, namely with the possible reduction of the domain wall self-energy. It was shown that, with decreasing the film thickness, the requirement of the minimal domain wall length starts to play an increasingly stronger impact on the domain wall orientation, violating the condition of mechanical compatibility in some geometries. In application to (001) BiFeO₃ rhombohedral films, large deviations of the 71° domain wall off its permissible orientation are predicted in films of thickness < 40 nm.

Another mechanism of orientation of ferroelastic domain walls was formulated and investigated. In films on a substrate, the incompatibility elastic stresses generated by lattice mismatches on a deviated wall may interfere with the film-substrate misfit stress, leading to relaxation of the latter and to decrease of the elastic energy of the film. In cases where such deviation is energetically favourable, the violation of the principle of mechanical compatibility of the wall is possible. This concept was applied to (001) tetragonal PZT thin films with *a/c*-domain structures. It was shown that in the structures with a narrow *a*-domain inclusion, the domain walls deviate off their permissible orientation, generating bound charges on the walls, which implies a possibility of having conductive domain walls in the systems. These predictions were supported by experimental observations of 60 nm PZT films, where metallic-like conductivity of the deviated domain walls was reported.

A theoretical description was provided for narrow domain inclusions into a dominant domain state in tetragonal ferroelectric films on an anisotropic (orthorhombic) substrate. It was shown that in the limit of thick films such domain structures follow linear scaling laws of domain periodicity and of the inclusion width, which lies in contrast to the classical Kittel-like square root dependence conventionally applied for description of domain structures. The parameters of the domain structure, such as periodicity of the structure, width of the narrow inclusion, is obtained by considering the energies of interaction of narrow domain inclusions between themselves and with the stresses of misfit between the dominant domain state and the substrate. The correspondence of the results of the theory for PZT films to the experimental observations was shown.

While focused mostly on properties of domain structures in ferroelectric materials, this work contains also the investigation of an antiphase boundary, having local ferroelectric properties, in antiferroelectric PbZrO₃. The mechanical response of the boundary on the external electric field generated by an AFM tip was modelled. It was shown that the electric field gradient can be used as the driving force for the antiphase boundary displacement. In thin films, the displacement of the boundary was described for varying film thicknesses,

voltages applied on the AFM tip, and other parameters of the system. In general, the boundary attracts to the tip when the voltage is applied, the effect being much larger in thinner films than in thicker films and in bulk crystals. When the applied voltage exceeds some threshold value depending on the parameters of the system, the collapse of the boundary towards the tip is observed. Upon removal of the electric field, less than 50% of the boundary displacement retracts due to the effect of the surface tension of the boundary, and the major part of the displacement retains.

8.1 Outlook

Within this work, theoretical description of some thin-film-specific properties of the ferroelectric domain structures was given. The next obvious step is to perform experimental analysis which would, in perspective, confirm the main findings of the work. For instance, in-plane deformations of the lattice surrounding a nonferroelastic domain wall in free-standing films, discussed in Chapter 3, suggest a direct applicability of TEM measurements for detection of the effect. Besides, the long-ranged elastic repulsion between nonferroelastic domain walls having relatively large values (shown to be comparable with the effect of coercive field in some materials) is of high experimental interest by itself.

The mechanisms of deviation of the ferroelastic domain wall discussed in Chapters 4, 5 may have manifestations in various ferroelectric systems. As it was shown, the application of the concept of the wall deviation driven by the mechanisms, such as domain wall self-energy minimization, film-substrate misfit stresses relaxation, can help to predict systems where the controllable generation of charged domain walls is possible, with possible applications in potential new devices with reconfigurable electric circuits.

Bibliography

- [1] J. Valasek, *Physical Review* **17**, 475 (1921).
- [2] M. A. Dubois and P. Muralt, *Applied Physics Letters* **74**, 3032 (1999).
- [3] N. Ledermann, J. Baborowski, A. Seifert, B. Willing, S. Hiboux, P. Muralt, N. Setter, and M. Forster, *Integrated Ferroelectrics* **35**, 1907 (2001).
- [4] J. Baborowski, N. Ledermann, P. Muralt, and D. Schmitt, *Integrated Ferroelectrics* **54**, 557 (2003).
- [5] P. Muralt, *Journal of Micromechanics and Microengineering* **10**, 136 (2000).
- [6] H. Ishiwara, *Journal of Nanoscience and Nanotechnology* **12**, 7619 (2012).
- [7] G. Catalan, J. Seidel, R. Ramesh, and J. F. Scott, *Reviews of Modern Physics* **84**, 119 (2012).
- [8] J. Seidel, *Journal of Physical Chemistry Letters* **3**, 2905 (2012).
- [9] P. Muralt, *Journal of the American Ceramic Society* **91**, 1385 (2008).
- [10] T. Mitsui and J. Furuichi, *Physical Review* **90**, 193 (1953).
- [11] A. L. Roitburd, *Physica Status Solidi a-Applied Research* **37**, 329 (1976).
- [12] W. Pompe, X. Gong, Z. Suo, and J. S. Speck, *Journal of Applied Physics* **74**, 6012 (1993).
- [13] N. A. Pertsev and G. Arlt, *Ferroelectrics* **123**, 27 (1991).
- [14] N. A. Pertsev and A. G. Zembilgotov, *Journal of Applied Physics* **78**, 6170 (1995).
- [15] A. E. Romanov, W. Pompe, and J. S. Speck, *Journal of Applied Physics* **79**, 4037 (1996).
- [16] N. A. Pertsev and A. Y. Emelyanov, *Physics of the Solid State* **39**, 109 (1997).
- [17] V. G. Koukhar, N. A. Pertsev, and R. Waser, *Physical Review B* **64**, 214103 (2001).

Bibliography

- [18] Y. L. Li, S. Y. Hu, Z. K. Liu, and L. Q. Chen, *Acta Materialia* **50**, 395 (2002).
- [19] Y. L. Li, S. Y. Hu, Z. K. Liu, and L. Q. Chen, *Applied Physics Letters* **78**, 3878 (2001).
- [20] A. Tagantsev, L. Cross, and J. Fousek, *Domains in Ferroic Crystals and Thin Films* (Springer, 2010).
- [21] A. K. Tagantsev, *Ferroelectrics* **375**, 19 (2008).
- [22] S. P. Chervonobrodov and A. L. Roytburd, *Ferroelectrics* **83**, 109 (1988).
- [23] J. Fousek and V. Janovec, *Journal of Applied Physics* **40**, 135 (1969).
- [24] J. Sapriel, *Physical Review B* **12**, 5128 (1975).
- [25] E. A. Eliseev, A. N. Morozovska, S. V. Kalinin, Y. Li, J. Shen, M. D. Glinchuk, L.-Q. Chen, and V. Gopalan, *Journal of Applied Physics* **106**, 084102 (2009).
- [26] J. Seidel, P. Maksymovych, Y. Batra, A. Katan, S. Y. Yang, Q. He, A. P. Baddorf, S. V. Kalinin, C. H. Yang, J. C. Yang, Y. H. Chu, E. K. H. Salje, H. Wormeester, M. Salmeron, and R. Ramesh, *Physical Review Letters* **105**, 197603 (2010).
- [27] S. Van Aert, S. Turner, R. Delville, D. Schryvers, G. Van Tendeloo, and E. K. H. Salje, *Advanced Materials* **24**, 523 (2012).
- [28] L. Goncalves-Ferreira, S. A. T. Redfern, E. Artacho, and E. K. H. Salje, *Physical Review Letters* **101**, 097602 (2008).
- [29] T. Sluka, A. K. Tagantsev, P. Bednyakov, and N. Setter, *Nature Communications* **4**, 1808 (2013).
- [30] J. Seidel, L. W. Martin, Q. He, Q. Zhan, Y. H. Chu, A. Rother, M. E. Hawkrige, P. Maksymovych, P. Yu, M. Gajek, N. Balke, S. V. Kalinin, S. Gemming, F. Wang, G. Catalan, *et al.*, *Nature Materials* **8**, 229 (2009).
- [31] X.-K. Wei, A. K. Tagantsev, A. Kvasov, K. Roleder, C.-L. Jia, and N. Setter, *Nature Communications* **5**, 3031 (2014).
- [32] A. L. Roytburd, *Journal of Applied Physics* **83**, 239 (1998).
- [33] P. Bintachitt, S. Jesse, D. Damjanovic, Y. Han, I. M. Reaney, S. Trolier-McKinstry, and S. V. Kalinin, *Proceedings of the National Academy of Sciences of the United States of America* **107**, 7219 (2010).

- [34] V. Nagarajan, A. Roytburd, A. Stanishevsky, S. Prasertchoung, T. Zhao, L. Chen, J. Melngailis, O. Auciello, and R. Ramesh, *Nature Materials* **2**, 43 (2003).
- [35] S. Conti and E. K. H. Salje, *Journal of Physics-Condensed Matter* **13**, L847 (2001).
- [36] S. Timoshenko and J. Goodier, *Theory of Elasticity* (McGraw-Hill, 1987).
- [37] L. Landau, E. Lifshitz, A. Kosevitch, and L. Pitaevskiy, *Theory of Elasticity* (Butterworth-Heinemann, 1986).
- [38] A. Flamant, *Comptes Rendus Hebdomadaires des Séances de l'Académie des Sciences* **114**, 1465 (1892).
- [39] J. X. Zhang, Y. L. Li, S. Choudhury, L. Q. Chen, Y. H. Chu, F. Zavaliche, M. P. Cruz, R. Ramesh, and Q. X. Jia, *Journal of Applied Physics* **103**, 094111 (2008).
- [40] I. Stolichnov, L. Feigl, L. J. McGilly, T. Sluka, X.-K. Wei, E. Colla, A. Crassous, K. Shapovalov, P. Yudin, A. K. Tagantsev, and N. Setter, *Nano Letters* **15**, 8049–8055 (2015).
- [41] S. K. Streiffer, C. B. Parker, A. E. Romanov, M. J. Lefevre, L. Zhao, J. S. Speck, W. Pompe, C. M. Foster, and G. R. Bai, *Journal of Applied Physics* **83**, 2742 (1998).
- [42] A. E. Romanov, M. J. Lefevre, J. S. Speck, W. Pompe, S. K. Streiffer, and C. M. Foster, *Journal of Applied Physics* **83**, 2754 (1998).
- [43] R. Dewit, *Journal of Research of the National Bureau of Standards Section a-Physics and Chemistry* **A 77**, 49 (1973).
- [44] R. Dewit, *Journal of Research of the National Bureau of Standards Section a-Physics and Chemistry* **A 77**, 607 (1973).
- [45] J. D. Eshelby, *Philosophical Transactions of the Royal Society of London Series a-Mathematical and Physical Sciences* **244**, 87 (1951).
- [46] M. Peach and J. S. Koehler, *Physical Review* **80**, 436 (1950).
- [47] A. K. Head, *Proceedings of the Physical Society of London Section B* **66**, 793 (1953).
- [48] P. Maksymovych, J. Seidel, Y. H. Chu, P. Wu, A. P. Baddorf, L.-Q. Chen, S. V. Kalinin, and R. Ramesh, *Nano Letters* **11**, 1906 (2011).
- [49] J. Guyonnet, I. Gaponenko, S. Gariglio, and P. Paruch, *Advanced Materials* **23**, 5377 (2011).
- [50] S. Farokhipoor and B. Noheda, *Physical Review Letters* **107**, 127601 (2011).

Bibliography

- [51] D. Meier, J. Seidel, A. Cano, K. Delaney, Y. Kumagai, M. Mostovoy, N. A. Spaldin, R. Ramesh, and M. Fiebig, *Nature Materials* **11**, 284 (2012).
- [52] E. A. Eliseev, A. N. Morozovska, Y. Gu, A. Y. Borisevich, L.-Q. Chen, V. Gopalan, and S. V. Kalinin, *Physical Review B* **86**, 085416 (2012).
- [53] S. V. Kalinin, A. Borisevich, and D. Fong, *Acs Nano* **6**, 10423 (2012).
- [54] S. Farokhipoor and B. Noheda, *Journal of Applied Physics* **112**, 052003 (2012).
- [55] R. K. Vasudevan, W. Wu, J. R. Guest, A. P. Baddorf, A. N. Morozovska, E. A. Eliseev, N. Balke, V. Nagarajan, P. Maksymovych, and S. V. Kalinin, *Advanced Functional Materials* **23**, 2592 (2013).
- [56] I. Stolichnov, M. Iwanowska, E. Colla, B. Ziegler, I. Gaponenko, P. Paruch, M. Huijben, G. Rijnders, and N. Setter, *Applied Physics Letters* **104**, 132902 (2014).
- [57] E. Strelcov, Y. Kim, S. Jesse, Y. Cao, I. N. Ivanov, I. I. Kravchenko, C.-H. Wang, Y.-C. Teng, L.-Q. Chen, Y. H. Chu, and S. V. Kalinin, *Nano Letters* **13**, 3455 (2013).
- [58] P. Maksymovych, A. N. Morozovska, P. Yu, E. A. Eliseev, Y.-H. Chu, R. Ramesh, A. P. Baddorf, and S. V. Kalinin, *Nano Letters* **12**, 209 (2012).
- [59] T. Sluka, A. K. Tagantsev, D. Damjanovic, M. Gureev, and N. Setter, *Nature Communications* **3**, 748 (2012).
- [60] N. Balke, B. Winchester, W. Ren, Y. H. Chu, A. N. Morozovska, E. A. Eliseev, M. Huijben, R. K. Vasudevan, P. Maksymovych, J. Britson, S. Jesse, I. Kornev, R. Ramesh, L. Bellaiche, L. Q. Chen, *et al.*, *Nature Physics* **8**, 81 (2012).
- [61] A. Crassous, T. Sluka, A. K. Tagantsev, and N. Setter, *Nature Nanotechnology* **10**, 614 (2015).
- [62] R. K. Vasudevan, A. N. Morozovska, E. A. Eliseev, J. Britson, J. C. Yang, Y. H. Chu, P. Maksymovych, L. Q. Chen, V. Nagarajan, and S. V. Kalinin, *Nano Letters* **12**, 5524 (2012).
- [63] M. Y. Gureev, A. K. Tagantsev, and N. Setter, *Physical Review B* **83**, 184104 (2011).
- [64] L. Feigl, P. Yudin, I. Stolichnov, T. Sluka, K. Shapovalov, M. Mtebwa, C. S. Sandu, X. K. Wei, A. K. Tagantsev, and N. Setter, *Nature Communications* **5**, 4677 (2014).
- [65] M. Dawber, K. M. Rabe, and J. F. Scott, *Reviews of Modern Physics* **77**, 1083 (2005).

- [66] O. Nesterov, S. Matzen, C. Magen, A. H. G. Vlooswijk, G. Catalan, and B. Noheda, *Applied Physics Letters* **103**, 142901 (2013).
- [67] J. H. Sung, W.-M. Lee, J. H. Lee, K. Chu, D. Lee, X. Moya, N. D. Mathur, C.-H. Yang, J.-H. Park, and M.-H. Jo, *Npg Asia Materials* **5**, e38 (2013).
- [68] Y.-H. Chu, Q. Zhan, L. W. Martin, M. P. Cruz, P.-L. Yang, G. W. Pabst, F. Zavaliche, S.-Y. Yang, J.-X. Zhang, L.-Q. Chen, D. G. Schlom, I. N. Lin, T.-B. Wu, and R. Ramesh, *Advanced Materials* **18**, 2307 (2006).
- [69] L. I. Feigl, L. J. McGilly, C. S. Sandu, and N. Setter, *Applied Physics Letters* **104**, 172904 (2014).
- [70] A. L. Roytburd, "Elastic domains in ferroelectric epitaxial films," in *Thin Film Ferroelectric Materials and Devices*, edited by R. Ramesh (Springer US, 1997).
- [71] T. Ohnishi, M. Lippmaa, T. Yamamoto, S. Meguro, and H. Koinuma, *Applied Physics Letters* **87**, 241919 (2005).
- [72] A. K. Tagantsev, E. Courtens, and L. Arzel, *Physical Review B* **64**, 224107 (2001).
- [73] H. Yokota, H. Usami, R. Haumont, P. Hicher, J. Kaneshiro, E. K. H. Salje, and Y. Uesu, *Physical Review B* **89**, 144109 (2014).
- [74] J. F. Scott, E. K. H. Salje, and M. A. Carpenter, *Physical Review Letters* **109**, 187601 (2012).
- [75] P. Mokry, Y. Wang, A. K. Tagantsev, and I. Stolichnov, "Study of the evolution of 180 degrees domain pattern microstructure using measurements of nonlinear permittivity," in *2007 Sixteenth Ieee International Symposium on the Applications of Ferroelectrics, Vols 1 and 2* (2007).
- [76] M. A. Collins, A. Blumen, J. F. Currie, and J. Ross, *Physical Review B* **19**, 3630 (1979).
- [77] A. L. Roitburd, *Doklady Akademii Nauk Sssr* **197**, 1051 (1971).
- [78] M. B. Walker and R. J. Gooding, *Physical Review B* **32**, 7408 (1985).
- [79] B. D. Laikhtman, *Fizika Tverdogo Tela* **15**, 93 (1973).
- [80] M. Molotskii, *Journal of Applied Physics* **93**, 6234 (2003).
- [81] W. Smythe, *Static and Dynamic Electricity* (McGraw-Hill, 1950).
- [82] V. A. Zhirnov, *Soviet Physics JETP-USSR* **8**, 822 (1959).

Bibliography

[83] E. V. Burtsev and S. P. Chervonobrodov, *Ferroelectrics* **45**, 97 (1982).

[84] K. A. Muller and H. Burkard, *Physical Review B* **19**, 3593 (1979).

List of publications

The following works have been published by K. Shapovalov:

- I. Stolichnov, L. Feigl, L. J. McGilly, T. Sluka, X.-K. Wei, E. Colla, A. Crassous, K. Shapovalov, P. Yudin, A. K. Tagantsev, and N. Setter, "Bent Ferroelectric Domain Walls as Reconfigurable Metallic-Like Channels", *Nano Letters* **15**, 8049 (2015). Used in the thesis, Chapter 5.
- K. Vaideeswaran, K. Shapovalov, P. V. Yudin, A. K. Tagantsev, and N. Setter, "Moving antiphase boundaries using an external electric field", *Applied Physics Letters* **107**, 192905 (2015). Used in the thesis, Chapter 7.
- M. Mtebwa, L. Feigl, P. Yudin, L. J. McGilly, K. Shapovalov, A. K. Tagantsev, and N. Setter, "Room temperature concurrent formation of ultra-dense arrays of ferroelectric domain walls", *Applied Physics Letters* **107**, 142903 (2015). Not used in the thesis.
- K. Shapovalov, P. V. Yudin, A. K. Tagantsev, E. A. Eliseev, A. N. Morozovska, and N. Setter, "Elastic Coupling between Nonferroelastic Domain Walls", *Physical Review Letters* **113**, 207601 (2014). Used in the thesis, Chapter 3.
- L. Feigl, P. Yudin, I. Stolichnov, T. Sluka, K. Shapovalov, M. Mtebwa, C. S. Sandu, X.-K. Wei, A. K. Tagantsev, and N. Setter, "Controlled stripes of ultrafine ferroelectric domains", *Nature Communications* **5**, 4677 (2014). Used in the thesis, Chapter 6.

Konstantin Shapovalov

Address:
Chemin de Champ-Paris 37,
1304 Cossonay-Ville,
Vaud, Switzerland
Work phone: +41 21 693 1043
Cell phone: +41 76 613 0706
E-mail: konstantin.shapovalov@epfl.ch
Date of birth: 19 June 1992
Marital status: single



EDUCATION

Doctor in Material Science (est. February 2016)

Swiss Federal Institute of Technology (EPFL), School of Material Science and Engineering.
Lausanne, Vaud, Switzerland.
PhD thesis title: Thin-film-specific elastic effects in ferroelectric domain structures.
Advisors: Prof. Alexander K. Tagantsev, Prof. Nava Setter.

Bachelor in General Physics (2012)

Novosibirsk State University, Department of Physics. Novosibirsk, Russia.
Average mark: 4.9 out of 5.
B.Sc. thesis title: Capacitance Spectroscopy of Dirac Fermions in CdHgTe/HgTe/CdHgTe Quantum Well.
Advisor: Dr. D. A. Kozlov.

High school education (2008)

Boarding high school "Specialised Educational Scientific Centre on Physics, Mathematics, Chemistry and Biology of Novosibirsk State University" with all over Russia selection of talented children, affiliated with the Novosibirsk State University. Novosibirsk, Russia.

RESEARCH EXPERIENCE

2012-est.2016: Assistant-PhD Student, Ceramics Laboratory, Swiss Federal Institute of Technology (EPFL). Lausanne, Vaud, Switzerland.

Research project: Investigation of the Domain Structure of Thin Ferroelectric Films.

Principal functions:

- Theoretical modelling of domain structures of thin ferroelectric films taking into account electric and elastic effects using Landau-Ginzburg-Devonshire theory.
 - Investigation of the internal structure of domain walls and of the inter-wall interaction.
- The work is performed in close cooperation with the experimental group of the Ceramics Laboratory.

2010-2012: Research Assistant, Rzhanov Institute of Semiconductor Physics, Siberian Branch of the Russian Academy of Sciences. Novosibirsk, Russia.

Research project: Investigation of Transport Properties and Spectrum of Dirac Fermions in CdHgTe/HgTe/ CdHgTe Quantum Well.

TEACHING EXPERIENCE

2014-est.2015: assistant of the bachelor course "Theory of Materials: from Structure to Properties", EPFL, Lausanne, Switzerland. Compilation of the exercises set in cooperation with Prof. A. Tagantsev; assisting students during the exercises sessions.

RESEARCH PUBLICATIONS

1. I. Stolichnov, L. Feigl, L. J. McGilly, T. Sluka, X.-K. Wei, E. Colla, A. Crassous, K. Shapovalov, P. Yudin, A. K. Tagantsev, and N. Setter, *Bent Ferroelectric Domain Walls as Reconfigurable Metallic-Like Channels*, *Nano Letters* **15**, 8049 (2015).
2. K. Vaideeswaran, K. Shapovalov, P. V. Yudin, A. K. Tagantsev, and N. Setter, *Moving antiphase boundaries using an external electric field*, *Applied Physics Letters* **107**, 192905 (2015).
3. M. Mtebwa, L. Feigl, P. Yudin, L. J. McGilly, K. Shapovalov, A. K. Tagantsev, and N. Setter, *Room temperature concurrent formation of ultra-dense arrays of ferroelectric domain walls*, *Applied Physics Letters* **107**, 142903 (2015).
4. K. Shapovalov, P. V. Yudin, A. K. Tagantsev, E. A. Eliseev, A. N. Morozovska, and N. Setter, *Elastic Coupling between Nonferroelastic Domain Walls*, *Physical Review Letters* **113**, 207601 (2014).
5. L. Feigl, P. Yudin, I. Stolichnov, T. Sluka, K. Shapovalov, M. Mtebwa, C. S. Sandu, X.-K. Wei, A. K. Tagantsev, and N. Setter, *Controlled Stripes of Ultrafine Ferroelectric Domains*, *Nature Communications* **5**, 4677 (2014).

CONFERENCE ABSTRACTS

1. K. Shapovalov et al, *Elastic Coupling between Nonferroelastic Domain Walls*, 2015 Joint ISAF-ISIF-PFM Conference, Singapore, 2015. Oral contribution.
2. K. Shapovalov et al, *Mechanically Incompatible Domain Walls in Thin Films*, International Workshop on Topological Structures in Ferroic Materials, Sydney, Australia, 2015. Oral contribution.
3. K. Shapovalov et al, *Elastic Coupling between Non-ferroelastic Domain Walls in Ferroelectric Films*, 2014 Workshop on Fundamental Physics of Ferroelectrics, Washington, DC, USA, 2014. Poster
4. K. Shapovalov et al, *Elastic Broadening of 180-degree Domain Walls in Perovskite Thin Films*, 13th International Meeting on Ferroelectricity, Krakow, Poland, 2013. Oral contribution.

AWARDS

- IEEE Ultrasonics, Ferroelectrics and Frequency Control Society Student Travel Fund, limited funding for oversea students traveling to Singapore for presenting oral talk or poster at 2015 Joint ISAF-ISIF-PFM Conference, Singapore, 2015.
- 3rd prize student paper award, for the presentation "Investigation of Properties of Dirac Fermions in CdHgTe/HgTe/CdHgTe Quantum Well" at 50th International Students Scientific Conference "Students and Progress in Science and Technology", Novosibirsk, Russia, 2012.
- 3rd prize at Kamchatka's regional Olympiad on Mathematics, Petropavlovsk-Kamchatsky, Russia, 2007.

RELEVANT SKILLS

Theoretical description of ferroelectric systems

Analytical: Landau-Ginzburg-Devonshire theory, theory of elasticity and plasticity, fictitious dislocations theory. Software: Wolfram Mathematica.

Numerical: phase-field simulations, basic knowledge of density functional theory. Software: Comsol Multiphysics, Matlab.

Languages: Russian – Native, English – Fluent, French – Good.

HOBBIES

Cycling, alpine skiing, scuba diving, art cinema

REFERENCES

Prof. Alexander K. Tagantsev

Professor,
Ceramics Laboratory,
Swiss Federal Institute of
Technology (EPFL),
Lausanne, Switzerland.

e-mail:
alexander.tagantsev@epfl.ch

Prof. Nava Setter

Head of Laboratory,
Ceramics Laboratory,
Swiss Federal Institute of
Technology (EPFL),
Lausanne, Switzerland.

e-mail:
nava.setter@epfl.ch

Prof. Kvon Ze Don

Head of Laboratory,
Rzhanov Institute of
Semiconductor Physics,
SB RAS, Novosibirsk, Russia.

e-mail:
kvon@isp.nsc.ru